

**Hydrogen sorption and desorption properties of Pd-alloys and steels investigated by electrochemical methods and mass spectrometry**

Uluc, Anna

**DOI**

[10.4233/uuid:31644ed3-5ec4-4328-a28e-a6fedac9ddd3](https://doi.org/10.4233/uuid:31644ed3-5ec4-4328-a28e-a6fedac9ddd3)

**Publication date**

2015

**Document Version**

Final published version

**Citation (APA)**

Uluc, A. (2015). *Hydrogen sorption and desorption properties of Pd-alloys and steels investigated by electrochemical methods and mass spectrometry*. [Dissertation (TU Delft), Delft University of Technology]. <https://doi.org/10.4233/uuid:31644ed3-5ec4-4328-a28e-a6fedac9ddd3>

**Important note**

To cite this publication, please use the final published version (if applicable). Please check the document version above.

**Copyright**

Other than for strictly personal use, it is not permitted to download, forward or distribute the text or part of it, without the consent of the author(s) and/or copyright holder(s), unless the work is under an open content license such as Creative Commons.

**Takedown policy**

Please contact us and provide details if you believe this document breaches copyrights. We will remove access to the work immediately and investigate your claim.

**Hydrogen sorption and desorption properties of Pd-alloys  
and steels investigated by electrochemical methods and  
mass spectrometry**

**Proefschrift**

ter verkrijging van de graad van doctor  
aan de Technische Universiteit Delft,  
op gezag van de Rector Magnificus Prof.ir. K.C.A.M. Luyben;  
voorzitter van het College voor Promoties,  
in het openbaar te verdedigen op dinsdag 24 november 2015 om 10.00 uur

door

Anna Vanya ULUC

Master of Science in Materials Science and Engineering, Sabancı  
Üniversitesi (Turkije)

geboren te Istanbul, Turkije

This dissertation has been approved by the promotor: Prof. dr. B.J. Thijsse

Copromotor: Dr. A.J. Böttger

Composition of the doctoral committee:

Rector Magnificus	chairman
Prof. dr. B.J. Thijsse	Delft University of Technology
Dr. A.J. Böttger	Delft University of Technology

Independent members:

Prof.dr.ir. J. Sietsma	Delft University of Technology
Prof.dr.ir. L.A.I. Kestens	Gent University, Belgium
Prof.dr. F.M. Mulder	Delft University of Technology
Dr.ir. R.H. Vegter	SKF Engineering & Research Centre Netherlands

# CONTENTS

<b>CHAPTER 1: Introduction.....</b>	<b>3</b>
1.1. Interaction of hydrogen with materials .....	3
1.2. Scope of this thesis .....	10
1.3. Outline of this thesis .....	11
References .....	13
<b>CHAPTER 2: Hydrogen Sorption and Desorption Related Properties of Pd-alloys Determined by Cyclic Voltammetry .....</b>	<b>17</b>
2.1. Introduction.....	17
2.2. Experimental procedure .....	19
2.3. Results and discussion.....	20
2.4. Conclusions .....	31
Acknowledgements .....	32
References .....	33
<b>CHAPTER 3: Investigation of H-desorption from Pd and Pd-alloys by Mass Spectrometry and the Role of Water Forming Reactions.....</b>	<b>37</b>
3.1. Introduction.....	37
3.2. Experimental procedure .....	38
3.3. Results and discussion.....	40
3.4. Conclusions .....	52
Acknowledgements .....	52
References .....	53
<b>CHAPTER 4: The Role of Heat Treatment and Alloying Elements on Hydrogen Uptake in Aermet 100 Ultrahigh-Strength Steel .....</b>	<b>57</b>
4.1. Introduction.....	57
4.2. Experimental procedure .....	59
4.3. Results and discussion.....	61
4.4. Conclusions .....	68
Acknowledgements .....	69
References .....	70

<b>CHAPTER 5: The Effect of Austenite and V-carbide on the Diffusible Hydrogen in Steels for Automotive Applications.....</b>	<b>75</b>
5.1. Introduction.....	75
5.2. Experimental procedure .....	77
5.3. Results and discussion.....	83
5.4. Conclusions .....	91
Acknowledgements .....	91
References .....	92
<b>APPENDICES.....</b>	<b>97</b>
APPENDIX A Calculation of [H]/[Pd] from X-ray diffraction peak shifts .....	97
APPENDIX B Effect of isotopes and fragmentation probabilities on a mass spectrum .....	99
APPENDIX C Calibration for Mass spectroscopy measurements.....	101
<b>Summary .....</b>	<b>107</b>
<b>Samenvatting.....</b>	<b>113</b>
<b>Acknowledgements.....</b>	<b>119</b>
<b>About the Author .....</b>	<b>123</b>

# CHAPTER 1



# CHAPTER 1: Introduction

---

*“FOR a long time it has been well known to wire-drawers and other manufacturers, who free the iron or steel they are engaged in working from rust by cleaning it with sulphuric acid, that after this process the metal becomes much more brittle than before. Further, if a piece of iron wire that has been cleaned in sulphuric acid be bent rapidly to and fro till it is broken, and the fracture be then moistened with the tongue, bubbles of gas arise from it, causing it to froth. If this same wire be now gently heated for a few hours, or left in a dry warm room for some days, it will be found to have regained its original toughness, and not to froth when broken and the fracture moistened.”*

*W. H. Johnson, Nature, 1875*

---

## 1.1. Interaction of hydrogen with materials

A brief article published in Nature by William H. Johnson [1] reveals that the deterioration effect of hydrogen on steels is known since (at least) as early as 1875. The loss of ductility and brittle fracture of steel parts upon cleaning them in sulphuric acid as explained in Johnson’s article [1] is what is now generally known as “hydrogen embrittlement” and it refers to the degradation of mechanical properties of materials due to hydrogen. Since those early days, hydrogen embrittlement has remained being the cause of unpredictable and severe brittle damage of many technologically important alloys and steels. Large improvements in understanding the interaction of hydrogen with materials have been made and nowadays three main mechanisms that describe H embrittlement are accepted: (i) hydrogen enhanced decohesion (HEDE) [2, 3], (ii) hydrogen enhanced localized plasticity (HELP) [4] and (iii) a recently proposed hydrogen-enhanced strain-induced vacancy (HESIV) mechanism [5].

Developing an understanding about hydrogen-assisted cracking is not only *interesting* from a research point of view, but it is also very *important* for practical purpose. Starting in the early 1990’s, steels that have high tensile strength together with high fracture toughness were developed [6]. These materials fulfilled the challenging needs of high strength and fracture

toughness for applications in aerospace, marine, energy, automotive and defense industries. Still, in spite of all the benefits of these high performance materials, their susceptibility to degradation of the fracture resistance by hydrogen kept on being a major concern [6].

In addition to steels, many metals and alloys show a strong interaction with hydrogen. Several applications make use of the strong metal-hydrogen (M-H) interaction, e.g., energy-storage systems, sensor applications and hydrogen purification systems [7, 8]. These applications have different focuses regarding hydrogen interaction and related properties. For example, for the metal-based hydrogen energy-storage materials, improving their adsorption/desorption kinetics, storage capacity and lifetime are the main concerns [9, 10]. In sensor applications, the main objectives are to enhance the sensitivity and selectivity of detecting hydrogen, reduce the response time and improve the reliability [11]. In the field of membrane technology used to separate hydrogen from a mixture of gases, Pd-based alloys are often used because of their high selectivity and temperature resistance. The major focus is to increase the lifetime of the metal alloys [7, 12, 13]. The lifetime of hydrogen storage materials and Pd-based membranes is usually limited by embrittlement, which -unlike steels- is due to large volume changes upon absorption/desorption of hydrogen by hydride formation [14].

Microstructure and composition affect the thermodynamic and mechanical stability of a material in the presence of hydrogen, as well as the kinetics of processes such as crack propagation, absorption, desorption and diffusion of hydrogen. For all research and application areas that make use of H–M interactions, tailoring of the (micro)structure and composition is necessary to reach the individual targeted characteristics along with manageable costs. In order to enable such tailoring, a deep knowledge about how hydrogen interacts with different phases and microstructural features such as dislocations, vacancies, alloying elements, grain boundaries and precipitates is essential. A good comprehension of hydrogen embrittlement cannot be achieved without understanding model systems such as Pd-H or without a systematic study of the interaction of hydrogen with materials of various crystal- and micro-structure. Succeeding in understanding and tailoring the interaction of hydrogen with a material by controlling its microstructure is essential for further material improvement.

### **1.1.1. Hydrogen embrittlement mechanisms**

In this section, the three generally accepted mechanisms for hydrogen embrittlement are introduced and discussed. The basics of these mechanisms are used to define further research on understanding phenomena related to hydrogen embrittlement.

*a) Hydrogen enhanced decohesion mechanism (HEDE)*

According to the HEDE mechanism, hydrogen accumulates in the lattice and reduces the cohesive metal-metal bonding strength. Hydrogen segregation occurs at the crack tip fracture process zone (FPZ) where the tensile stresses are at maximum. Crack propagation is enhanced when the tensile stresses at the crack tip opening exceed the local reduced cohesive strength. Although the mechanism is likely from several point of views, there is still no clear experimental evidence proving that hydrogen lowers the interatomic bonding forces [15]. Particularly, whether a substantially high hydrogen concentration could occur that would confirm the HEDE mechanism is still being debated [16, 17].

*b) Hydrogen enhanced localized plasticity mechanism (HELP)*

This model is based on observations that the free hydrogen in the solid solution reduces the interaction of dislocations with obstacles, lowering the stresses for dislocation movement within the lattice. In the end, the amount of deformation in the vicinity of the fracture surface is increased. Thus, this model suggests that the failure process is locally highly plastic rather than brittle. The main evidence for the HELP mechanism is obtained by *in-situ* TEM observations, which showed an increase of the number of dislocations in a pileup in the presence of hydrogen [18]. Although intending to be a direct evidence for an increase in crack mobility, the method itself is the subject of criticism. Since the TEM study makes use of thin foils (<200 nm), it is suggested that surface related phenomena might be more pronounced in such a way that the observed phenomena might be unique for thinned specimen [15].

*c) Hydrogen-enhanced strain-induced-vacancy mechanism (HESIV)*

The third and more recent model proposes that the role of hydrogen in embrittlement is indirect through stabilizing and promoting vacancy agglomeration that results in failure. The microstructure is suggested to play a major role (and not the hydrogen concentration itself) in determining a material's susceptibility to hydrogen embrittlement. Additionally, crack formation is supposed to depend on the material's ability to create vacancies under stress [16]. The model first explains that when hydrogen is present in the environment during straining, higher quantities of hydrogen are absorbed than when H is not present during straining. This is shown in a number of analyses to be due to the increase in the number of vacancies during straining [5]. This active vacancy formation is expected to be more pronounced during the later stages of deformation as a result of the increased number of interactions between dislocations. It is also shown that hydrogen reduced ductile crack growth resistance through an increase in the number

of vacancies. Nucleation of a high density of voids enhances the localization of voids at the crack tip, thus leading to shear instability associated with crack advance [5].

Regardless of the *type* of embrittlement mechanism, the amount and mobility of hydrogen play a key role in the failure of technologically important alloys. The mobility of hydrogen is to a large extent governed by the number and type of traps (as determined by the microstructure) present in the material. The effect of traps on the diffusivity of hydrogen will be discussed in the next section.

### 1.1.2. Trapping of hydrogen

Hydrogen can be trapped at various microstructural features in an alloy. This alters the amount of hydrogen dissolved in the lattice and affects the diffusivity, hence the importance of trapping phenomena in embrittlement. High strength is known to correlate with trapping because the nanoscale features (precipitates) that are deliberately added to the microstructure in order to strengthen an alloy offer effective sites for H trapping [6].

Hydrogen binds to different types of traps with different strength. Two simplified schematics of the energy landscape as experienced by hydrogen in steels are given to qualitatively illustrate strengths of traps (Figure 1.1 from [19]). In Figure 1.1a, an incoherent TiC precipitate trap in steels as an example for a strong trap is shown. In this case, the activation energy for trapping ( $E_t$ ) is higher than that for lattice diffusion ( $E_{diff}$ ).

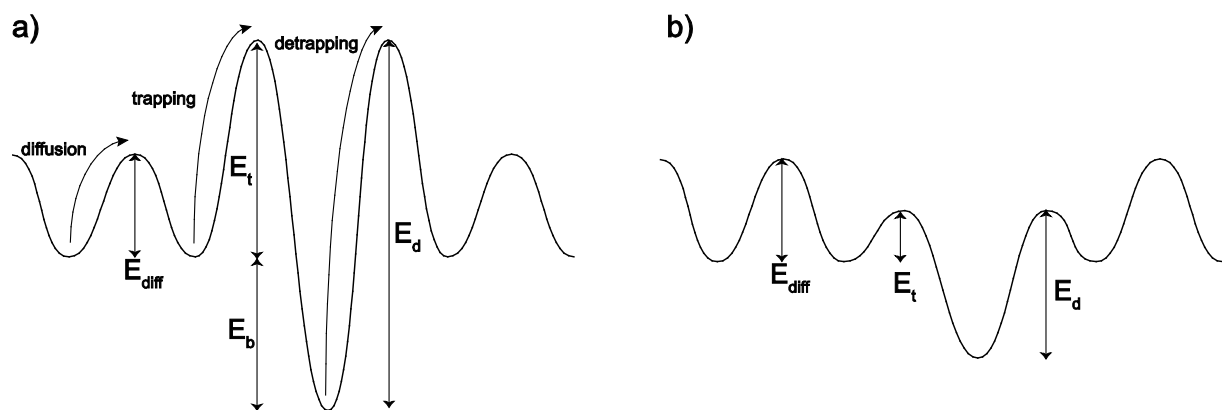


Figure 1.1. Different types of traps in terms of their trapping energy.  $E_{diff}$ : Activation energy for diffusion,  $E_b$ : Binding Energy,  $E_t$ : Trapping activation energy  $E_d$ : Detrapping activation energy. a) An example of a TiC trap in steel where a high activation energy is needed for both trapping and detrapping to occur. b) An example of a low-angle grain boundary trap where the activation energy for trapping is smaller than that for lattice diffusion.

The activation energy needed to escape the trap exceeds the activation energy for trapping because of the strong bonding to the trap, *i.e.* the detrapping energy or desorption activation energy is  $E_d = E_t + E_b$ . This strong interaction leads to the “irreversible” nature of these types of

traps; once hydrogen is trapped it is difficult to remove it. Another case is shown in Figure 1.1b, where a typical low-angle grain boundary trap in steels is schematically depicted. Here, the necessary activation energy for trapping is smaller than the activation energy needed for lattice diffusion, thus a hydrogen atom is readily trapped. Generally, the binding energy of H to a grain boundary is small and the detrapping activation energy is slightly higher than that for diffusion. This makes these types of traps of “reversible” nature, implying that hydrogen can easily be detrapped.

While reversible traps are expected to play a major role in hydrogen embrittlement by acting as reservoirs to supplement hydrogen that can diffuse to the crack tips, irreversible traps presumably do not have such effect. On the contrary, they are restraining hydrogen embrittlement by trapping hydrogen and hindering its diffusion to the crack tips or other regions of high stress [20]. Whether a trap should be termed “reversible” or “irreversible” is not straightforward. For a thermally activated process, the probability for a H atom to escape a trap is proportional to  $\exp(-E_d/RT)$  resulting in an increased probability of escaping a trap with increasing temperature. It is important to note that different methods of measuring the binding energies, as well as slightly different microstructures result in differently reported binding energies.

Although the values for binding energy of traps are difficult to establish, in general, traps are found in the following order of increasing trapping strength [17, 21-23]:

- (i) Some solute atoms
- (ii) Free surfaces and subsurface layers
- (iii) Vacancies and vacancy clusters
- (iv) Dislocation cores and strain fields
- (v) Grain boundaries including prior-austenite grain boundaries in martensitic steels
- (vi) Precipitate/matrix interfaces and strain fields around precipitates
- (vii) Inclusion/matrix interfaces
- (viii) Voids and internal cracks

Lynch depicts some of these trap sites [17]. In Figure 1.2a, the atomic scale traps are schematically shown. These smaller size traps are usually correlated with low binding energy traps. In general, as the size of the traps increases (see Figure 1.2b) the trap binding energies increase.

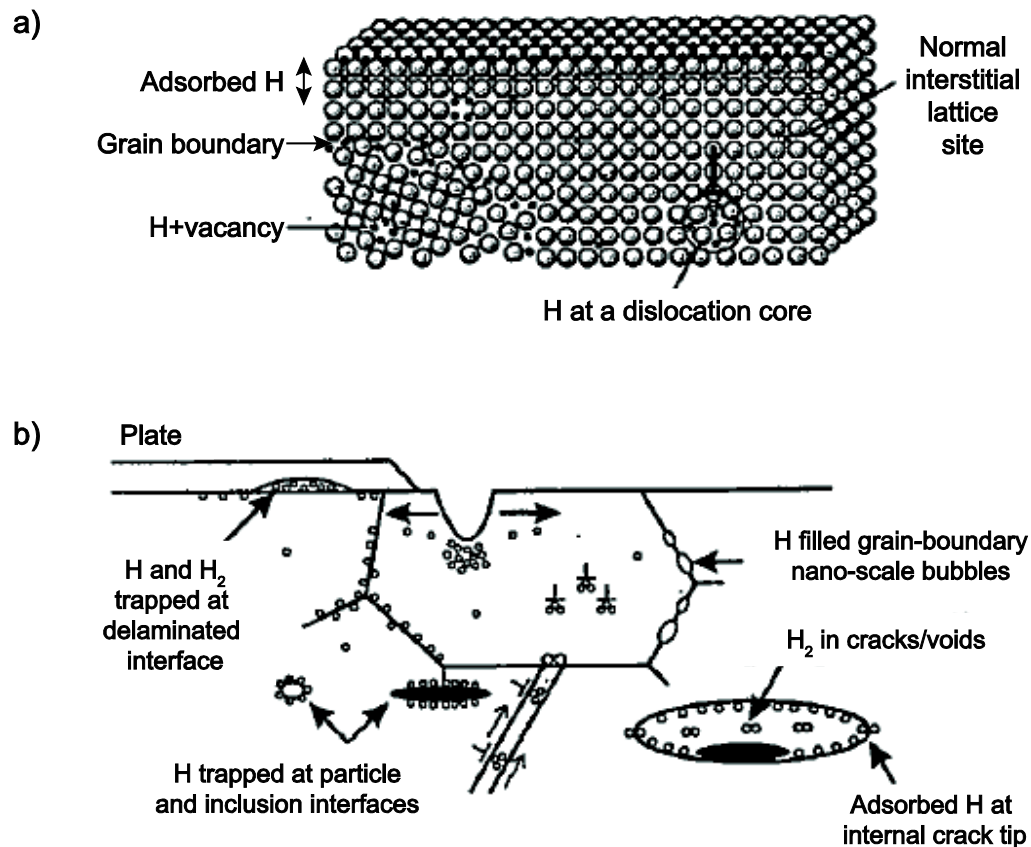


Figure 1.2. Schematic illustrations of sites and traps for hydrogen in materials: a) atomic scale (adopted from [8, 17]) b) microscopic scale (adopted from [17]).

In many cases, the binding energies of these traps overlap with each other making the precise identification of trap and detrapping energy difficult. For example, a hydrogen atom at the very core of a dislocation (iv) could be trapped with a higher energy than a H atom at a low-angle grain boundary (v). As the complexity of the microstructure increases, as is the case in ultrahigh-strength steels, the assignment of trapping sites becomes rather difficult. The most common defects that contribute to hydrogen trapping will be briefly discussed next.

### *Point defects*

Among the different point defects (such as vacancies and solute atoms), the most significant trap type is the vacancy. Not only can vacancies enhance embrittlement through agglomeration according to the HESIV model described above [5], they also have high binding energies with H compared to most alloying elements common in steels [15, 24]. For several metals, a decrease of the vacancy formation energy was observed in the presence of hydrogen, which leads to remarkably high vacancy concentrations. Superabundant vacancy formation occurred at high pressures and temperatures in Pd-H system, where vacancy concentrations of about 18% were

found [25] and in aluminum, where vacancy concentrations of about 23% were observed [26]. Similar behavior was observed in other metals such as Fe or Nb [27].

Together with vacancies, solute atoms provide reversible trapping sites for hydrogen. The interaction of solute atoms with hydrogen depends largely on both the type of solute atom and the metal matrix [24, 28-30].

#### *Dislocations*

The interaction of hydrogen with dislocations has a direct effect on the plastic flow properties of the material and hydrogen mobility. Edge dislocations exhibit a strong interaction with hydrogen atoms. In Pd, hydrogen is trapped in edge dislocations and an increase in hydrogen solubility is observed similar to the case with vacancies [8]. Hydrogen can be transported more rapidly when present in the surroundings of dislocations than through lattice diffusion. This becomes especially important when hydrogen is transported to grain boundaries thereby promoting intergranular (IG) fracture [17]. Trap binding energies of about 30 kJ/mol are commonly reported for H trapping in the elastic-strain field of a dislocation. The binding energy increases as H interacts with sites closer to the core, then binding energies of about 58 kJ/mol are reported for steels. Large dislocation densities in quenched steels are produced during the austenite-to-martensite transformation, this increases the trap density for these steels [23, 28].

#### *Grain boundaries*

As illustrated in Figure 1.1b, grain boundaries can act as traps for hydrogen and indeed hydrogen enrichment at grain boundaries is widely observed [8]. Hydrogen usually diffuses more rapidly along grain boundaries than through the lattice. But if there is a higher trap density in the grain boundaries than elsewhere in the lattice, then slower diffusion along the grain boundaries would be observed [17]. It was shown that impurity elements such as P or S that segregated at grain boundaries resulted in trapping of H at such grain boundaries. This leads to IG cracking along prior-austenite grain boundaries in high strength steels. The IG hydrogen failure likely involves reduced boundary cohesion due to segregation of hydrogen and impurities. Via a better control of the composition mainly through reducing the amount of impurity elements in high-strength and ultrahigh-strength steels, IG hydrogen embrittlement was reduced [31-34]. For the same type of steels the type of fracture can be transgranular (TG) or intergranular IG depending on the composition and heat treatment of the steels, which will result in different trap sites. TG fracture typically occurs in high-purity steels and in cases that H is segregated to other places than the grain boundaries, for example to FPZ upon stressing. [23, 34]. Low-angle grain boundaries have

lower binding energies with H than high-angle grain boundaries [23] and therefore IG failure is more likely in the latter case.

#### *Precipitate/matrix interfaces*

Matrix-precipitate interfaces can be reversible or irreversible traps depending on the size and coherency of the particles with the matrix. An irreversible trap with high trapping strength was illustrated in Figure 1.1a. The trapping strength is higher for coarse and incoherent precipitates than for smaller and coherent ones [28]. Titanium carbide, vanadium carbide and niobium carbide precipitates are known to trap hydrogen irreversibly and consequently reduce hydrogen embrittlement [35-38].  $M_2C$  precipitates common in precipitation hardened steels at their nominal tempering temperatures are reversible trapping sites for hydrogen. While these precipitates are responsible for the strength of the material (ultrahigh-strength steels), their reversible-trap nature leads to an enhancement of hydrogen embrittlement [23].

### **1.1.3. Effect of hydrogen concentration on hydrogen embrittlement**

The currently available hydrogen embrittlement models, HELP and HEDE, rely on the occurrence of diffusion of hydrogen to stressed regions within the lattice. The HESIV model also considers the diffusion of hydrogen, however, in this case it refers to the hydrogen that is reversibly trapped in vacancies [16]. In all the models for embrittlement, the amounts of H dissolved in the lattice and in reversible traps are of more importance than the overall H content in the material. This diffusible, diffusive or “free” hydrogen, as it is referred to in literature, is responsible for embrittlement phenomena.

The free hydrogen concentration has an effect on both the subcritical crack growth rate and the threshold stress intensity factor. For many steel grades including precipitation-hardened maraging steels it has been observed that for internal hydrogen assisted cracking the threshold intensity factor decreases as the free hydrogen concentration increases [6].

## **1.2. Scope of this thesis**

In view of what has been outlined so far, it is evident that developing an understanding about hydrogen interaction with different defects that act as traps is essential. These traps are responsible for the total hydrogen concentration within a microstructure as well as the diffusivity of hydrogen in the alloy. This is the main the reason why thermal desorption spectroscopy (TDS) has been widely used in investigating hydrogen traps present in alloys [8, 22, 38, 39]. This method is well-established and successful in identifying different binding energies of the traps with

hydrogen. Mechanical testing, on another end, is a direct measure of embrittlement but cannot determine trap types or the amount of hydrogen in the material. A direct observation of material can be provided by *in-situ* TEM, where evidence of the effect of hydrogen on fracture behavior and dislocation pile-ups is given [18].

In order to complement the above-mentioned methods, in this work, a non-destructive, fast and easy method is developed that could be used for screening the hydrogen uptake of alloys. An electrochemical method based on cyclic voltammetry (CV) is used to investigate the hydrogen absorption and desorption of different materials. With a theoretical detection limit of one hydrogen atom, the method is very useful in quantifying small amounts of hydrogen.

The method is established by studying the relatively simple Pd-alloys and several steel grades with complex microstructure and composition. The Pd-alloys were investigated in this study in order to:

- (i) develop the method using cyclic voltammetry (CV) as a tool to understand metal-hydrogen interactions using a relatively simple model system, and
- (ii) investigate the effect of solute atoms on the absorption/desorption properties of palladium for the application as membrane material for the separation of hydrogen from gas mixtures.

Next, the method was used to investigate more complex materials, i.e., a ball bearing steel, a twinning-induced plasticity steel and an ultra-high strength steel, that all have many applications in automotive and aerospace engineering. The focus is on the relation between hydrogen uptake and composition of the matrix along with heat treatments, that is, the microstructure.

### **1.3. Outline of this thesis**

In Chapter 2, the experimental set-up and the methodology used for the cyclic voltammetry (CV) technique as applied in this thesis are described. The hydrogen sorption and desorption related properties of Pd-alloys (Pd-Au and Pd-Mo-Cu) and pure Pd are investigated.

Chapter 3 mainly focuses on thermal H-desorption with a combined method of thermogravimetric analysis with mass spectrometer (TGA/MS). H-desorption from Pd, Pd-Au and Pd-Cu-Mo alloys was investigated and the role of water forming reactions in the route of H-desorption from different Pd-alloys was examined.

Chapter 4 focuses on Aermet 100 steel, an ultra-high strength steel developed for aerospace applications with a good combination of tensile strength and toughness, yet prone to H embrittlement. The material is investigated in two heat treatment states: (i) as-quenched – which mainly is a martensitic structure and (ii) aged – which consists of austenite and martensite. The hydrogen uptake is correlated both with the microstructure obtained by the different heat treatments and with the presence of alloying elements.

In Chapter 5, two other types of steels used for automotive applications are investigated. These are a bearing steel (SAE 52100) and an austenitic Mn-based twinning induced plasticity (TWIP) steel. Similar to Chapter 4, two different types of microstructures are compared in terms of their hydrogen sorption/desorption properties. For the ball-bearing steel, the effect of the presence of austenite was studied. For the TWIP steel, the effect of vanadium carbide precipitates was investigated. The main aim was to relate the absence and presence of austenite and precipitates on desorption of hydrogen.

## References

1. Johnson, W.H., *Nature*, 1875. **11**: p. 393.
2. Whiteman, M.B. and A.R. Troiano, *Corrosion*, 1965. **21**(2): p. 53-&.
3. Oriani, R.A. and P.H. Josephic, *Acta Metallurgica*, 1974. **22**(9): p. 1065-1074.
4. Birnbaum, H.K. and P. Sofronis, *Materials Science and Engineering a-Structural Materials Properties Microstructure and Processing*, 1994. **176**(1-2): p. 191-202.
5. Nagumo, M., *Materials Science and Technology*, 2004. **20**(8): p. 940-950.
6. Gangloff, R.P., *Hydrogen-assisted Cracking*, in *Comprehensive Structural Integrity*, I. Milne, R.O. Ritchie, and B. Karihaloo, Editors. 2003, Pergamon: Oxford. p. 31-101.
7. Mendes, D., et al., *Asia-Pacific Journal of Chemical Engineering*, 2010. **5**(1): p. 111-137.
8. Puntdt, A. and R. Kirchheim, *Annual Review of Materials Research*, 2006. **36**: p. 555-608.
9. Sakintuna, B., F. Lamari-Darkrim, and M. Hirscher, *International Journal of Hydrogen Energy*, 2007. **32**(9): p. 1121-1140.
10. *Technical System Targets: Onboard Hydrogen Storage for Light Duty Fuel Cell Vehicles*. [cited 2014 17 January ]; Available from: [http://www1.eere.energy.gov/hydrogenandfuelcells/storage/current\\_technology.html](http://www1.eere.energy.gov/hydrogenandfuelcells/storage/current_technology.html).
11. Hubert, T., et al., *Sensors and Actuators B-Chemical*, 2011. **157**(2): p. 329-352.
12. Hatlevik, O., et al., *Separation and Purification Technology*, 2010. **73**(1): p. 59-64.
13. Lu, G.Q., et al., *Journal of Colloid and Interface Science*, 2007. **314**(2): p. 589-603.
14. Nanu, D.E. and A.J. Bottger, *Advanced Functional Materials*, 2008. **18**(6): p. 898-906.
15. Barnoush, A., Saarland University, 2011.
16. Nagumo, M., *Isij International*, 2001. **41**(6): p. 590-598.
17. Lynch, S., *Corrosion Reviews*, 2012. **30**(3-4): p. 105-123.
18. Robertson, I.M., *Engineering Fracture Mechanics*, 2001. **68**(6): p. 671-692.
19. Lee, H.G. and J.Y. Lee, *Acta Metallurgica*, 1984. **32**(1): p. 131-136.
20. Takai, K. and R. Watanuki, *Isij International*, 2003. **43**(4): p. 520-526.
21. Choo, W.Y. and J.Y. Lee, *Metallurgical Transactions a-Physical Metallurgy and Materials Science*, 1982. **13**(1): p. 135-140.
22. Lee, J.Y. and S.M. Lee, *Surface & Coatings Technology*, 1986. **28**(3-4): p. 301-314.
23. Li, D.M., R.P. Gangloff, and J.R. Scully, *Metallurgical and Materials Transactions a-Physical Metallurgy and Materials Science*, 2004. **35A**(3): p. 849-864.
24. Counts, W.A., C. Wolverton, and R. Gibala, *Acta Materialia*, 2010. **58**(14): p. 4730-4741.
25. Fukai, Y. and N. Okuma, *Japanese Journal of Applied Physics Part 2-Letters*, 1993. **32**(9A): p. L1256-L1259.
26. Lu, G. and E. Kaziras, *Physical Review Letters*, 2005. **94**(15).
27. Fukai, Y., *Journal of Alloys and Compounds*, 2003. **356**: p. 263-269.
28. Thomas, R.L.S., et al., *Metallurgical and Materials Transactions a-Physical Metallurgy and Materials Science*, 2002. **33**(7): p. 1991-2004.
29. Uluc, A.V., et al., *Electrochimica Acta*, 2014. **submitted**.
30. Myers, S.M., et al., *Reviews of Modern Physics*, 1992. **64**(2): p. 559-617.
31. Pound, B.G., *Acta Metallurgica et Materialia*, 1990. **38**(12): p. 2373-2381.
32. Pound, B.G., *Acta Metallurgica et Materialia*, 1991. **39**(9): p. 2099-2105.
33. Pound, B.G., *Acta Materialia*, 1998. **46**(16): p. 5733-5743.
34. Thomas, R.L.S., J.R. Scully, and R.P. Gangloff, *Metallurgical and Materials Transactions a-Physical Metallurgy and Materials Science*, 2003. **34**(2): p. 327-344.
35. Takahashi, J., K. Kawakami, and T. Tarui, *Scripta Materialia*, 2012. **67**(2): p. 213-216.
36. Wei, F.G., T. Hara, and K. Tsuzaki, *Metallurgical and Materials Transactions B-Process Metallurgy and Materials Processing Science*, 2004. **35**(3): p. 587-597.
37. Yamasaki, S. and H.K.D.H. Bhadeshia, *Proceedings of the Royal Society a-Mathematical Physical and Engineering Sciences*, 2006. **462**(2072): p. 2315-2330.
38. Wei, F.G. and K. Tsuzaki, *Metallurgical and Materials Transactions a-Physical Metallurgy and Materials Science*, 2006. **37A**(2): p. 331-353.
39. Hashimoto, K. and M. Meshii, *Scripta Metallurgica*, 1985. **19**(9): p. 1075-1079.



# CHAPTER 2



# CHAPTER 2: Hydrogen Sorption and Desorption Related Properties of Pd-alloys Determined by Cyclic Voltammetry\*

---

*In this chapter we present a fast and quantitative electrochemical method – based on cyclic voltammetry (CV) – to screen the hydrogen (H) sorption (adsorption and/or absorption) and desorption behaviour of Pd-based alloys. The method consists of a first step in which specimens are potentiostatically loaded with H, followed by a second step in which a CV experiment is performed with a wide-range potential sweep. During the second step, oxidation of H occurs as well as the formation of oxides and their consequent reduction. The H-loading and the CV start potential are the same so that H oxidation is not influenced by other surface reactions as it is the first process to take place. The method is applied to different Pd-alloys (Pd-Au, Pd-Mo-Cu) and it enabled to elucidate the differences in H-sorption/desorption properties of the alloys. X-ray diffraction (XRD) and scanning electron microscopy (SEM) are used to investigate changes in the structure as a function of the H-loading times. It was shown with this work that (i) the phases present in the microstructure have a significant effect on the amount of hydrogen absorbed and the kinetics of absorption, (ii) even very small amounts of desorbed hydrogen can be detected by CV and (iii) alloying elements affect hydrogen sorption/desorption behaviour of Pd-based alloys and the bonding strength of H to the surface or in the bulk.*

---

## 2.1. Introduction

Palladium-based alloys are applied in membrane reactors to enhance the efficiency of industrially important chemical reactions [1-4] and in hydrogen production by steam reforming and water gas shift reaction [5-7]. Pd-alloys are also applied in thin film hydrogen sensors [8]. The lifetime and the performance, i.e. the permselectivity of membranes and the quality of sensors of Pd-based alloys is largely determined by hydrogen absorption and adsorption properties. The lifetime is mainly limited by hydrogen embrittlement when absorption of hydrogen causes hydride formation that is accompanied by large volume changes up to 10% (for pure Pd), causing

---

\* This chapter is based on:

Uluc, A. V., Mol, J. M. C., Terryn, H., Bottger, A. J. (2014). Hydrogen sorption and desorption related properties of Pd-alloys determined by cyclic voltammetry. *Journal of Electroanalytical Chemistry*, 734, 53-60.

microstructural changes and ultimately breakdown of the material [9]. The performance of Pd-based alloys, catalytic properties and sensing quality are influenced by surface poisoning [10-13] and in some cases by surface segregation [14, 15]. Both adsorption and absorption properties are affected by the amount and type of the alloying elements. H-embrittlement can be reduced by alloying because absorption properties are changed such that the formation of hydrides ( $\beta$ -phase) is prevented under given process conditions, i.e. when the material stays in the  $\alpha$  phase [9]. Alloying also changes adsorption properties which allows to reduce the susceptibility to surface poisoning [16] and to optimize the performance of sensors [17].

In this research an electrochemical approach was utilized to study the hydrogen sorption and desorption reactions of bulk Pd-Au and Pd-Mo-Cu alloys with several tens of micrometer thickness by combining potentiostatic loading with voltammetry. Alloys chosen are promising candidates for membrane technology, particularly for hydrogen gas purification due to their resistance to surface poisoning and H embrittlement. Cyclic voltammetry (CV) is a useful technique in studying sorption/desorption mechanism of hydrogen and oxygen on various materials [18]. This is mainly because it reveals information on these mechanisms through well studied reactions, e.g. formation of adsorbed hydrogen (Volmer adsorption) or electrochemical desorption of hydrogen into the solution (Heyrovsky desorption) in one relatively fast scan. Another advantage of the method is the possibility of detecting very low amounts of H in the material. Czerwinski et al. [19-21] investigated the absorption/desorption properties of hydrogen in Pd using CV in acidic and basic solutions. In these works the H-loading potential was related to the amount of H absorbed by the material; in their thin specimen the  $\alpha$  and  $\beta$  phases form and show two distinct peaks in the anodic oxidation region. Lukaszewski et al. [22-25] investigated the hydrogen absorption behavior and the chemistry of the surface oxides of Pd-Au alloys. They identified the Pd-rich and Au-rich oxide forming species by investigating the oxide reduction peak observed in the CV.

Although there has been extensive research in the past on H in Pd-alloys, still the effect of alloying on H absorption is unknown for a wide range of electrochemical H-loading durations including low H content region (at room temperature:  $\alpha$ -phase,  $[H]/[M] \leq 0.05$ ), the two phase region ( $\alpha + \beta$ -phase,  $0.05 \leq [H]/[M] \leq 0.6$ ) and the H saturation region ( $[H]/[M] \geq 0.6$ ). In this study a wide range of loading times is used, which allowed to distinguish the H-sorption behaviour of these alloys in the earlier stages when the system is not yet stable and later stages when the system reaches a steady state.

Different terms are generally used to describe the position or state of a hydrogen atom at the surface or in the bulk of material. In this chapter the following nomenclature was used: i) *Adsorption* refers to the accumulation of hydrogen (physisorbed or chemisorbed) at the surface and also includes the subsurface hydrogen, ii) *Absorption* refers to the initially adsorbed hydrogen that has diffused into the bulk of the lattice, iii) *Sorption* includes both adsorption and absorption phenomena and iv) *Desorption* is the inverse of sorption; it defines the hydrogen that leaves the system through the surface (with an oxidation reaction) of the sample and diffuses into the solution.

## 2.2. Experimental procedure

The materials used for this study were 50  $\mu\text{m}$  foils of pure Pd, Pd alloyed with Au ( $\text{Pd}_{95}\text{Au}_5$ ,  $\text{Pd}_{90}\text{Au}_{10}$ ,  $\text{Pd}_{75}\text{Au}_{25}$ ) and Pd alloyed with Mo and Cu ( $\text{Pd}_{85}\text{Mo}_{10}\text{Cu}_5$ ). The foils were obtained from Philips Research Laboratories in Eindhoven, The Netherlands. The samples were prepared from these foils by cutting pieces of 5 mm x 10 mm. Samples were attached to a steel wire by spot welding. The connection and the part of the wire that was inside the solution were painted with a lacquer resistant at highly basic solution. Prior to painting, both sides of the sample were washed first with acetone and then with ethanol, followed by drying with  $\text{N}_2$ , in order to dissolve any grease or similar contamination. The reference electrode was a saturated standard calomel electrode (SCE) and the electrolyte used was a 1 M KOH (Sigma Aldrich, purity  $\geq 85\%$ , pH  $\sim 13.1$ ) solution. Finally, platinum was used as the counter electrode. Although in some cases [22-25] the solution is deaerated by bubbling Ar or  $\text{N}_2$  gas prior to and/or during the experiment, our experiments were performed without bubbling gas since no effect of deaeration on results was found.

For the cyclic voltammetry experiments, a Potentiostat Autolab PGSTAT 12 was used. During the experiments, the potential was swept between -1.2 V to 0.5 V with a sweep rate of 0.01 V/s and starting at -1.2 V. The potentiostatic H-loading potential was selected as -1.2 V. Loading times were varied from 25 s to 8 h, so that the hydrogen adsorption/absorption behavior of the materials in  $\alpha$ -,  $\alpha+\beta$ - and  $\beta$ -phases is covered. The sequence of the electrochemical experiments is shown schematically in Figure 2.1 and was as follows: (1) two repeated cycles of CV (Figure 2.1a and Figure 2.1b) (2) potentiostatic hydrogen loading at -1.2 V and (3) two repeated cycles of CV (Figure 1c and Figure 1d). The sample was not removed from the solution in between the steps mentioned above and the temperature was fixed at 300 K. All potentials are referred to SCE in this thesis. Traditionally, the current density in CV experiments is expressed per unit area ( $\text{A}/\text{cm}^2$ ). Since the amount of hydrogen absorbed depends also on the volume of the Pd samples,

the data are expressed per unit volume ( $\text{A}/\text{cm}^3$ ) to take into account the effect of small volume differences between the samples.

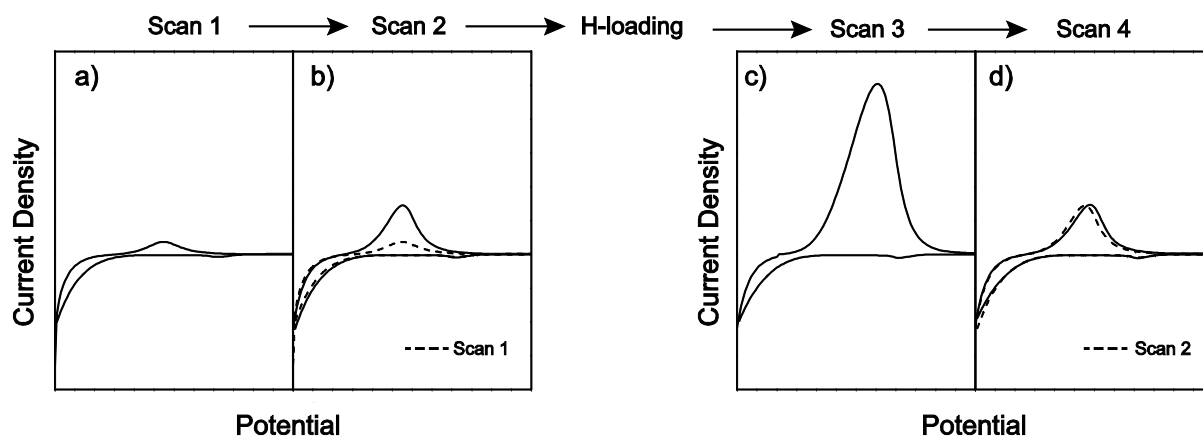


Figure 2.1. Experimental scheme: CV scans before H-loading a) Scan 1, regarded as a cleaning/reference step; b) Scan 2; CV scans after H-loading c) Scan 3; d) Scan 4.

X-Ray diffraction (XRD) was used to determine the phases present in the material upon different H-loading times. X-ray powder diffraction (XRPD) patterns were recorded in a Bragg-Brentano geometry in a Bruker D8 Advance diffractometer equipped with a Vantec position sensitive detector and graphite monochromator [26]. Data collection was carried out at room temperature using monochromatic Co  $K\alpha$  radiation ( $\lambda = 0.179026$  nm) in the  $2\theta$  region between  $40^\circ$  and  $140^\circ$ , step size  $0.04^\circ 2\theta$  and measuring time per step 2 s. The samples were placed on a Si {510} substrate and rotated during measurement. Scanning Electron Microscope (SEM) was utilized to investigate surface related changes (e.g. segregation) upon H-loading. The SEM was a JEOL JSM 6500F from Japan Electron Optics Ltd with a hot field emission gun and is equipped with a Thermo Fisher Ultradry EDS detector with Noran System 7 data-acquisition and data-analysis software. The backscattered electron detector (BSE) was an Autrata type.

### 2.3. Results and discussion

In this section the results of the electrochemical methods that were applied on Pd, Pd-Au and Pd-Mo-Cu will be presented and discussed. The range of alloying was chosen such that both the single phase ( $\text{Pd}_{75}\text{Au}_{25}$  and  $\text{Pd}_{85}\text{Mo}_{10}\text{Cu}_5$ ) and two-phase ( $\text{Pd}_{95}\text{Au}_5$  and  $\text{Pd}_{90}\text{Au}_{10}$ ) systems were investigated. A wide range of potentiostatic loading times were applied in order to gain knowledge on both adsorption and absorption related properties of Pd-alloys. In the following sections, before going into a detailed discussion on H adsorption/absorption properties of different alloys, a description of a typical CV scan will be given with the definitions of different regions, including the reactions taking place. Next, the method for quantification for both the CV

scans and potentiostatic loading curves will be described. This will be followed by a discussion on H sorption/desorption properties of the Pd-alloys.

### 2.3.1. Description of a CV scan for Pd-alloys

A typical CV curve for Pd<sub>95</sub>Au<sub>5</sub> is given in Figure 2.2. Hydrogen evolution and/or adsorption takes place at Region 1 and Region 3, whereas H-desorption (oxidation) occurs in Region 2.

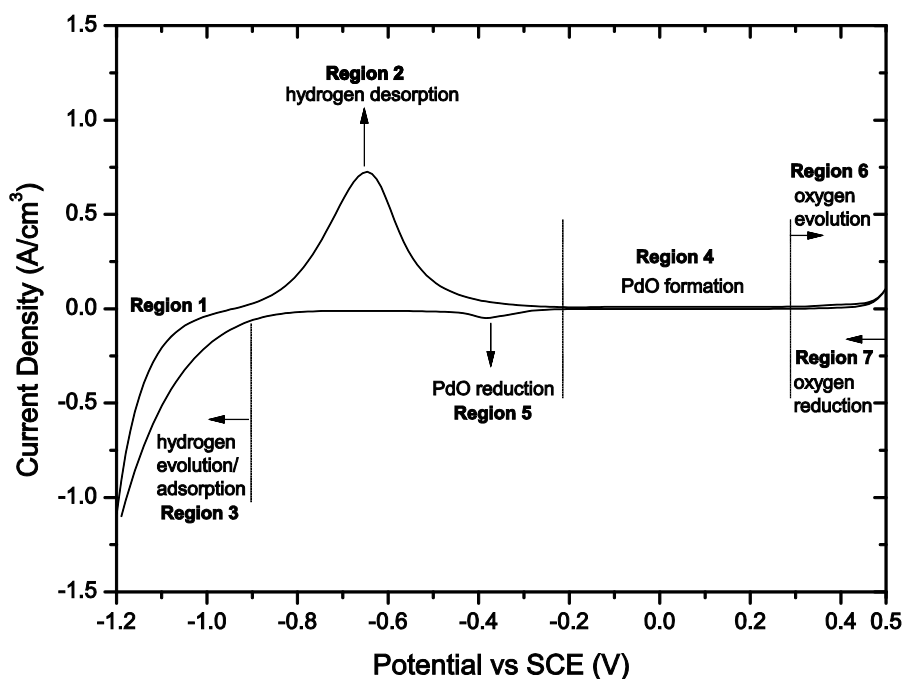


Figure 2.2. A typical CV scan performed on Pd<sub>95</sub>Au<sub>5</sub> in a 1M KOH solution. Starting and switching potentials are -1.2 V and 0.5 V, respectively. Sweep rate is 0.01 V/s. Different reaction regions of hydrogen evolution/adsorption (Region 1 and Region 3), hydrogen desorption (Region 2), PdO oxidation and reduction (Region 4 and 5, respectively) and oxygen evolution (Region 6) are shown.

Region 1 in Figure 2.2 shows that the current is negative and decreasing. In this region, the discharge of H<sub>2</sub>O occurs (Volmer reaction) which results in hydrogen adsorption on the electrode surface according to Eq. (1). This reaction takes place around a potential of -1.068 V vs. SCE in a solution of pH 13.1 [27]. This is the main reason for selecting a potentiostatic H-loading potential of -1.2 V, i.e. to ensure that the Volmer reaction takes place on the surface of the working electrode.



The adsorbed hydrogen can either diffuse into the bulk through absorption (Eq. (2)),



or it can recombine with another adsorbed H atom (Tafel reaction) and diffuse away from the surface as is given in Eq. (3):



Sweeping the potential from Region 1 towards Region 2, once the current is in the anodic region, the hydrogen that was adsorbed and/or absorbed in Region 1 starts to desorb, forming the hydrogen desorption peak. Sweeping the potential further until the switching potential ( $E_s=0.5$  V) leads to PdO formation (Region 4 in Figure 2.2) and oxygen evolution (Region 5 in Figure 2.2). During the reverse scan, oxygen and PdO reduction takes place on the electrode surface (Region 7 and Region 5 in Figure 2.2, respectively). This is followed by Region 3, where similar to Region 1, hydrogen is produced which can adsorb on the surface. Regarding the regions related to hydrogen sorption/desorption, Region 1 and Region 3 can be used to calculate the total amount of hydrogen evolved ( $\text{H}_2$  gas and the hydrogen that is adsorbed) at the electrode surface and Region 2 is used to determine the amount that desorb out of the system.

### 2.3.2. Quantification of adsorbed and absorbed hydrogen for Pd-alloys

To quantify the amount of hydrogen that is sorbed and to establish if all the hydrogen that is evolved on the surface does sorb/desorb, the total charge  $Q$  (in C) involved in the reactions of Region 1, Region 2 and Region 3 are compared.  $Q$  is calculated by integrating the  $I(t)$  after converting the potential axis of Figure 2.2 to time axis as in Eq. (4) :

$$t = \frac{|E(t) - E_i|}{\nu} \quad (4)$$

where  $E(t)$  is the potential at time  $t$  (V),  $E_i$  is the initial/starting potential (V),  $\nu$  is the sweep rate (V/s) and  $t$  is time (s). The  $E_i$  term in Eq. (4) is replaced by the switching potential  $E_s$  for the reverse scan.

The total charge  $Q$  calculated by integration of  $I(t)$  is then used to calculate the amount of hydrogen. This implicitly assumes that each electron reacts with 1 H atom according to Eq. (1). If all the hydrogen atoms evolved are sorbed and also completely desorbed, then the following equations regarding Scan 1 and Scan 2 (see Figure 2.1a and Figure 2.1b) should hold:

$$(Q \text{ of Region } 1^{\text{scan } 1}) = (Q \text{ of Region } 2^{\text{scan } 1}) \quad (5)$$

$$(Q \text{ of Region } 3^{\text{scan } 1}) + (Q \text{ of Region } 1^{\text{scan } 2}) = (Q \text{ of Region } 2^{\text{scan } 2}) \quad (6)$$

After potentiostatic H-loading takes place, it should hold that:

$$(\text{Q of hydrogen loading curve}) + (\text{Q of Region 1}^{scan\ 3}) = (\text{Q of Region 2}^{scan\ 3}) \quad (7)$$

The left side of these equations shows the total charges related to hydrogen evolution (adsorbed and/or evolved) and those on the right side are due to H-desorption. The comparison of the left and right side of Eq. (5) and Eq. (6) averaged for 20 measurements shows that for scan 1, the difference between the total Q related to H evolution and H desorption is about 34%, whereas this difference for scan 2 is only 6%. The higher difference between the anodic and cathodic regions of scan 1 is attributed to the presence of contamination or oxide layers on the surface that reduce the sorption of hydrogen. It is also observed that the peak potential  $E_p$  of the hydrogen desorption peak (Region 2 in Figure 2.2) of scan 1 and scan 2 are the same (-0.65 V vs. SCE). However, the total Q differs for these two scans (i.e., larger Q for scan 2), pointing to a larger amount of H adsorbed [18].

Similar to calculating the amount of H desorbing from the sample using the CV curves, integration of  $I(t)$  vs. time plot of the potentiostatic loading curve was used to calculate the amount of hydrogen evolved during H-loading. The loading curves for the Pd-Au alloys are shown in Figure 2.3. The loading curves of Pd<sub>75</sub>Au<sub>25</sub> presented in Figure 2.3c show different characteristics than that of Pd<sub>95</sub>Au<sub>5</sub> and Pd<sub>90</sub>Au<sub>10</sub> (Figure 2.3a and Figure 2.3b, respectively). The Pd<sub>95</sub>Au<sub>5</sub> and Pd<sub>90</sub>Au<sub>10</sub> samples show a region with slightly higher current densities (see arrows), whereas the Pd<sub>75</sub>Au<sub>25</sub> sample does not show such region. The changes in the current (and hence the absorption property) are related to the phases present in the material as will be shown next. Different stages of the loading curves can be related to different phases as the  $\alpha_{max}$  and  $\beta_{min}$  concentrations correspond to the charges in relation with inflexion points on the loading curves as shown by Lukaszewski et al. (Pd-Au and Pd-Pt) [28] and Hubkowska et al. (Pd-Ru) [29]. In the current work, direct phase identification was performed by means of X-ray diffraction at selected points (times of loading) of the loading curve. Figure 2.4 shows the diffraction patterns of Pd<sub>95</sub>Au<sub>5</sub> samples for different H-loading times. In Figure 2.4a, the diffraction pattern of a fresh sample (before performing CV) is shown where the material is in the  $\alpha$ -phase. The material is in the face-centered-cubic (FCC) structure and H is expected to fill the interstitial sites upon loading. The XRD pattern for 500 s H-loading (Figure 2.4b), is very similar to the diffraction pattern before loading, no additional diffraction peaks are observed. The 500 s loading corresponds to the initial part of the potentiostatic loading curve, where the current is abruptly decreasing, as indicated with an arrow in Figure 2.3a.

In this region, the material is still in the  $\alpha$ -phase and calculation of the hydrogen amount by means of XRD is difficult since a remarkable shift in diffraction peaks is not observed. The  $\alpha \rightarrow \beta$

transition has started to take place for loading times around 1000 s. Diffraction patterns obtained at this stage of loading show the appearance of the  $\beta$  -{200} reflection next to the  $\alpha$ -{200} reflection indicated by an arrow in Figure 2.4c.

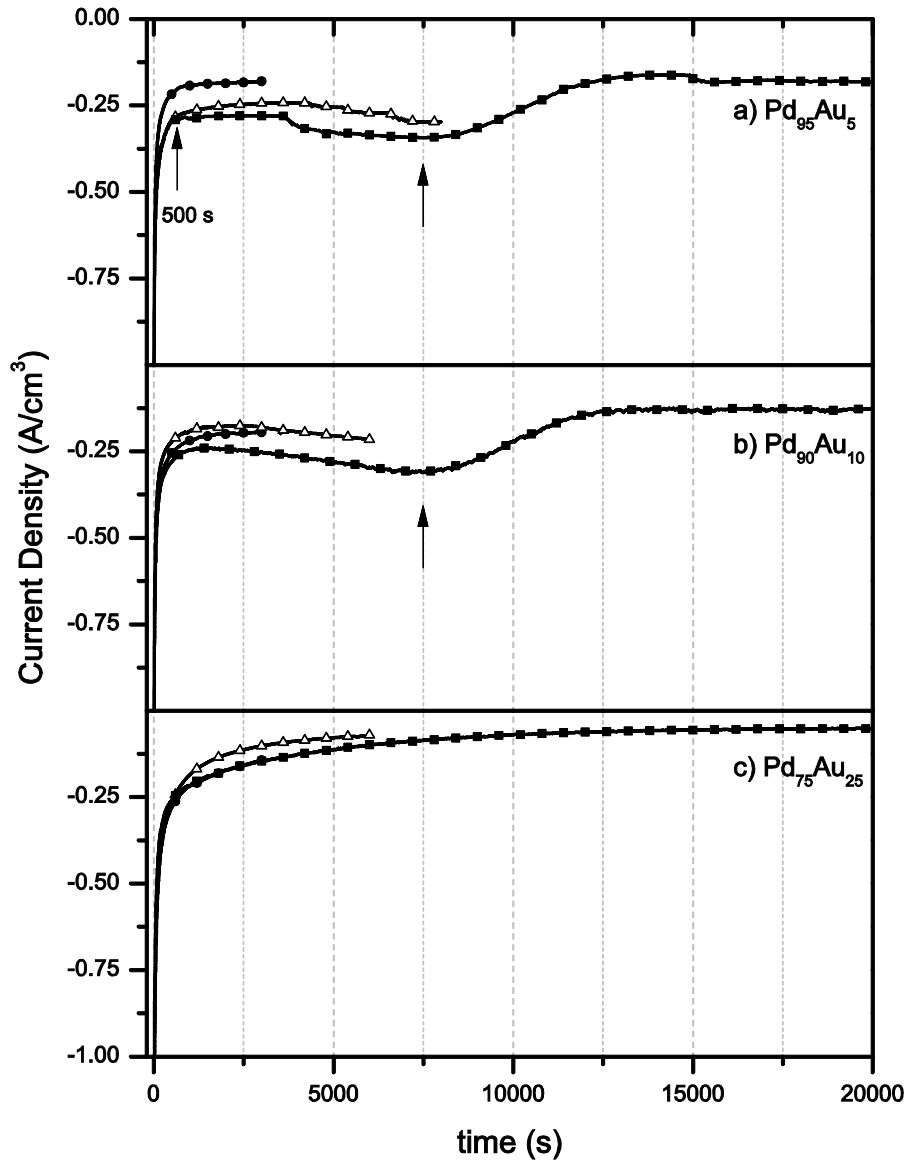


Figure 2.3. Potentiostatic H-loading curves at -1.2 V for a) Pd<sub>95</sub>Au<sub>5</sub> b) Pd<sub>90</sub>Au<sub>10</sub> c) Pd<sub>75</sub>Au<sub>25</sub>. The loading current goes through an increasing region followed by a decreasing trend in Pd<sub>95</sub>Au<sub>5</sub> and Pd<sub>90</sub>Au<sub>10</sub> samples associated with the  $\alpha \rightarrow \beta$  transition. The Pd<sub>75</sub>Au<sub>25</sub> alloy, however, does not show this behavior (stays in the one phase region throughout loading).

The results of XRD when H-loading was performed for 2500 s and 10000 s, which both corresponds to the higher current region of the loading curve (see arrows in Figure 2.3a and Figure 2.3b), are shown in Figure 2.4c and Figure 2.4d. It is clearly seen that the  $\alpha$  and  $\beta$  phases coexist for these loading times and that the amount of  $\beta$ -phase increases in time, as indicated by a higher peak area of the  $\beta$ -phase for 10000 s loading than 2500 s loading. For longer loading times

(Figure 2.4f) all the  $\alpha$ -phase has transformed into the  $\beta$ -phase. The  $\text{Pd}_{75}\text{Au}_{25}$  alloy does not show similar behavior of a change in the current density (see Figure 2.3c) which suggests that this material stays in the one phase ( $\alpha$ -phase) region throughout the loading. The corresponding H contents by means of CV will be discussed in the next sections.

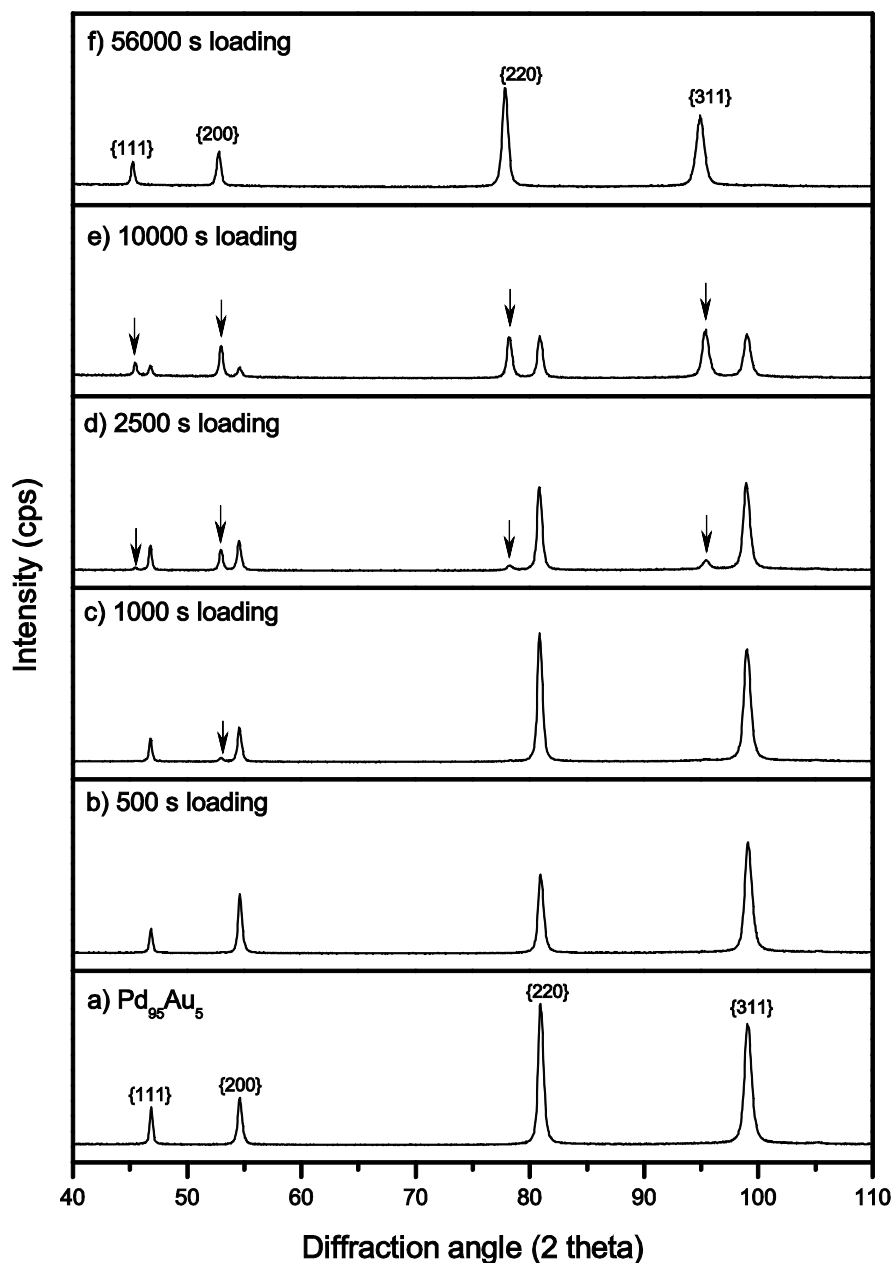


Figure 2.4. XRD patterns of  $\text{Pd}_{95}\text{Au}_5$  samples after different H loading times. a)  $\text{Pd}_{95}\text{Au}_5$  alloy showing FCC  $\alpha$ -phase peaks. b) After 500 s loading, the material is still in the  $\alpha$ -phase,  $[\text{H}]/[\text{Pd}]$  cannot be calculated by XRD since a remarkable shift in peaks is not observed). c) For the 1000 s loaded sample, the formation of  $\beta$ -phase (see arrow)  $[\text{H}]/[\text{Pd}] \sim 0.46$ . d) After 2500 s loading  $[\text{H}]/[\text{Pd}] \sim 0.46$  and e) 10000 s loading  $[\text{H}]/[\text{Pd}] \sim 0.46$ , the  $\beta$ -phase amount is increasing indicated by bigger  $\beta$ -phase peaks f) for a sample that was 56000 s loaded  $[\text{H}]/[\text{Pd}] \sim 0.52$ , only the  $\beta$ -phase peaks are visible, indicating that the  $\alpha \rightarrow \beta$  transformation is complete.

### 2.3.3. Adsorption vs absorption in the $\alpha$ -phase

The hydrogen desorption peak of the second scan is due to the total hydrogen sorbed during Region 3 in the first scan and Region 1 in the second scan (see Figure 2.2). Since the amount of total hydrogen generated in these regions is very small, the second scans of Pd-alloys can be used to differentiate the adsorption properties of the materials. To determine if absorption readily occurs during the second scan, the number of hydrogen sites available on the sample surface and the amount of H evolved during the second scan was compared. Assuming a {111} orientation on the Pd surface and 1 H/Pd adsorption ratio on the surface [30], there are  $3.79 \times 10^{14}$  Pd sites available for H adsorption. The amount of hydrogen produced at the surface was calculated to be  $1.41 \times 10^{17}$  atoms (see Eq. 6 and section 3.2 for information about the quantification method). This indicates that, even in Region 1 of the second scan when there is no H-loading performed on purpose, all the sites available for H near the surface are full. This means that, even in the very low H-loading amounts, absorption has started.

Figure 2.5a shows a correlation between the mean peak potential of the hydrogen desorption peak and the percentage of Au in the Pd-Au alloy.

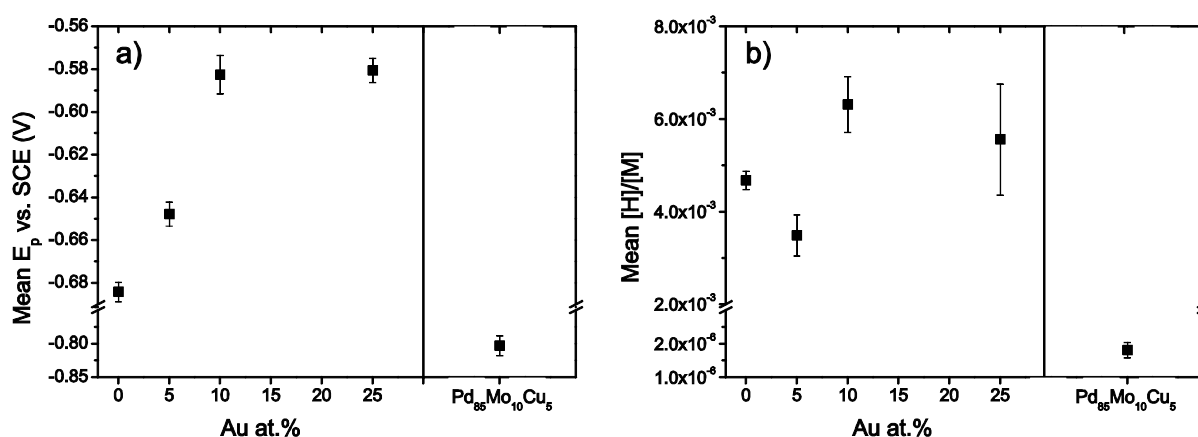


Figure 2.5. a) The mean peak potentials b) The mean  $[H]/[M]$  of minimum 20 measurements for Pd-Au and Pd-Cu-Mo systems. The second scans were used to determine the values.

When the amount of Au in the alloys is small (Pd and Pd<sub>95</sub>Au<sub>5</sub>), the mean peak potential is significantly more cathodic compared to that of Pd-alloys of higher Au content. The more anodic peak potential of Pd<sub>90</sub>Au<sub>10</sub> and Pd<sub>75</sub>Au<sub>25</sub> samples could point to mainly three possibilities: (i) higher Au% samples sorb higher amounts of hydrogen and thus a longer time period is required to strip it all out; (ii) H diffusivity gets smaller with increasing Au% [31] so a longer time period is required for H to diffuse to the surface; or (iii) hydrogen is more strongly bound to the surface/bulk so that it is energetically more difficult to remove from the material. If the first option is correct, then the mean hydrogen content  $[H]/[M]$  should have the same trend as the

mean peak potential with amount of Au in the Pd-Au alloy. However, it is shown in Figure 2.5b that there is no clear correlation between the H content and the amount of Au in the alloy. In fact, for short loading times, the  $[H]/[M]$  is highest for Pd<sub>90</sub>Au<sub>10</sub>, somewhat lower for Pd<sub>75</sub>Au<sub>25</sub> followed by pure Pd and smallest for Pd<sub>95</sub>Au<sub>5</sub>. Thus, the first option can be eliminated. The second and third options both remain as possible explanations. They are both feasible explanations. According to the third option, the peak shift is related to the interaction strength between the hydrogen and the surface or bulk sites of the alloy. As seen in Figure 2.5a, this would suggest that the hydrogen is attached more strongly as the amount of Au in the alloys is increased. This is in good agreement with density functional calculations of Sonwane et al. [32, 33], where the binding energies of hydrogen to the octahedral sites are calculated to be higher for Pd-Au alloys and lower for Pd-Cu alloys, with respect to pure Pd. For Pd-Cu-Mo system, the mean peak potential is the most cathodic one, and the hydrogen amount that is sorbed in the system is significantly lower than the Pd-Au alloys.

### 2.3.4. Hydrogen in the $\alpha+\beta$ and $\beta$ phase regions

The CV scans of Pd alloys after H-loading up to 1000 s at -1.2 V are shown in Figure 2.6.

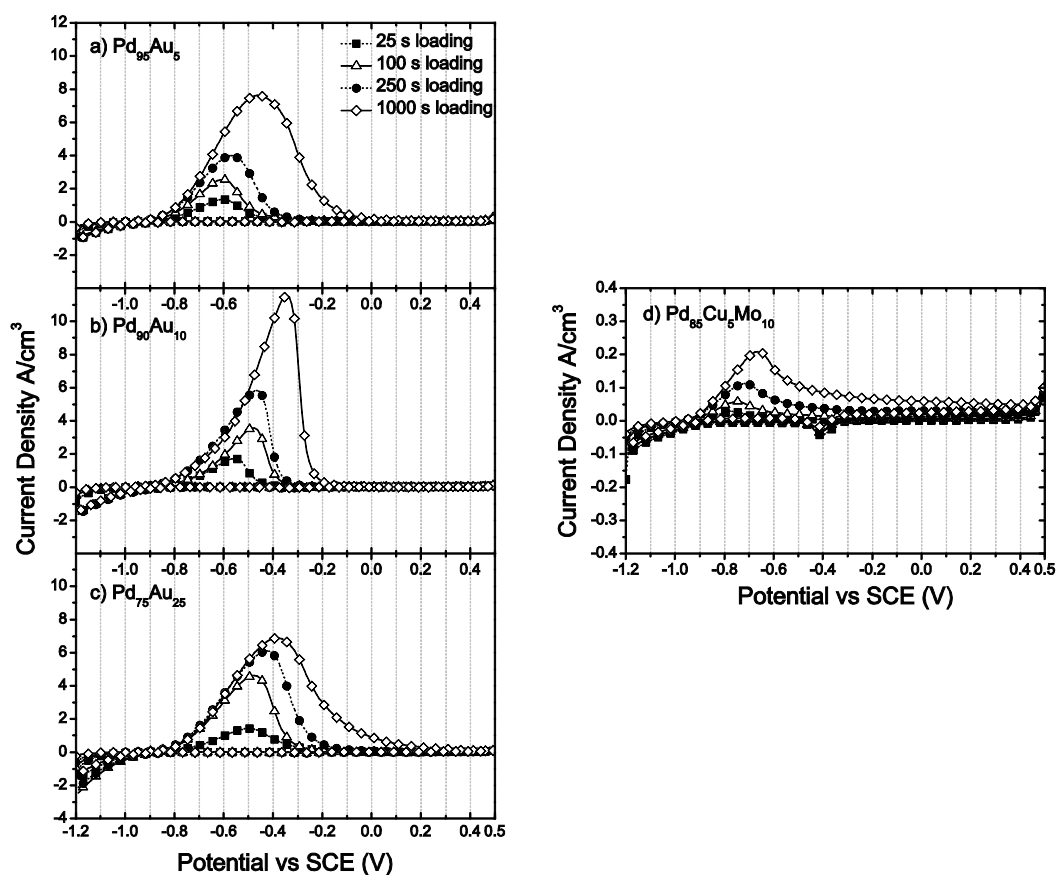


Figure 2.6. CV scans of Pd-Au and Pd-Cu-Mo alloys after potentiostatic loading at -1.2 V for loading times between 25 s – 1000 s. a) Pd<sub>95</sub>Au<sub>5</sub> b) Pd<sub>90</sub>Au<sub>10</sub> c) Pd<sub>75</sub>Au<sub>25</sub> d) Pd<sub>85</sub>Mo<sub>10</sub>Cu<sub>5</sub>.

The direct observation for all materials is the shift of  $E_p$  to more anodic potentials as the loading time increases. This is because the potential axis of a CV curve can also be considered as a time axis. As the time of loading increases, there is more time needed to strip the H out of the samples. Also, the  $\beta$ -phase (once formed) needs to decompose into the  $\alpha$ -phase during unloading which additionally could contribute to the time delay. It is also seen that different Pd-Au alloys with different percentages of Au have distinctly different shapes. While CV scans of Pd<sub>95</sub>Au<sub>5</sub> look rather symmetrical in peak shape, the Pd<sub>90</sub>Au<sub>10</sub> alloy shows a tail at the beginning of the hydrogen desorption peak whereas the Pd<sub>75</sub>Au<sub>25</sub> shows a tail at the end. In Figure 2.6d, the CV scans for Pd-Cu-Mo system is also shown for the same loading times. The shape in this case also consists of a hydrogen desorption peak with a tail at the end. Additionally, a high oxidation current is observed on the cathodic region right after the hydrogen desorption peak. This oxidation reaction prevents the hydrogen desorption peak current to drop to low values which makes the calculation of the hydrogen amount more difficult. In this case, by subtracting the charges (Q) involved in the reduction of PdO in the reverse scan from the total Q of hydrogen desorption of the forward scan, the hydrogen amounts were estimated.

As stated previously, the amount of hydrogen produced during potentiostatic loading can be compared with the hydrogen desorbing from the specimen during CV. The results for Pd<sub>95</sub>Au<sub>5</sub> and Pd<sub>75</sub>Au<sub>25</sub> for loading times up to 60000 s are given in Figure 2.7. As the loading time increases, the total hydrogen evolved also increases as expected. For the Pd<sub>95</sub>Au<sub>5</sub> (Figure 2.7a) the amount of H desorbed however first increases but then remains constant after loading times of about 10000 s. Initially almost all the H produced also desorbs (91%), implying that almost all the H has been absorbed.

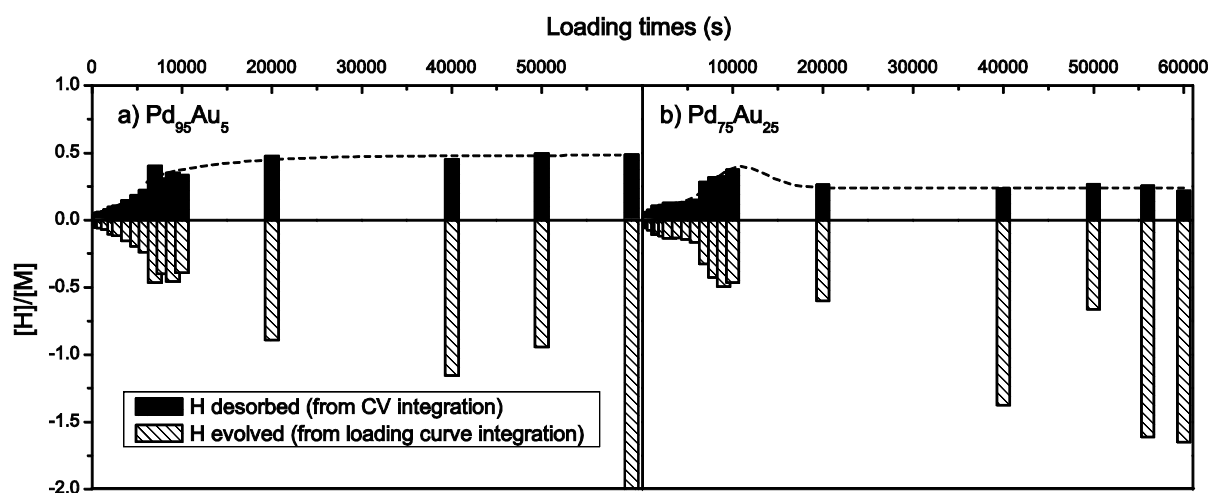


Figure 2.7. Amount of Hydrogen evolved during loading and amount of hydrogen desorbed during CV expressed as  $[H]/[M]$  for different loading times of a) Pd<sub>95</sub>Au<sub>5</sub> and b) Pd<sub>75</sub>Au<sub>25</sub>.

After longer loading times ( $>10000$  s) the material is saturated with H (about  $0.5 [H]/[M]$ ), the amount of desorbed H does not increase anymore, indicating that the material has absorbed the maximum amount of hydrogen for the given conditions. Similarly for the  $\text{Pd}_{75}\text{Au}_{25}$  samples initially (loading time  $<10000$  s) there is an increase in the area of the desorption peak. After  $10000$  s of loading, which corresponds to about  $0.3 [H]/[M]$ , there is a drop in the amount of desorbed H (down to about  $0.25 [H]/[M]$ ) and from then on that amount stays constant for all longer loading times. This reduction of desorbed H for  $\text{Pd}_{75}\text{Au}_{25}$  after longer loading times is so far not understood. Both surface segregation and changes in the amount of defects in the material were investigated. Surface segregation (of Au) could hinder the dissociation of  $\text{H}_2$  and therefore reduce the absorption of H atoms. Changes in the defect amount and type could lead to a reduction of the amount of desorbed H since defects could be traps for H. No surface segregation of Au [14, 34] was observed by means of SEM. BSE data were used to first visually determine the Au-rich regions (higher brightness due to its higher weight than the Pd atoms) and then EDS was used to quantify the Pd:Au ratio. Analysis of the surface of  $\text{Pd}_{75}\text{Au}_{25}$  with this method showed that a few Au-rich regions were present on the surface for both as-received material as well as the samples that were loaded longer than  $20000$  s. But no clear increase of the amount of Au-rich regions was found. Changes in the amount or type of defects were also monitored by looking at XRD profiles and their line widths that in principle reflect local changes in the crystal structure [35], but no changes were found. Although experimentally not observed, our calculations based on work of Tomanek et al. [36] showed that segregation of Au to the surface of  $\text{Pd}_{75}\text{Au}_{25}$  sample is expected to be more pronounced than for lower Au content samples. To summarize, even though proof of Au segregation was not found on the surface of  $\text{Pd}_{75}\text{Au}_{25}$  samples, the possibility cannot be ruled out as an explanation of the observed difference between the hydrogen evolved during loading and the hydrogen desorbed from  $\text{Pd}_{75}\text{Au}_{25}$  alloys.

Next, the relation between the amount of H desorbed as a function of loading time will be discussed. In Figure 2.8a-c, the amount of desorbed H after various loading times for the Pd-Au alloys is presented. In Figure 2.8a the results for the low H-loading times (up to  $3000$  s) are collected. Clearly, the  $\text{Pd}_{75}\text{Au}_{25}$  sample absorbs the highest amount of hydrogen for the low loading times, however Figure 2.8b shows that for higher loading times the  $\text{Pd}_{75}\text{Au}_{25}$  samples desorbs less hydrogen than  $\text{Pd}_5\text{Au}_{95}$  and  $\text{Pd}_{10}\text{Au}_{90}$ . During the initial stages of H absorption where the system is away from a steady state, the H-absorption of different alloys is determined by reduction kinetics. This is reflected in the amounts of hydrogen evolved as shown in Figure 2.7. For H-loadings up to  $3000$  s, the amount of hydrogen evolved is higher for  $\text{Pd}_{75}\text{Au}_{25}$  than for  $\text{Pd}_{95}\text{Au}_5$ . This suggests that the  $\text{H}^+$  reduction at the surface of the  $\text{Pd}_{75}\text{Au}_{25}$  alloy is faster than the

$\text{Pd}_{95}\text{Au}_5$  alloy. The amount of H eventually absorbed by the system is determined by thermodynamics. It is well known that the number of interstitial sites available for hydrogen decreases as the Au content in Pd increases [37, 38], because the sites close to Au atoms are energetically less favorable for H. In particular, in Nanu et al. [38] the analysis of atom configurations by means of neutron diffraction showed that when the amount of Au in the Pd-based alloy is increased, also tetrahedral sites in the vicinity of Au atoms are occupied, whereas in pure Pd only octahedral interstitial site are occupied by H.

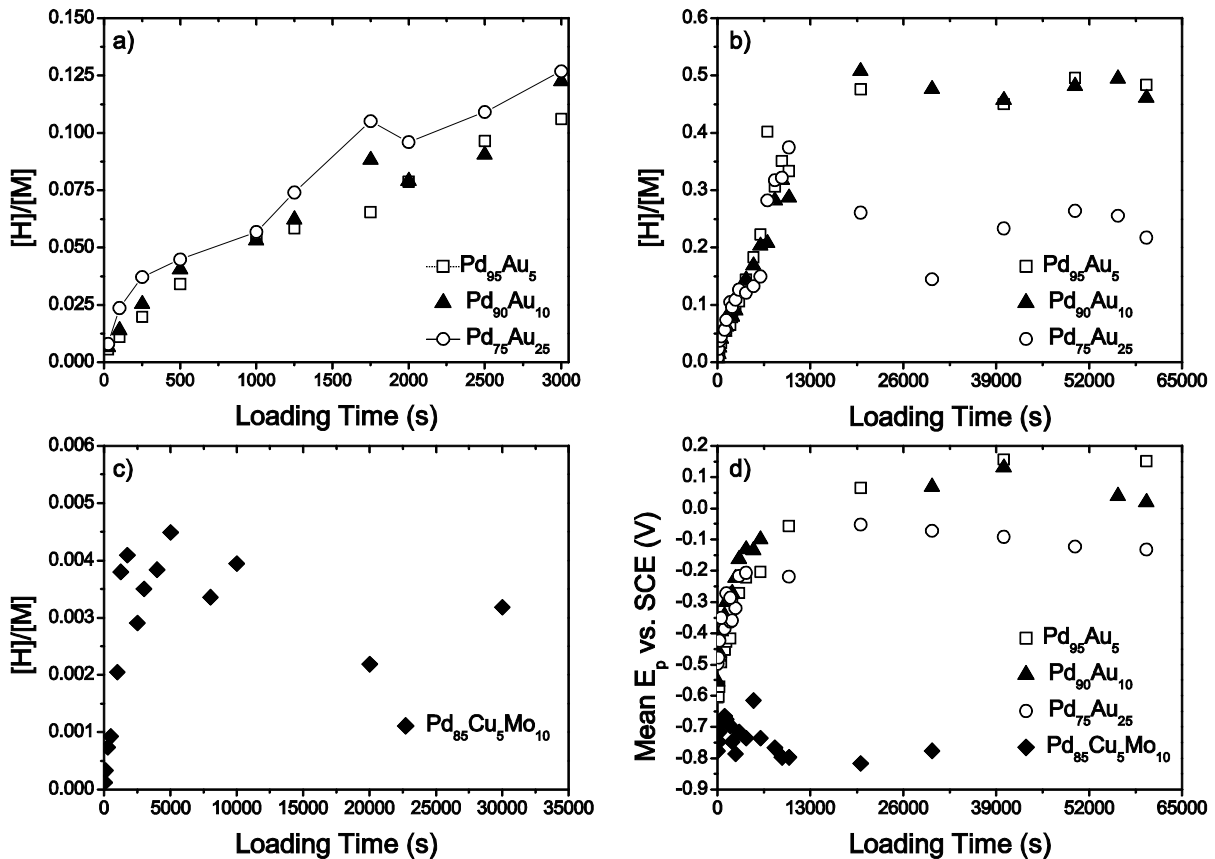


Figure 2.8. Hydrogen content ( $[\text{H}]/[\text{M}]$ ) and peak potential ( $E_p$ ) vs. loading time for  $\text{Pd}_{95}\text{Au}_5$ ,  $\text{Pd}_{90}\text{Au}_{10}$ ,  $\text{Pd}_{75}\text{Au}_{25}$  and  $\text{Pd}_{85}\text{Mo}_{10}\text{Cu}_5$ . a)  $[\text{H}]/[\text{M}]$  for Pd-Au alloys with loading times at and below 3000 s, b)  $[\text{H}]/[\text{M}]$  for Pd-Au alloys showing all loading times, c)  $[\text{H}]/[\text{M}]$  for  $\text{Pd}_{85}\text{Mo}_{10}\text{Cu}_5$  alloy showing all loading times, d)  $E_p$  vs. loading time for Pd-Au alloys.

Moreover the local configuration of Au atoms around an octahedral site matters. This is consistent with the neutron diffraction experiments [37] and Mössbauer spectroscopy results [39] that indicated that the H atoms are repelled by Au atoms and consequently the interstitial sites in the vicinity of Au atoms are not preferably occupied by H atoms. The  $\text{Pd}_{95}\text{Au}_5$  material absorbs less hydrogen than  $\text{Pd}_{90}\text{Au}_{10}$  for loadings up to 3000 s (because of kinetics) but eventually higher amounts of hydrogen are absorbed, as is in accordance with the phase diagram [40]. In Figure 2.8d, the mean peak potential ( $E_p$ ) as a function of loading time is presented for Pd-Au alloys. In

contrast with Figure 2.5a (for low loading times), here the  $E_p$  is shifted to more cathodic potentials with increasing Au content. Lukaszewski et al. in their work [23] observed similar behavior and attributed the easier H-oxidation of Au-richer alloys to be kinetically originated by a probable change on the surface or the bulk characteristics of the samples upon Au% increase. Our results presented in Figure 2.8b indicate that the amount of  $[H]/[Pd]$  is lowest for  $Pd_{75}Au_{25}$  for the high loading times; the shift of the  $E_p$  of higher Au content samples is attributed to the fact that lower H amounts results in shorter times for the total H to desorb from the material. The observations regarding the  $E_p$  shift for low and high H amounts is also in accordance with recent work of Lukaszewski et al. [41]. Revisiting the discussion of the diffusivity of H in Pd-Au alloys that was considered before for very low H content (see section 3.3), diffusion of H is not the determining factor in the observed peak potential shift (Figure 2.8d) for the high H content. As Au% increases, the diffusivity of H decreases [31], so a peak shift to more anodic potentials is expected whereas the observed peak shift on Figure 2.8d is towards more cathodic potentials. Thus, when only small amounts of hydrogen are absorbed,  $E_p$  reflects the H-metal binding strength or the diffusivity of H and for higher H contents the time needed to remove all the H is determining  $E_p$ .

## 2.4. Conclusions

In this research we used a fast and quantitative electrochemical method to screen the hydrogen sorption (adsorption and/or absorption) and desorption behaviour. We showed that the method can be used to (i) determine the effect of phases present on the amount of hydrogen absorbed and the kinetics of absorption, (ii) quantify the amount of hydrogen desorbing (even for very small amounts) and (iii) identify the effect of alloying elements on hydrogen sorption/desorption behaviour and the binding strength of H to the surface or in the bulk.

The method was applied to Pd-based alloys. Analysis of the H-loading current for different alloys (Pd, Pd-Au and Pd-Mo-Cu) shows that the phases present, i.e.  $\alpha$ ,  $\alpha+\beta$  or  $\beta$ , influences the kinetics of H evolution and H uptake in the material. In particular, the hydrogen reduction kinetics is enhanced in the two-phase region. The amount of desorbing H, determined by the consecutive cyclic voltammetry scans, allowed to quantify the amounts of hydrogen even in the  $\alpha$ -phase when about 0.05 H atoms per metal atom are present. Significant differences in H-sorption/desorption behavior are observed depending on the kind and amount of alloying elements present. Au and Cu-Mo addition can reduce the total amount of H that can be absorbed (long loading times). The parameter determining the total hydrogen uptake for low H-contents is the kinetics of  $H^+$  reduction, whereas for long loading times the total amount of H in the material is determined by

thermodynamics. The peak potential ( $E_p$ ) of the CV scans may be an indication of how strong the hydrogen is interacting with the surface or the bulk for low loading times and of the amount of H in the bulk for high loading times.

## **Acknowledgements**

The authors gratefully acknowledge R. W. A. Hendrikx and N.M. van der Pers for helping with XRD related sample preparations and discussions. We would also like to thank Irimi Zacharaki for her experimental support. This work is financially supported by the Delft University of Technology and is part of a Materials innovation institute (M2i) research program with project number MC6.06283.

## References

1. Bortolotto, L. and R. Dittmeyer, Separation and Purification Technology, 2010. **73**(1): p. 51-58.
2. Dittmeyer, R., V. Hollein, and K. Daub, Journal of Molecular Catalysis a-Chemical, 2001. **173**(1-2): p. 135-184.
3. Sato, K., et al., Catalysis Today, 2010. **156**(3-4): p. 276-281.
4. Sheintuch, M. and R.M. Dessau, Chemical Engineering Science, 1996. **51**(4): p. 535-547.
5. Gallucci, F., et al., Industrial & Engineering Chemistry Research, 2006. **45**(9): p. 2994-3000.
6. Uemiya, S., Topics in Catalysis, 2004. **29**(1-2): p. 79-84.
7. Uemiya, S., et al., Applied Catalysis, 1991. **67**(2): p. 223-230.
8. Westerwaal, R.J., et al., International Journal of Hydrogen Energy, 2013. **38**(10): p. 4201-4212.
9. Nanu, D.E. and A.J. Bottger, Advanced Functional Materials, 2008. **18**(6): p. 898-906.
10. Amandusson, H., L.G. Ekedahl, and H. Dannetun, Applied Surface Science, 2000. **153**(4): p. 259-267.
11. Gao, H.Y., et al., Industrial & Engineering Chemistry Research, 2004. **43**(22): p. 6920-6930.
12. Li, A., W. Liang, and R. Hughes, Journal of Membrane Science, 2000. **165**(1): p. 135-141.
13. Zhao, Z.Y., et al., Sensors and Actuators B-Chemical, 2008. **129**(2): p. 726-733.
14. Piccolo, L., A. Piednoir, and J.C. Bertolini, Surface Science, 2005. **592**(1-3): p. 169-181.
15. Wang, K.W., S.R. Chung, and T.P. Perng, Journal of Alloys and Compounds, 2006. **417**(1-2): p. 60-62.
16. Roa, F., *Palladium-Copper and Palladium-Gold Alloy Composite Membranes for Hydrogen Separations*, in *Inorganic Membranes for Energy and Environmental Applications*, A.C. Bose, Editor. 2009, Springer Science+Business Media: New York, USA.
17. Hubert, T., et al., Sensors and Actuators B-Chemical, 2011. **157**(2): p. 329-352.
18. Bard, A.J. and L.R. Faulkner, *Electrochemical Methods Fundamentals and Applications*. 1980, New York: John Wiley & Sons.
19. Czerwinski, A. and R. Marassi, Journal of Electroanalytical Chemistry, 1992. **322**(1-2): p. 373-381.
20. Czerwinski, A., R. Marassi, and S. Zamponi, Journal of Electroanalytical Chemistry, 1991. **316**(1-2): p. 211-221.
21. Czerwinski, A., et al., Journal of Electroanalytical Chemistry, 1995. **386**(1-2): p. 207-211.
22. Lukaszewski, M. and A. Czerwinski, Electrochimica Acta, 2003. **48**(17): p. 2435-2445.
23. Lukaszewski, M. and A. Czerwinski, Journal of Solid State Electrochemistry, 2008. **12**(12): p. 1589-1598.
24. Lukaszewski, M., K. Hubkowska, and A. Czerwinski, Physical Chemistry Chemical Physics, 2010. **12**(43): p. 14567-14572.
25. Lukaszewski, M., et al., Journal of Solid State Electrochemistry, 2003. **7**(2): p. 69-76.
26. Pers, N.M.v.d., et al., Review of Scientific Instruments, 2013. **84**(4): p. 045102.
27. Pourbaix, M., *Atlas of electrochemical equilibria in aqueous solutions*. 1974: NACE International.
28. Lukaszewski, M., K. Hubkowska, and A. Czerwinski, Journal of Electroanalytical Chemistry, 2011. **651**(2): p. 131-142.
29. Hubkowska, K., et al., Journal of Electroanalytical Chemistry, 2013. **704**: p. 10-18.
30. Conrad, H., G. Ertl, and E.E. Latta, Surface Science, 1974. **41**(2): p. 435-446.
31. Perrot, P., *Gold-Hydrogen-Palladium*, Landolt-Bornstein. p. 258-265.
32. Sonwane, C.G., J. Wilcox, and Y.H. Ma, Journal of Physical Chemistry B, 2006. **110**(48): p. 24549-24558.
33. Sonwane, C.G., J. Wilcox, and Y.H. Ma, Journal of Chemical Physics, 2006. **125**(18).
34. Rousset, J.L., J.C. Bertolini, and P. Miegge, Physical Review B, 1996. **53**(8): p. 4947-4957.
35. Mittemeijer, E.J. and U. Welzel, eds. *Modern Diffraction Methods*. 2013, Wiley-VCH Verlag & Co. : Weinheim, Germany.
36. Tomanek, D., et al., Surface Science, 1982. **114**(1): p. 11-22.
37. Luo, S., D. Wang, and T.B. Flanagan, Journal of Physical Chemistry B, 2010. **114**(18): p. 6117-6125.
38. Nanu, D.E., et al., Acta Materialia, 2010. **58**(16): p. 5502-5510.

39. Wagner, F.E., et al., *Interaction of Hydrogen with Substitutional Solute Metals in the  $\beta$ -Phase of the Palladium-Hydrogen System*, in *Electronic Structure and Properties of Hydrogen in Metals*, P. Jena and C.B. Satterthwaite, Editors. 1983, Springer US. p. 581-588.
40. Macland, A. and T.B. Flanagan, *Journal of Physical Chemistry*, 1965. **69**(10): p. 3575-&.
41. Lukaszewski, M., et al., *Materials*, 2013. **6**(10): p. 4817-4835.

# CHAPTER 3



# CHAPTER 3: Investigation of H-desorption from Pd and Pd-alloys by Mass Spectrometry and the Role of Water Forming Reactions

---

*In this chapter, we present a combination of thermogravimetric analysis (TGA) with mass spectrometry (MS) to study H-desorption from Pd, Pd-Au and Pd-Cu-Mo alloys. Samples were electrochemically H-loaded in a 1 M KOH solution. In order to express the H-desorbed quantitatively, calibration of MS signals was performed for both H<sub>2</sub> and water related components in the chamber. The water related calibration was achieved by means of decomposition of (CuSO<sub>4</sub>.5H<sub>2</sub>O) and the calibration of H<sub>2</sub> by means of Ar gas with 50 ppm H<sub>2</sub>. The H amount measured by MS was in agreement with the ones obtained by XRD and/or TGA methods. The Pd-Au and Pd-Cu-Mo alloys absorbed less H than pure Pd under the same loading conditions. Formation of water was the preferred reaction upon H release from the unalloyed Pd sample, whereas H<sub>2</sub> production selectively occurred on Pd-Au and Pd-Cu-Mo surfaces.*

---

## 3.1. Introduction

The interaction of hydrogen with Pd and its alloys is of interest since Pd is a potentially important material for metallic membranes for H purification, H storage applications, catalysis and sensor applications [1-4]. Although Pd is known to be suitable in these applications, alloying Pd with other metals is a route to enhance the lifetime and properties. As reviewed by Paglieri et al. [5], alloys can be preferred instead of pure Pd because: (i) Pd has high and fluctuating costs (ii)  $\alpha$  to  $\beta$  phase transition and associated volume changes cause embrittlement thereby reducing lifetime (this can be altered by alloying), (iii) Pd-alloys have comparable or higher permeability than the pure Pd, and (iv) alloys usually have higher ability to withstand thermal cycling. In the field of catalysis, Pd-Au alloys can be preferred over Pd for direct synthesis of H<sub>2</sub>O<sub>2</sub> from H<sub>2</sub> and O<sub>2</sub>. Pd-Au alloys have been reported to enhance the efficiency and selectivity towards H<sub>2</sub>O<sub>2</sub> production reaction rather than the side reactions [6-9]. Furthermore, high sensitivity and selectivity in hydrogen sensors is an important subject [10], in particular when the performance of pure Pd or Pd-alloys becomes critical as under actual application environments of various composition [11].

H-desorption has been studied extensively with techniques such as thermal desorption spectroscopy (TDS) for Pd and its alloys [1, 2, 4, 12, 13]. This method enables to study the different H-traps and their activation energies.

In this work, we used a combined method of thermogravimetric analysis (TGA) and mass spectrometry (MS) in order to study the H-desorption properties of Pd, Pd-Au and Pd-Cu-Mo alloys. Combining H-desorption properties with H-sorption properties (see Chapter 2), H-interactions with different alloys are better understood. With this knowledge, it is possible to get one step closer to tailoring application specific alloys with high performance while optimizing costs. In this respect, we aimed at (i) comparing the amounts of H that desorbed out of the samples with the amounts that were calculated based on cyclic voltammetry (CV) experiments (Chapter 2) and X-ray diffraction technique, and (ii) examining the role of water forming reactions in the route of H-desorption from different Pd-alloys. Adsorption of reaction products on the surface and the gas atmosphere were investigated using Fourier transform infrared spectroscopy (FTIR) measurements.

### 3.2. Experimental procedure

The materials used were foils of Pd, Pd<sub>75</sub>Au<sub>25</sub> and Pd<sub>85</sub>Cu<sub>5</sub>Mo<sub>10</sub> (Chapter 2 [7]) of 50 μm thickness. The foils were cut in 2 x 1 cm<sup>2</sup> rectangles, and a hole with a diameter of 2 mm was made in order to hang the samples in the TGA equipment. The samples were hung with a silica pin into the TGA chamber.

The sequence of the experiments performed on the samples is summarized in Figure 3.1. Firstly, X-ray diffraction (XRD) scan and Fourier transform infrared spectroscopy (FTIR) tests were performed on the fresh samples. Such measurements were intended to serve as reference. Next, potentiostatic H-loading was performed, which was either followed by TGA/MS experiments, XRD or FTIR tests. The TGA/MS experiments were performed in two repetitive cycles, out of which the second one served as the reference.

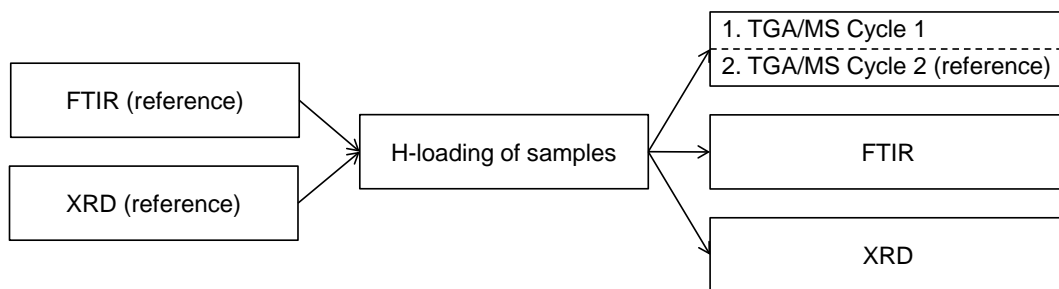


Figure 3.1. Sequence of experiments performed to investigate H-desorption behaviour of Pd-alloys.

The details of the electrochemical H-loading experiments were explained in detail in Chapter 2 [14]. After cleaning the surface, the specimens were electrochemically loaded using a saturated standard calomel electrode (SCE) as the reference electrode and Pt as the counter electrode. The electrolyte used was a 1 M KOH solution. The important parameters are summarized in Table 3.1.

Table 3.1. Summary of the electrochemical H-loading conditions [14].

Material	Solution	H-charging potential	H-charging time
Pd, Pd-alloys	1 M KOH	- 1.2 V vs. SCE	4 hours

The FTIR tests were performed with a Thermo-Nicolet Nexus FTIR apparatus equipped with a mercury-cadmium-telluride liquid-nitrogen-cooled detector and a nitrogen-purged measurement chamber.

X-ray powder diffraction (XRPD) patterns were recorded in a Bragg-Brentano geometry in a Bruker D8 Advance diffractometer equipped with a Vantec position sensitive detector and graphite monochromator [15]. Data collection was carried out at room temperature using monochromatic Co K $\alpha$  radiation ( $\lambda = 0.179026$  nm) in the  $2\theta$  region between  $40^\circ$  and  $140^\circ$ , step size  $0.04^\circ 2\theta$  and measuring time per step 2 s. The samples were placed on a Si {510} substrate and rotated during measurement.

Thermogravimetric Analysis (TGA) equipment utilized was a Setaram Setsys Evolution combined with an Omnistar quadrupole mass spectrometer by Pfeiffer Vacuum. The TGA/MS experiments were performed in two cycles as schematically depicted in Figure 3.2. H desorbs out of the sample during the first cycle.

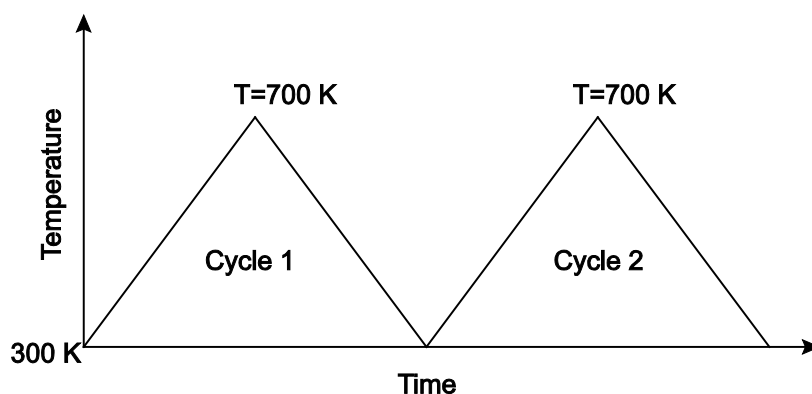


Figure 3.2. Schematics of the TGA/MS experiments: Cycle 1 is the actual measurement, whereas Cycle 2 is used as a reference. Temperature scan is from 300 K to 700 K.

Because all H is already desorbed after the first cycle, Cycle 2 serves as a reference measurement to estimate the background. The heating was performed from 300 K to 700 K with 5 K/min heating rate. The Multiple Ion Detection (MID) data acquisition method [16] was used for the mass spectrometer measurements. The MID method is used when the mass numbers to be monitored are known and the system only reports back these numbers. The mass-to-charge ratios ( $m/e$ ) tracked by the MID method and the corresponding ions are given in Table 3.2.

For the calibration of the water related signal, copper sulphate in the pentahydrate form ( $\text{CuSO}_4 \cdot 5\text{H}_2\text{O}$ ) obtained from Sigma Aldrich (ReagentPlus®,  $\geq 98.0\%$ ) was used. A temperature range of 300-573 K and a heating rate of 3 K/min were chosen to perform the calibration experiments of  $\text{H}_2\text{O}$ . Two heating cycles were performed similar to that in Figure 3.2 in order to confirm that  $\text{CuSO}_4 \cdot 5\text{H}_2\text{O}$  was fully decomposed. For the calibration of the  $\text{H}_2$  signal, a gas mixture of 50 ppm  $\text{H}_2$  in Ar (Lindegas Benelux B.V. Purity 99.9999%) was used. This content was selected because it is approximately equal to the H amount that is expected to desorb from the samples. For this purpose, the experiment first started with flowing 60 ml/min Ar gas in the chamber. The  $m/e=2$  signal pertaining to  $\text{H}_2^+$  was measured and used as the background. Then the gas composition was switched to the mixture of Ar and  $\text{H}_2$ ; Ar with 50 ppm  $\text{H}_2$  flowing with 60 ml/min was fed into the system. The pressure change in the  $m/e=2$  channel, taking into account the background, was then used to relate the MS  $\text{H}_2^+$  signal to the  $\text{H}_2$  amount.

### 3.3. Results and discussion

The mass-to-charge ratios ( $m/e$ ) to be tracked during the MS experiments were selected based on the gas atmosphere within the chamber during the measurements. A residual gas analysis (RGA) was performed while flowing 60 ml/min Ar gas in order to verify the chamber atmosphere. The result is given in Figure 3.3. The mass-to-charge ratios observed in this figure were also tracked during the experiments with Pd-alloys.

Because the  $m/e$  for different compounds could overlap (e.g.  $m/e=18$  contains contributions of  $\text{H}_2\text{O}^+$  and  $^{36}\text{Ar}^{++}$  isotope ions), it was aimed to make a suitable selection of which  $m/e$  to use for  $\text{H}_2$  and  $\text{H}_2\text{O}$  identification. Therefore, the effect of the isotopes and the cracking patterns of molecules/ions were considered. Additionally, the sensitivities for different components were taken into account. The complete analysis of the isotopes and the fragmentation probabilities on the mass spectrum is considered in Appendix A of this thesis. The  $m/e$  values of the main contributing components of Figure 3.3 are summarized in Table 3.2.

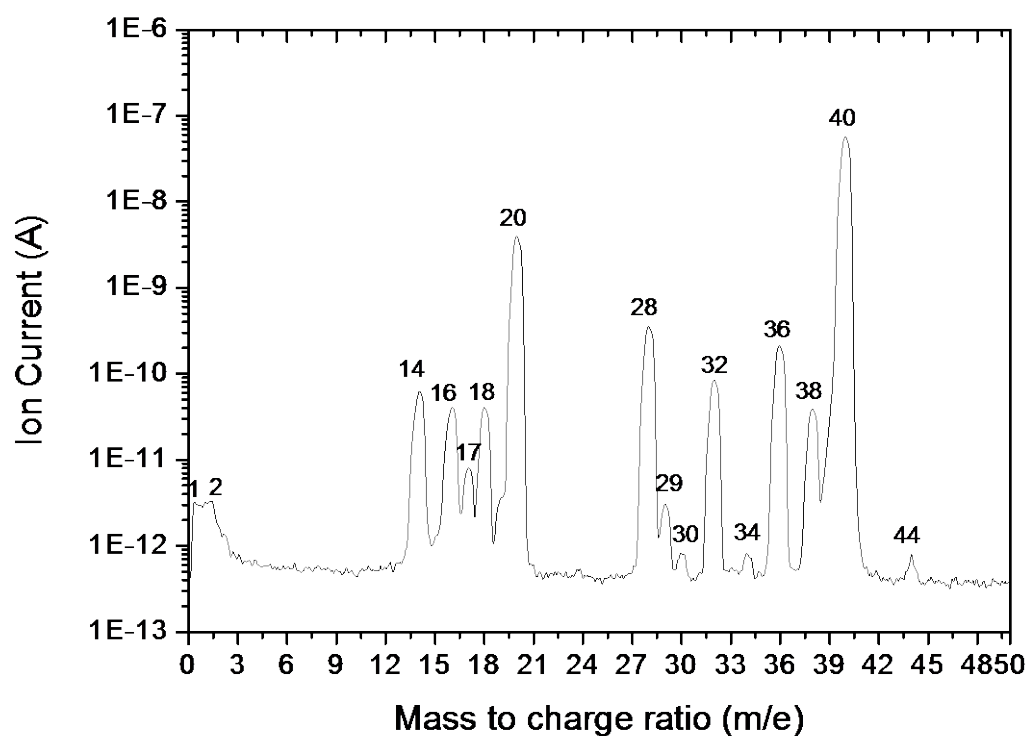


Figure 3.3. Residual gas analysis (RGA) result while flowing 60 ml/min Ar in the TGA chamber.

Table 3.2. The mass-to-charge ratio ( $m/e$ ) followed during the MS experiments and their corresponding main components. The terms in brackets indicate contributions due to isotopes.

Mass-to-charge ratio ( $m/e$ )	Corresponding component
1	$H^+$
2	$H_2^+$
14	$N^+$
16	$O^+$
17	$OH^+$ ( $O^+$ )
18	$H_2O^+$ , ( $Ar^{++}$ , $OH^+$ , $O^+$ )
20	$Ar^{++}$ , ( $H_2O^+$ , $OH^+$ )
28	$N_2^+$
29	( $N_2^+$ )
32	$O_2^+$
36	( $Ar^+$ )
38	( $Ar^+$ )
40	$Ar^+$

While Ar ( $m/e = 40$ ) is the major component in the chamber, it is seen that peaks related to  $N_2$  and  $O_2$  are also visible ( $m/e = 28$  and  $32$ , respectively), indicating the presence of air in the chamber. Air was not intentionally introduced to the chamber, but the observed level was considered in order-of-magnitude agreement with real application environments for these materials (e.g. sensors). Based on the analysis in Appendix A,  $m/e = 17$  was chosen for the water related analysis and  $m/e = 2$  as the main peak for hydrogen related analysis. As hydrogen desorbs out of the Pd-alloys, it is expected to form  $H_2$  gas in the chamber. Alternatively (or simultaneously), as H desorbs out, it could react to form water. Therefore,  $H_2$  and  $H_2O$  are expected to be the main products upon H desorption within the chamber. In order to quantify the desorbed hydrogen, calibration was performed for both  $H_2$  and water.

Copper (II) sulfate pentahydrate ( $CuSO_4 \cdot 5H_2O$ ) was used as a calibration compound for the water signal because it is known to decompose by losing two water molecules at 336 K, followed by two more at 382 K and the final water molecule at 473 K [17].

An example of the MS results is shown in Figure 3.4a, where the partial pressure  $OH^+$  ions at  $m/e = 17$  is shown.

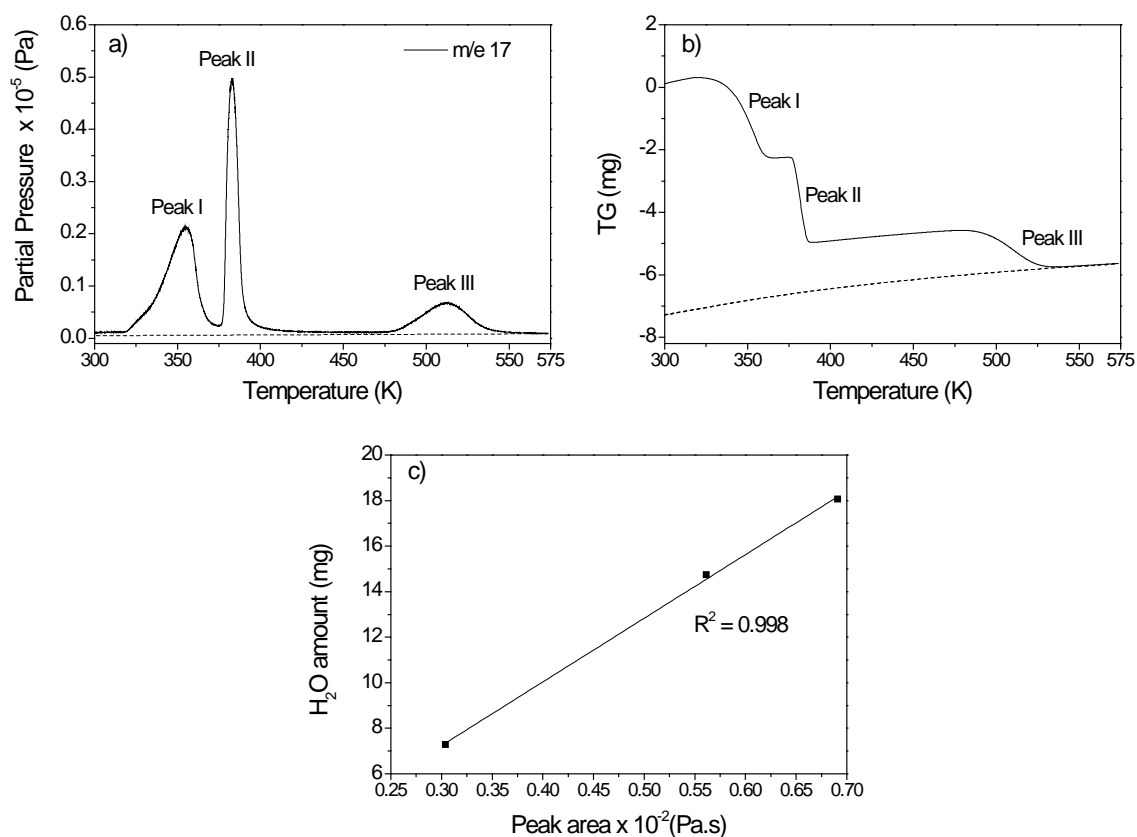


Figure 3.4. Calibration for water a) MS  $m/e=17$  for Copper (II) sulfate pentahydrate ( $CuSO_4 \cdot 5H_2O$ ), b) TG results of the same sample as in a), c) water amount – MS water peak area relationship.

The onset temperature of Peak I, Peak II and Peak III of the partial pressure-temperature graph in Figure 3.4a match well with the decomposition temperatures expected (336 K, 382 K and 473 K, respectively). These peaks also match well with the TGA results (Figure 3.4b) that show three stages of weight loss associated with the three peaks quoted. The dotted lines in Figure 3.4a and Figure 3.4b are the backgrounds as observed during cycle 2, which confirm that all water has desorbed. Combining information from MS (Figure 3.4a) and TGA (Figure 3.4b) the amount of desorbed  $\text{H}_2\text{O}$  was related to the MS peak areas. This calibration experiment was repeated three times, and a linear relation of the  $\text{H}_2\text{O}$  content and the area of the partial pressure-time data was obtained (Figure 3.4c). This relation was then used to calculate the amount of  $\text{H}_2\text{O}$  from the MS  $\text{H}_2\text{O}^+$  signals of all the MS measurements in the subsequent sections.

### 3.3.1. Water vs. $\text{H}_2$ formation

The MS results of pure Pd with respect to temperature are shown in Figure 3.5 after background subtraction was performed. The  $m/e$  ratios relevant to  $\text{H}_2$  and  $\text{H}_2\text{O}$  compounds are shown. From Figure 3.5 it is clear that some of the signals ( $\text{O}^+$  and  $\text{O}_2^+$ ) became lower than the signals measured as the background, whereas others increased ( $\text{H}_2^+$ ,  $\text{OH}^+$ ,  $\text{H}_2\text{O}^+$ ) with respect to the background.

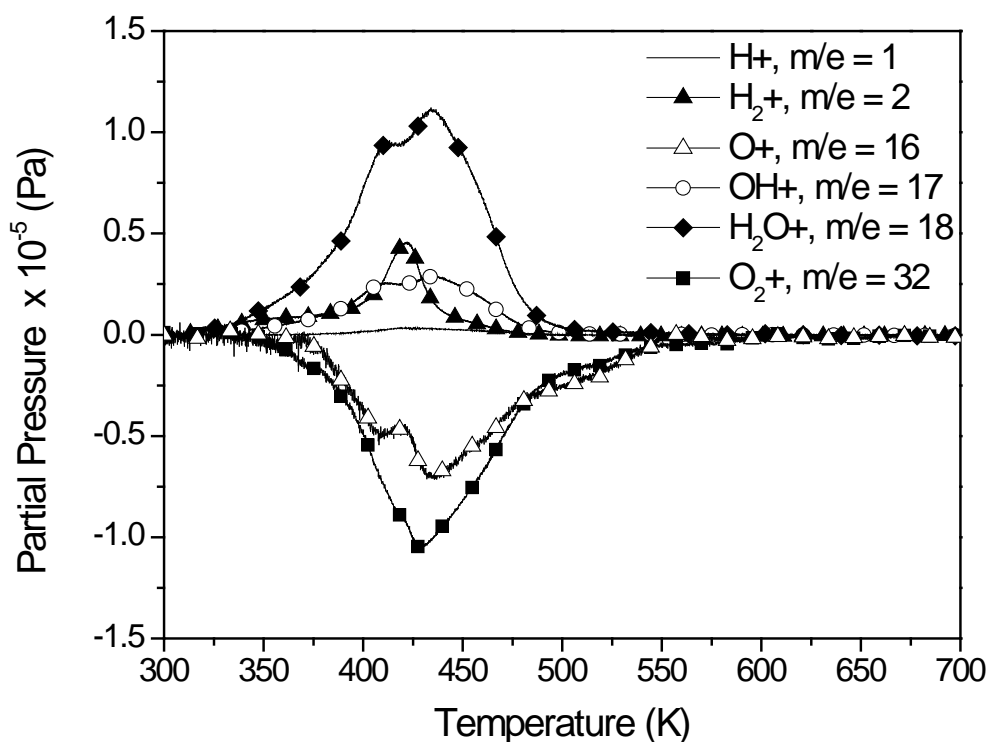
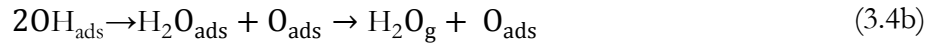


Figure 3.5. MS results of pure Pd for the  $m/e$  that are related to ions and fragments involved in  $\text{H}_2^+$  and  $\text{H}_2\text{O}^+$  forming reactions. The full curves are the actual data points, symbols are added for visual distinction of different signals.

As expected, a  $\text{H}_2^+$  peak (full triangle) is observed as one of the products, i.e. the result of hydrogen desorbing out of the sample thereby forming  $\text{H}_2$  according to eq. (3.1):



The  $\text{H}_2\text{O}^+$  ion is also one of the products and it shows two local maximums. According to Figure 3.5, the components that are being consumed are  $\text{O}^+$  and  $\text{O}_2^+$ . Similar to  $\text{H}_2\text{O}^+$ , the  $\text{O}^+$  signal shows two local minimums. The  $\text{H}_2\text{O}$  is assumed to be produced by one or more of the following reaction pathways [18, 19]:



According to the work of Nyberg et al. based on electron energy loss spectroscopy (EELS) [19], the water formation on Pd(100) material is suggested to occur via the reaction pathways of eq. (3.4a) and eq. (3.4b). All in all, looking into the trends of the consumed and produced components, it is concluded that part (most) of the hydrogen that desorbs out of the sample during heating reacts with the oxygen in the chamber, thus forming water.

The  $\text{H}_2^+$  MS signal of different alloys is compared in Figure 3.6a. The peaks are observed between 300-500 K. The  $\text{H}_2^+$  peak of the pure Pd shows two local maximums. This supports the conclusion that the two local maximums of the water related MS peaks ( $m/e=17$  and  $m/e=18$ ) are related to the  $\text{H}_2^+$  peak. The two  $\text{H}_2^+$  peaks are related to the two different phases that form in H-loaded Pd. The lower temperature maximum relates to the  $\alpha$ -phase and the higher temperature maximum relates to  $\beta$ -phase (see Chapter 2 [14] and Nanu et al. [20]). The  $\beta$ -phase is not expected in the  $\text{Pd}_{75}\text{Au}_{25}$  and  $\text{Pd}_{85}\text{Cu}_5\text{Mo}_{10}$  samples because these materials have a much lower critical temperature than pure Pd, and the  $\alpha$  to  $\beta$  transition does not take place.

The critical temperature is below room temperature for both  $\text{Pd}_{75}\text{Au}_{25}$  [20] and  $\text{Pd}_{85}\text{Cu}_5\text{Mo}_{10}$  [21]. Indeed only one desorption peak is observed in Figure 3.6a.

It is also clearly seen in Figure 3.6a that the highest amount of hydrogen is pertaining to pure Pd, and decreases on the order Pd<sub>75</sub>Au<sub>25</sub> and Pd<sub>85</sub>Cu<sub>5</sub>Mo<sub>10</sub>.

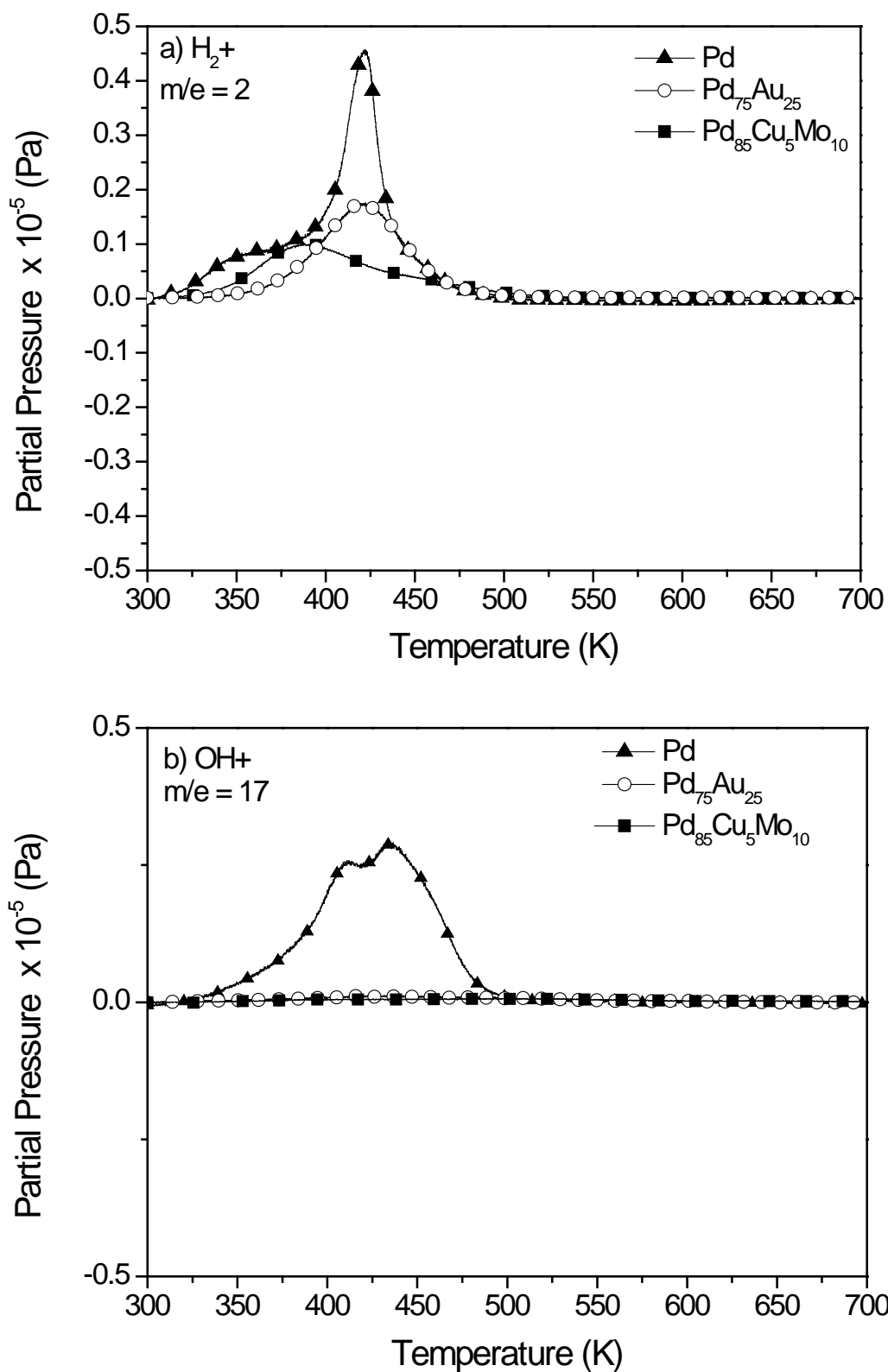


Figure 3.6. MS signals of Pd, Pd<sub>75</sub>Au<sub>25</sub> and Pd<sub>85</sub>Cu<sub>5</sub>Mo<sub>10</sub> a) H<sub>2</sub><sup>+</sup> signal (m/e=2), b) OH<sup>+</sup> signal (m/e =17).

Figure 3.6b clearly shows that the  $\text{OH}^+$  peak trends observed for  $\text{Pd}_{75}\text{Au}_{25}$  and  $\text{Pd}_{85}\text{Cu}_5\text{Mo}_{10}$  samples are noticeably different than those of the unalloyed Pd sample. For  $\text{Pd}_{75}\text{Au}_{25}$  and  $\text{Pd}_{85}\text{Cu}_5\text{Mo}_{10}$  samples,  $\text{OH}^+$  is such a small fraction of the  $\text{H}_2^+$  peak that it is not visible on Figure 3.6b. This difference between the MS results of Pd and its alloys could be due to catalytic activity differences between unalloyed Pd and the Pd-alloys. The result suggests that formation of  $\text{H}_2$  is preferred over the formation of  $\text{H}_2\text{O}$  for  $\text{Pd}_{85}\text{Cu}_5\text{Mo}_{10}$  and  $\text{Pd}_{75}\text{Au}_{25}$ . The higher electro-catalytic activity of Pd-Au alloy than pure Pd was observed for hydrogen evolution reaction in  $\text{H}_2\text{SO}_4$  solutions [9]. Also, density functional theory calculations support that alloying Pd with Au enhanced the selectivity toward  $\text{H}_2\text{O}_2$  formation rather than  $\text{H}_2\text{O}$  formation [6-8]. Our experimental results suggest that a higher selectivity for  $\text{H}_2$  formation rather than  $\text{H}_2\text{O}$  formation is valid for the case where the absorbed H desorbs from the sample upon heating. It is also suggested that addition of Cu and Mo alloying elements to Pd has a similar effect to selectively steer the reaction pathway towards  $\text{H}_2$  formation rather than  $\text{H}_2\text{O}$  formation. Thus, water-forming reactions seem to be preferred on the Pd surface over  $\text{H}_2$  evolution and the opposite holds on the  $\text{Pd}_{75}\text{Au}_{25}$  and  $\text{Pd}_{85}\text{Cu}_5\text{Mo}_{10}$  surfaces.

In order to further understand the difference between the existence of a water peak in the MS of Pd and the absence of such water peak for the  $\text{Pd}_{75}\text{Au}_{25}$  and  $\text{Pd}_{85}\text{Cu}_5\text{Mo}_{10}$  samples, FTIR measurements were performed; the results are given in Figure 3.7. A reference scan before H-loading is shown at the lowest position on each graph (open squares) for both Pd and  $\text{Pd}_{85}\text{Cu}_5\text{Mo}_{10}$  samples. The FTIR absorbance spectra are measured again directly after H-loading and also after 3 and 13 days. When the trends in Figure 3.7 are considered, it is seen that some peaks form below  $1750\text{ cm}^{-1}$  for both pure Pd and  $\text{Pd}_{85}\text{Cu}_5\text{Mo}_{10}$  samples after H-loading. The peak around  $1675\text{ cm}^{-1}$  reduces in intensity and disappears in time for both Pd and Pd-Cu-Mo alloy. This peak is possibly originating from the bending mode (scissoring) of a water molecule which is expected between  $1500$  to  $1650\text{ cm}^{-1}$ , depending on the amount of H-bonds formed [22, 23] and interaction strength of the water with the metal surface [18]. A higher frequency within the given range above (as our case with  $\sim 1675\text{ cm}^{-1}$ ) indicates a relatively weak interaction with the metal surface and that H-bonding between water molecules is extensive [18]. Furthermore, the source of this peak is the molecularly adsorbed water (and not its dissociation products) [18, 24].

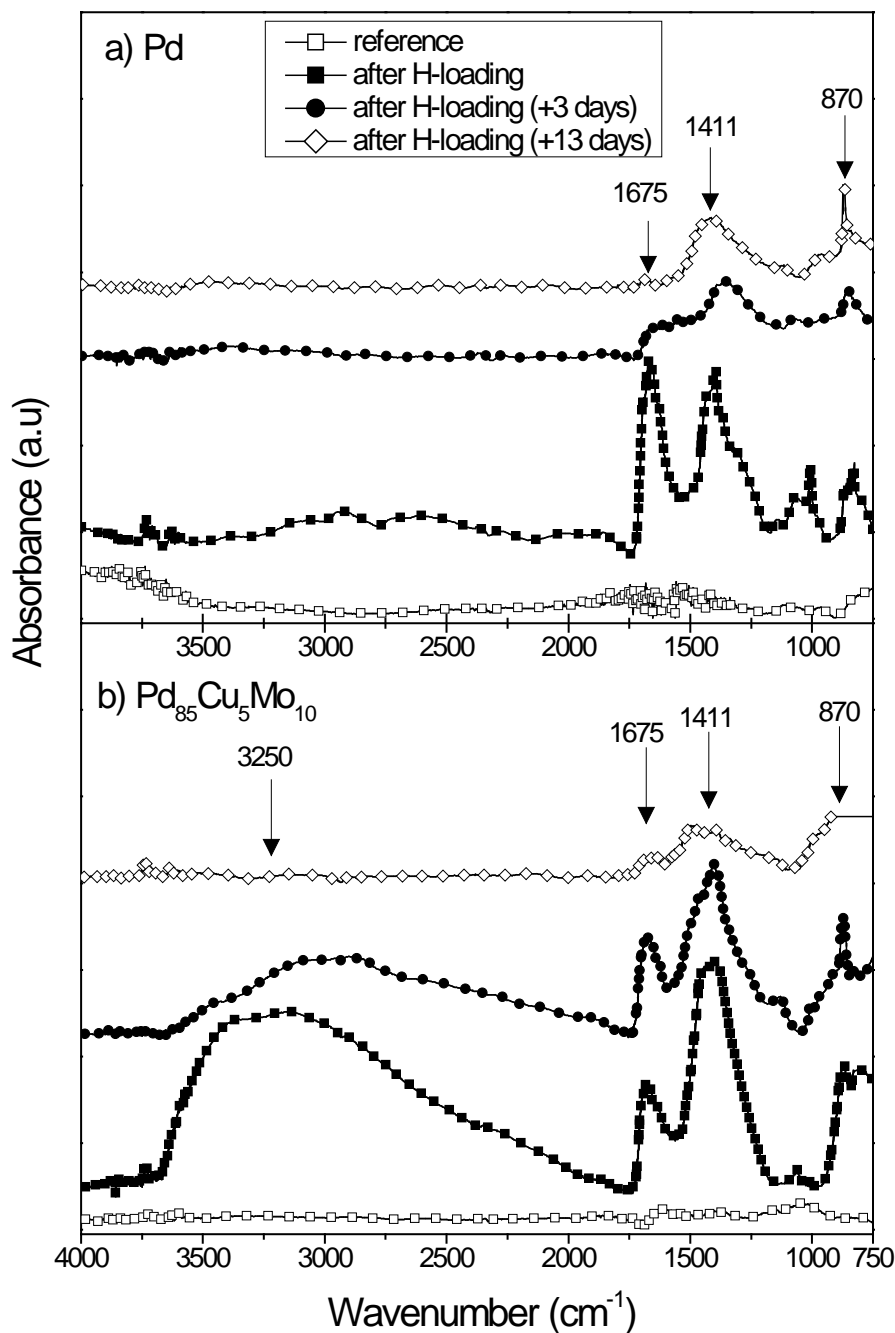


Figure 3.7. FTIR absorbance spectra of Pd and Pd<sub>85</sub>Cu<sub>5</sub>Mo<sub>10</sub> specimens. The arrows indicate the wave numbers of water related vibration modes at the surface.

When the Pd and Pd-Cu-Mo samples are compared for this peak right after H-loading, it is seen that the pure Pd has a higher intensity of the peak at 1675 cm<sup>-1</sup>. This could mean that all or most of the water is molecularly adsorbed on pure Pd, whereas for the Pd-Mo-Cu sample the water is adsorbed dissociatively. This complies with the dissociative adsorption of water on Mo [18].

When comparing the spectra from Pd and Pd-Cu-Mo alloys, the main differences are found above 1700 cm<sup>-1</sup>. The freshly H-loaded Pd-Cu-Mo samples show a very broad peak between

3600-2000  $\text{cm}^{-1}$ . It is known that extended water structures (H-bonded water molecules) typically show extremely broad bands [22]. Absorption from such extended water structures occurs from 3700  $\text{cm}^{-1}$  (associated with the “free” or uncoordinated OH stretch) down to 3000  $\text{cm}^{-1}$  (for strongly hydrogen bonded OH) [22]. In time, it is seen that this water related peak diminishes and completely disappears, which suggests that the water film has evaporated. This broad peak is difficult to identify whether it is due to the dissociated hydroxyl compound or due to the OH stretch mode of the molecularly adsorbed water because these modes overlap with each other [18, 24]. Since it is only observed for the Pd-Co-Mo, it is likely that this broad peak is due to the dissociated OH stretch mode which is expected for Pd  $\sim 3160 \text{ cm}^{-1}$  [18]. The difference between the FTIR spectra of Pd and Pd-Cu-Mo samples could also be related to the status of the surface upon removing the samples out of the electrolyte solution. It is known that H is bound stronger to the Mo than to Pd atoms and Cu atoms [25]. This could mean that the Pd-Cu-Mo sample has a higher amount of H on the surface upon removing the sample from the electrolyte. These H atoms can react with the oxygen in the air and form OH and  $\text{H}_2\text{O}$  components on the surface. This would imply a lower amount of OH and  $\text{H}_2\text{O}$  formed on the surface for Pd samples than Pd-Cu-Mo samples, hence the FTIR results in Figure 3.7. These findings could appear contradictory with what has been found with the MS results, where the pure Pd sample showed a water peak and the  $\text{Pd}_{85}\text{Cu}_5\text{Mo}_{10}$  did not. However, it should be noted that for the Pd sample the water peak in the MS data only is observed during desorption of H, i.e. after desorption water is formed. During the FTIR measurements, however, desorption of H is minimal and therefore formation of water has probably not started yet. Assuming a {111} orientation on the Pd surface and 1  $\text{H}_2\text{O}/\text{Pd}$  adsorption ratio on the surface [18], there are  $3.79 \times 10^{14}$  Pd sites available for  $\text{H}_2\text{O}$  adsorption. The expected MS peak area of such amounts of water at the MS is  $\sim 2$  ppm of the peak area observed in Figure 3.6b. Such a small expected peak area lies within the background and therefore not visible by means of MS. Finally, taking the MS and the FTIR results into consideration it is concluded that the source of the water related peak in the MS of the Pd sample (Figure 3.6b) cannot be the water adsorbed on the surface, but that it is produced as H-desorbs from the Pd sample by reacting with oxygen in the chamber.

### 3.3.2. Quantification of $\text{H}_2$

Quantification of the amount of hydrogen desorbing from the pure Pd sample is performed by taking both the MS water related  $m/e=17$  peak and the  $\text{H}_2^+$   $m/e=2$  peak into account.

Combining the amounts of  $\text{H}_2$  obtained from the  $\text{H}_2$  and  $\text{H}_2\text{O}$  related peaks, a total amount of  $0.77 \pm 0.07 \text{ mg H}_2$  is obtained. This corresponds to an atomic ratio of  $[\text{H}]/[\text{Pd}] = 0.72$ . 85% of

this total amount of hydrogen stems from the water contribution ( $m/e=17$ ) whereas the rest (15%) is detected as  $H_2$  ( $m/e=2$ ). This value is in good agreement with the TG results ( $[H]/[Pd]=0.75$ ) in Figure 3.8. The weight loss starts just above 300 K and ends around 500 K. This range of weight loss is also in good agreement with the MS results showing the  $H_2$  and  $H_2O$  related MS peaks between 300-500 K (Figure 3.6), this implies that the weight loss is due to H-desorption.

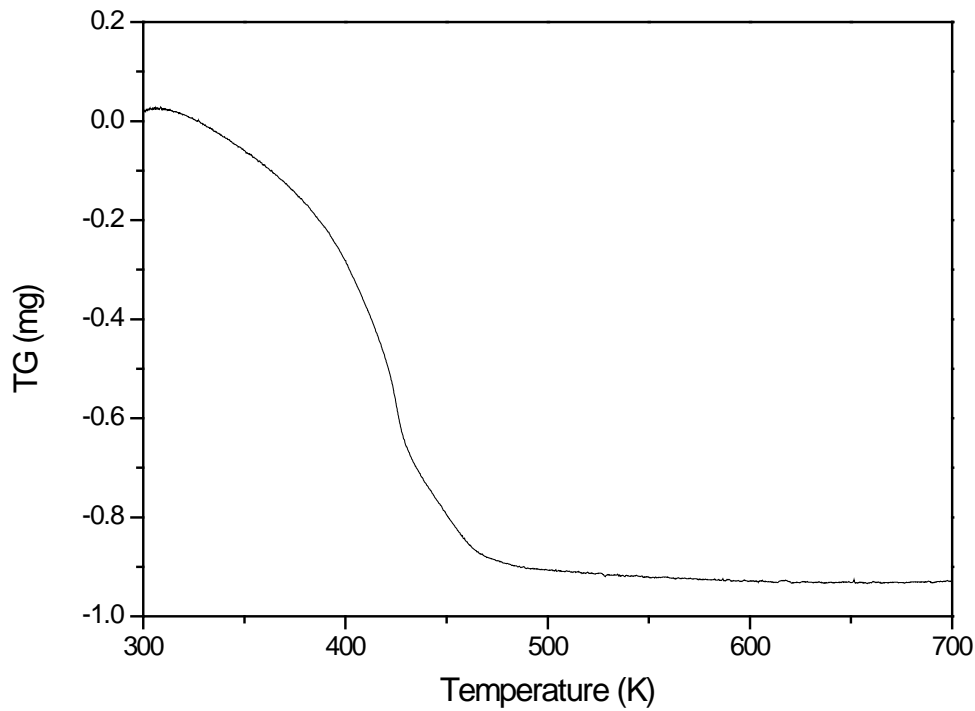


Figure 3.8. TGA results of Pd sample.

XRD was used to confirm the amount of hydrogen for the Pd sample. Upon loading with H, the XRD peaks of Pd shifted to lower  $2\theta$  indicating the phase change from  $\alpha$  to  $\beta$  (Figure 3.9). The lattice parameter change upon H-loading was calculated from the shift of the peaks. The H concentration in the  $\beta$  phase was calculated by the linear relationship between the lattice parameter change in Pd and hydrogen concentration according to eq. (3.5).

$$\frac{3}{a_0} \frac{\Delta a_0}{\Delta x} = 0.19 \pm 0.01 \quad [26] \quad (3.5)$$

Using the equation above, the hydrogen concentration was calculated as  $x = [H]/[Pd] = 0.6$ .

To summarize the hydrogen amount  $[H]/[Pd]$  quantified by different methods a comparison is presented in Figure 3.10.

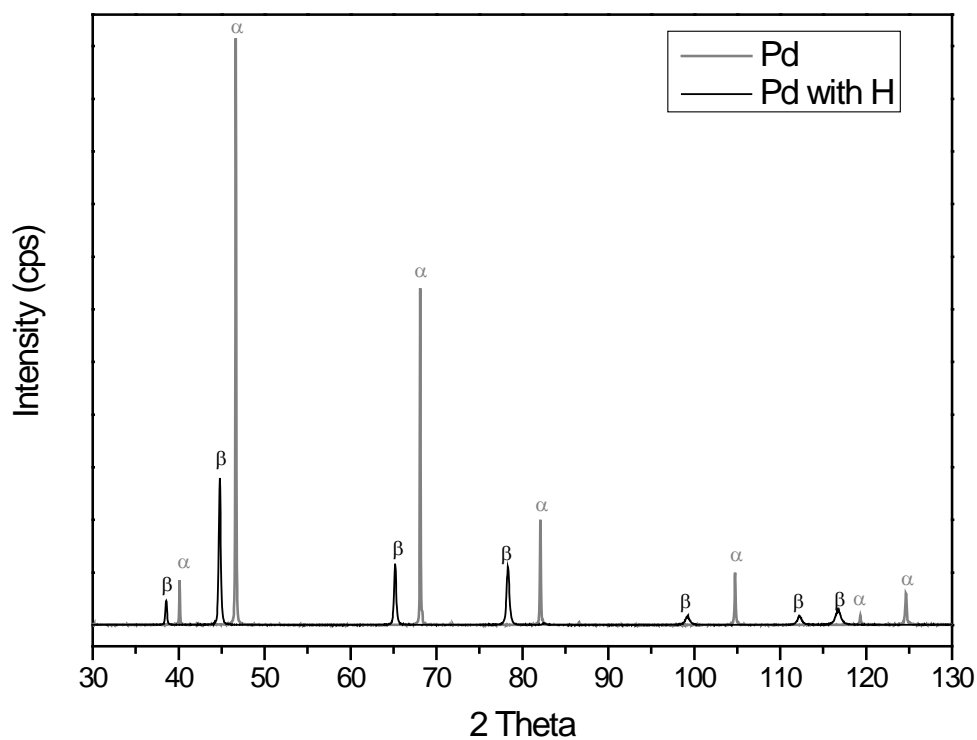


Figure 3.9. XRD scans of Pd sample before and after H-loading.

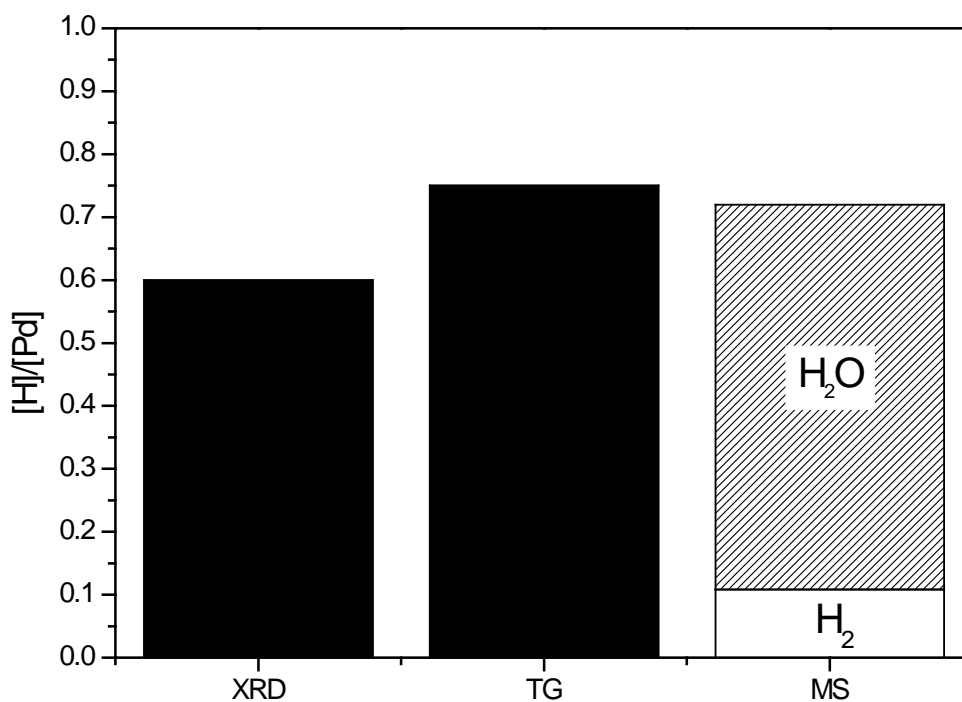


Figure 3.10. Comparison of  $[H]/[Pd]$  values with different methods: XRD, TG and MS. 85% in the total detected hydrogen in the MS has a water source and the remaining 15% is hydrogen.

The XRD method gives slightly lower values compared to the TG and the MS  $[H]/[Pd]$  values. This is probably because the sample used for XRD method was a different one than the TG and

MS measurements and therefore slight changes in experimental H-loading conditions can be expected.

For Pd<sub>75</sub>Au<sub>25</sub> [H]/[M] was calculated as 0.21 and for Pd<sub>85</sub>Cu<sub>5</sub>Mo<sub>10</sub> it was calculated as 0.009. This is in good agreement with results shown in Chapter 2 [14].

### 3.4. Conclusions

It was shown that for Pd sample, during H-desorption, most of the hydrogen that was absorbed by the sample reacts with oxygen in the chamber of the TGA equipment and forms water. Hydrogen desorbed from the Pd-Au and Pd-Cu-Mo samples preferably forms H<sub>2</sub> and not water. Therefore, for applications where H<sub>2</sub> production is preferred to take place rather than H<sub>2</sub>O formation, Pd-Cu-Mo and Pd-Au alloys are beneficial. Pd-Cu-Mo can be also used for H<sub>2</sub>O<sub>2</sub> synthesis reaction by inhibiting formation of H<sub>2</sub>O similar to Pd-Au.

By taking the suitable m/e peaks and performing the relevant calibration measurements, the H<sub>2</sub> content was confidently determined. This was achieved by considering both the hydrogen that reacts to form water and the hydrogen that is detected as H<sub>2</sub><sup>+</sup>. Combining the amounts of H<sub>2</sub> obtained from the H<sub>2</sub> and H<sub>2</sub>O peaks, the atomic ratio of [H]/[Pd] is in good agreement with the values for TG and XRD. [H]/[M] found for Pd, Pd<sub>75</sub>Au<sub>25</sub> and Pd<sub>85</sub>Cu<sub>5</sub>Mo<sub>10</sub> were respectively about 0.5, 0.2 and 0.01 under the same applied loading conditions

The FTIR results suggested that after H-loading of the samples in the electrolytic solution, adsorbed water is readily available on the surfaces of both Pd and Pd-Cu-Mo samples. The differences of the FTIR spectra showed that for Pd most of the water is molecularly adsorbed on the surface whereas for Pd-Cu-Mo it is dissociatively adsorbed as OH. It is concluded that the source of the water related peak in the MS of the Pd sample cannot be the water adsorbed on the surface, but that it is produced as H-desorbs from the Pd sample.

### Acknowledgements

The authors gratefully acknowledge J.C. Brouwer for supporting with TGA/MS related experiments and discussions. We would also like to thank R. W. A. Hendriks and N.M. van der Pers for helping with XRD related sample preparations and discussions. This work is financially supported by the Delft University of Technology and is part of the Materials innovation institute (M2i) research program with project number MC6.06283.

## References

1. Behm, R.J., et al., *Journal of Chemical Physics*, 1983. **78**(12): p. 7486-7490.
2. Cabrera, A.L., E. Morales, and J.N. Armor, *Journal of Materials Research*, 1995. **10**(3): p. 779-785.
3. Mendes, D., et al., *Asia-Pacific Journal of Chemical Engineering*, 2010. **5**(1): p. 111-137.
4. Pundt, A. and R. Kirchheim, *Annual Review of Materials Research*, 2006. **36**: p. 555-608.
5. Paglieri, S.N. and J.D. Way, *Separation and Purification Methods*, 2002. **31**(1): p. 1-169.
6. Li, J., et al., *Journal of Physical Chemistry C*, 2011. **115**(15): p. 7392-7398.
7. Staykov, A., et al., *Journal of Physical Chemistry C*, 2008. **112**(49): p. 19501-19505.
8. Ham, H.C., et al., *Journal of Physical Chemistry C*, 2009. **113**(30): p. 12943-12945.
9. Pluntke, Y., L.A. Kibler, and D.M. Kolb, *Physical Chemistry Chemical Physics*, 2008. **10**(25): p. 3684-3688.
10. Hubert, T., et al., *Sensors and Actuators B-Chemical*, 2011. **157**(2): p. 329-352.
11. Zhao, Z.Y., et al., *Sensors and Actuators B-Chemical*, 2008. **129**(2): p. 726-733.
12. Konvalinka, J.A. and J.J.F. Scholten, *Journal of Catalysis*, 1977. **48**(1-3): p. 374-385.
13. Cabrera, A.L., et al., *Applied Physics Letters*, 1995. **66**(10): p. 1216-1218.
14. Uluc, A.V., et al., *Journal of Electroanalytical Chemistry*, 2014. **734**: p. 53-60.
15. Pers, N.M.v.d., et al., *Review of Scientific Instruments*, 2013. **84**(4): p. 045102.
16. Vacuum, P. *Mass Spectrometer*. 2005 1 March 2015]; Available from: <http://www.istcgroup.com/pdf/Mass%20Spectrometer%20Catalog%202005%20-%202007.pdf>.
17. Holleman, A.F. and E. Wiberg, *Holleman-Wiberg's Inorganic Chemistry*. 2001, Berlin: Walter de Gruyter GmbH & Co.
18. Thiel, P.A. and T.E. Madey, *Surface Science Reports*, 1987. **7**(6-8): p. 211-385.
19. Nyberg, C. and C.G. Tengstal, *Journal of Chemical Physics*, 1984. **80**(7): p. 3463-3488.
20. Nanu, D.E., et al., *Acta Materialia*, 2008. **56**(20): p. 6132-6140.
21. Nanu, D.E. and A.J. Bottger, *Advanced Functional Materials*, 2008. **18**(6): p. 898-906.
22. Hodgson, A. and S. Haq, *Surface Science Reports*, 2009. **64**(9): p. 381-451.
23. Jacox, M.E. *Vibrational and Electronic Energy Levels of Polyatomic Transient Molecules*. NIST Chemistry WebBook, NIST Standard Reference Database Number 69 January 4, 2015; Available from: <http://webbook.nist.gov>.
24. Henderson, M.A., *Surface Science Reports*, 2002. **46**(1-8): p. 1-308.
25. Frese, K.W., *Surface Science*, 1987. **182**(1-2): p. 85-97.
26. Eastman, J.A., L.J. Thompson, and B.J. Kestel, *Physical Review B*, 1993. **48**(1): p. 84-92.

# CHAPTER 4



# CHAPTER 4: The Role of Heat Treatment and Alloying Elements on Hydrogen Uptake in Aermet 100 Ultrahigh-Strength Steel\*

---

*In this chapter we present a fast and semi-quantitative electrochemical method – based on cyclic voltammetry (CV) – to easily screen the H uptake of materials. We used Aermet 100, an ultrahigh-strength steel, in its as-quenched (martensitic) state and an aged state to investigate the H-desorption properties of different microstructures. The CV-based method clearly shows the influence of the alloying elements, the microstructure and the effect of hydrogen recombination poisons on the H uptake. The experiments indicate that a significant part of the uptake of hydrogen is due to (i) the presence of Ni as an alloying element and (ii) the presence of austenite that forms during the heat treatment.*

---

## 4.1. Introduction

Aermet 100 ultrahigh-strength martensitic steel was developed for aerospace applications in order to replace its predecessors that suffered from stress corrosion cracking or low toughness [1-5]. The alloy is used in landing gears, jet engine shafts and structural components. Aermet 100 combines high strength, high hardness and fracture toughness with good ductility [1]. High-strength steels in general are prone to degradation by hydrogen (H), thereby losing their excellent mechanical properties [2, 3, 5]. The presence of atomic hydrogen near a crack tip is recognized to cause crack propagation at stresses far below the critical stress in a hydrogen free condition [6]. High strength steel's susceptibility to hydrogen degradation therefore is largely determined by the hydrogen diffusivity and, the density and type of hydrogen traps. The microstructure of Aermet 100 is complex and contains a large number of traps: dislocations, coherent and incoherent metal carbides  $M_2C$  (where M is Mo, Cr, Fe), alloying elements in solid solution (mainly Ni and Co), retained or reverted austenite and martensite lath boundaries [3, 4]. Reversible traps (low H binding energy) are possible sources for diffusible (free moving) H that may cause embrittlement. The presence of irreversible traps (high H binding energy) in general does not enhance H-related

---

\* This chapter is based on:

Uluc, A. V., Tichelaar, F. D., Terryn, H., & Bottger, A. J. (2015). The role of heat treatment and alloying elements on hydrogen uptake in Aermet 100 ultrahigh-strength steel. *Journal of Electroanalytical Chemistry*, 739, 130-136.

failure mechanisms [3] unless high temperatures or high stresses are applied. The large amount of reversible and irreversible traps in Aermet 100 allows a high hydrogen uptake.

To enhance the resistance of Aermet 100 to H degradation, research has been focused on effects of the microstructure on strengthening mechanisms in relation with heat treatments [7-9] and hydrogen embrittlement. The type of traps and their binding strength of H have been investigated by means of Thermal Desorption Spectroscopy [4, 10, 11]. This resulted into a qualification of trap types: Reversible traps are dislocations, coherent  $M_2C$  precipitates, alloying atoms in solid solution, and austenite grain boundaries; irreversible traps are interfaces of incoherent carbides, martensite lath boundaries and prior austenite grain boundaries [11].

Electrochemical measurements have been widely used in determination of the diffusion constants of steels and other metals through permeation tests which was first introduced by Devanathan [12], including Aermet 100 [3, 13-15]. Recently Evers et al. [16] published a review of current techniques and introduced the Kelvin probe approach to detect very small amounts of hydrogen. In the current work, however, a different electrochemical approach is looked into in order to gain different information related to hydrogen in steels, such as the effect of alloying elements on hydrogen uptake. In general, cyclic voltammetry is a long established method in the following two areas. The first is the detection of small amounts of absorbed and adsorbed hydrogen in metals, mainly Pd and its alloys [17-24]. Secondly, CV has also been used to a large extent to study the oxidation/passivation and corrosion behavior of pure metals (amongst others Fe, Ni and Co) and several steels, but not yet Aermet 100 [25-35]. Although CV has been used extensively in these areas, to our knowledge, the hydrogen uptake properties of steels has not yet been looked into by means of CV. The focus on uptake properties of steels could be seen as an overlapping region between the above mentioned areas, as depicted in Figure 4.1.

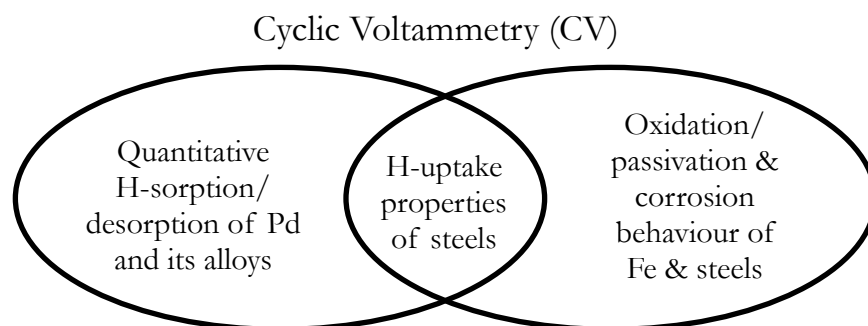


Figure 4.1. Different areas that cyclic voltammetry (CV) method is commonly used in.

It is the primary objective of present research to confirm that CV can be used as a fast and easy method to relate the diffusible hydrogen to microstructural features such as different phases and

alloying elements in steels. Since this method has not been used frequently for H-detection purposes in steels, it is the aim of this work to gain more insight into the hydrogen related regions of a cyclic voltammogram in a steel and unambiguously assign the peaks to chemical reactions. By comparing the cyclic voltammograms of different heat treated samples, one can get an indication if a steel contains diffusible hydrogen, and therefore may be prone to hydrogen embrittlement or not.

## 4.2. Experimental procedure

### 4.2.1. Methods

#### *Electrochemical set-up*

Cylindrical samples of  $\varnothing 20$  mm x 2 mm were first ground on one side (front side) up to #2400 grinding paper and then polished up to 1  $\mu\text{m}$ . A steel wire was attached to the sample on the back-side by spot welding. Both the back-side of the sample and the wire were painted with a lacquer resistant to highly basic solutions so that only one surface was exposed to the solution. The electrolyte was 1 M KOH (Sigma Aldrich, purity  $\geq 85\%$ ) solution. In some experiments, 4 g/l thiourea (Sigma Aldrich, grade puriss. p.a., Reag. Ph. Eur.,  $\geq 99\%$ ) was added to the solution as a recombination poison. A basic solution was selected since a high pH solution enables covering a wide potential region without corrosion dominantly taking place. For the cyclic voltammetry and H-charging experiments, a Potentiostat Autolab PGSTAT 12 was utilized with a saturated standard calomel electrode (SCE) as the reference electrode and platinum as the counter electrode. During the cyclic voltammetry experiments, the potential was swept between -1.3 V to 0.2 V starting at -1.3 V with a scan rate of 0.01 V/s. The H-charging potential was selected as -1.3 V to ensure hydrogen evolution on the working electrode. Charging times were varied from 1h to 72h. The sequence of the experiments was described in our previous work [24] but in summary was as follows: (1) two repeated cycles of CV, the first of these is regarded as a cleaning step of the surface and the second is the reference scan (2) consequent potentiostatic hydrogen charging at -1.3 V and (3) two repeated cycles of CV which are used to analyze the H-desorption behavior. The sample was not removed from the solution in between the steps mentioned. The temperature was fixed at 300 K during the experiments. All potentials are referred to SCE in this paper. When referring to literature, the potentials are also converted to SCE for ease of comparison.

### *Phase identification and microstructural analysis*

Phase identification was performed by means of X-ray diffraction. X-ray powder diffraction (XRPD) patterns were recorded in a Bragg-Brentano geometry with a Bruker D8 Advance diffractometer equipped with a Vantec position sensitive detector and a cone-shaped graphite monochromator [36]. Data collection was carried out at room temperature using Co K $\alpha$  radiation ( $\lambda = 0.179026$  nm) in the  $2\theta$  region between  $30^\circ$  and  $130^\circ$ , a step size of  $0.034^\circ 2\theta$ , and a measuring time per step of 2 s. The samples were placed on a Si (510) substrate and rotated during measurement. Data evaluation was done with the Bruker program EVA.

The Transmission Electron Microscope (TEM) utilized was a Monochromated Tecnai F20ST/STEM (FEI Electron Microscopes) with an Energy Dispersive Spectroscopy (EDS) detector for elemental composition analysis. Sample preparation was as follows: The  $\varnothing 20$  mm x 2 mm discs were first thinned by spark erosion and then the thickness was further reduced to  $\sim 20$   $\mu\text{m}$  by mechanical polishing. Next, 2.3 mm discs were punched and thinned by electrochemical polishing using 15% perchloric acid in methanol at 243 K. The final thinning step was done by Ar-ion milling.

Thermo-Calc (Version 5.0.4.75 with TCFE database version 6.2) was used to determine the composition and amounts of the thermodynamic stable phases expected in the as-quenched and aged condition. The results were compared with experiments (XRD, TEM/EDS).

### **4.2.2. Materials**

The chemical composition of the Aermet 100 used in this study is listed in Table 4.1. The compositions were obtained from the supplier AmEuro Metals B.V. The material was obtained in the form of rods with a diameter of 20 mm; 2 mm thick discs were cut from these rods.

Table 4.1. Composition of as-received Aermet 100 steel (balance Fe).

	<b>C</b>	<b>Cr</b>	<b>Ni</b>	<b>Co</b>	<b>Mn</b>	<b>Mo</b>	<b>Si</b>	<b>Al</b>	<b>S+P</b>
<b>wt. %</b>	0.23	3.00	11.14	13.44	0.01	1.18	0.01	0.003	0.003
<b>at. %</b>	1.08	3.25	10.63	12.83	0.010	0.69	0.02	0.006	0.005

The material was received in the as-quenched state after austenitization at 1116 K for 1 hour. After quenching, the materials were cryogenically chilled. The experiments were performed on the material in two states of heat treatment: (1) as-quenched (i.e. as-received) and (2) aged at 835 K for 69 hours in a salt bath (further in this paper this state will be named as “aged”). The “aged” condition, which is treated at a higher temperature than the peak-aged condition (see for instance

in literature [7]), was deliberately chosen in order to obtain a relatively high amount of austenite. These two heat treatments offer an opportunity for comparison, as there is an essential difference of the microstructures mainly in terms of the amount of austenite, but also the amount and coherency of the carbide precipitates.

### 4.3. Results and discussion

The CV results of before and after H-charging Aermet 100 samples for 1 hour in KOH solutions containing thiourea are given in Figure 4.2. During the CV experiments, the potential was swept starting from -1.3 V to ensure that the oxidation of adsorbed/absorbed hydrogen was the first occurring reaction so that the result was not affected by other surface reactions. After two consecutive CV scans, cathodic hydrogen charging was performed at -1.3 V, followed by two CV scans.

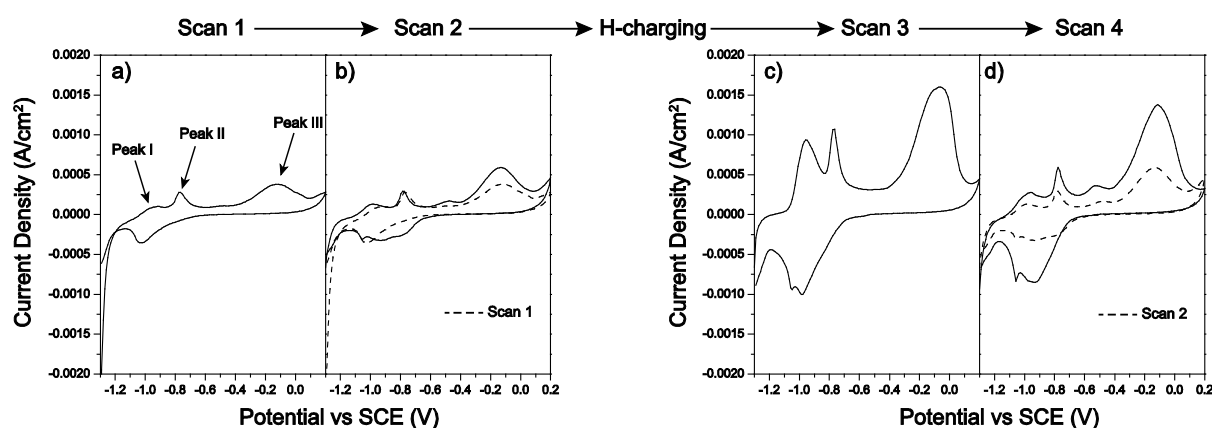


Figure 4.2. All four CV scans performed on an as-quenched Aermet 100 sample in 1 M KOH solution with thiourea and with a scan rate of 0.01 V/s. a) The first scan, regarded as a cleaning step b) second scan, then the H-charging for 4 hours (not shown), c) the third scan which is made after H-charging and d) a fourth scan.

In the anodic part of all four scans, three prominent peaks were observed as shown by the arrows in Figure 4.2a. The areas of these peaks increase strongly after H-charging (Figure 4.2). Although the peaks denoted Peak I and Peak II in the CV results in Figure 4.2 were observed before in several electrochemical studies on iron and steel samples [25, 28, 30, 33], the assignment of Peak I and Peak II to specific reactions differ from one study to another. Geana et al. [28], for example, assigned Peak I as the oxidation of adsorbed and absorbed hydrogen. However, in a rather recent paper Veleva et al. [32] state that Peak I is an indication of the transition from an active dissolution of the steel to passivation. Guzman et al. [29] comment that the first product forming in the potential region of Peaks I and II is  $\text{Fe}(\text{OH})_2$  and further discuss the formation of  $\text{FeOOH}$  at more anodic potentials. All in all, the assignment of the peaks around the potentials -1.1 V to -0.75 V is not very easy as both the hydroxidation of iron as well as oxidation of

hydrogen are thermodynamically possible in strongly basic solutions ( $\text{pH} \sim 13.5$ ) according to Pourbaix diagram [37]. This complication in assigning peaks to certain reactions is the reason why a separate discussion of origins of peaks is presented in the consecutive sections.

### 4.3.1. Hydrogenation vs. hydroxidation of Fe (Peak I vs. Peak II)

In Figure 4.3 (a-d), the effect of H-charging on the CV of as-quenched and aged specimens for various charging times is shown. The figure demonstrates the large differences between as-quenched and aged Aermet 100 samples when loaded in a KOH solution containing thiourea.

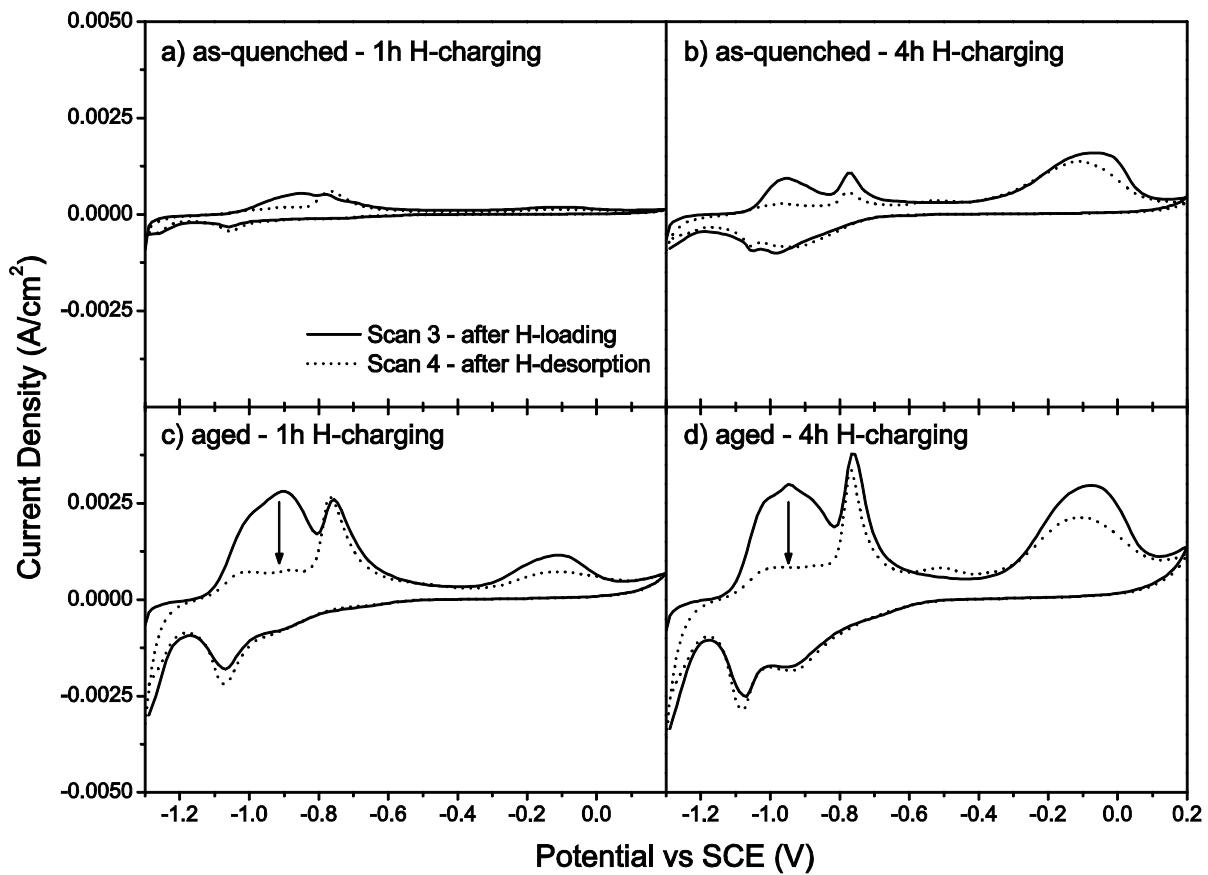


Figure 4.3. The CV results of scan 3 and scan 4 (cf. Figure 4.2) of as-quenched and aged Aermet 100 after H-charging for various durations in KOH solution with thiourea. The scan rate was 0.01 V/s. a) As-quenched, 1h charging; b) As-quenched, 4h charging; c) Aged, 1h charging; d) Aged, 4h charging.

The latter is a recombination poison which is known to increase the efficiency of H-charging by promoting H-absorption [38]. In particular, the differences between the as-quenched and aged samples are visible in Peak I and III. We relate these peaks to hydrogen absorption because their behavior strongly correlates with the H-charging time applied. When the charging time increases, an increase in the peak areas of Peak I, Peak II and III is observed in the scans made directly after the H-charging (scan 3). In the following CV scan (scan 4), however, Peak I (and III) are strongly reduced whereas Peak II does not change. The strong reduction of the area of peaks I

and III in scan 4 is assigned to the fact that hydrogen that has been absorbed during the charging is desorbed during scan 3. Note that during the reverse scan of scan 3 and the start of scan 4 hydrogen evolution takes place at potentials smaller than about -0.9 V which leads to some H absorption too. Therefore, desorption peaks (I and III) appear also in scan 4. Based on these observations, Peak I is suggested to be due to the oxidation of adsorbed/absorbed hydrogen. This is consistent with the conclusions of Geana et al [28]. Accordingly, the decrease of the peak area of Peak I from scan 3 to scan 4 (see arrows in Figure 4.3c and Figure 4.3d) is attributed to desorption of hydrogen from the sample.

The aged samples (Figure 4.3c and Figure 4.3d) show a higher Peak I area than the as-quenched samples (Figure 4.3a and Figure 4.3b). This difference is probably a consequence of the different phases present in the different samples. As seen in Table 4.2, the aged sample contains ~19 vol. % austenite determined from the X-ray diffraction patterns by the so-called direct comparison method [39], which is consistent with our Thermo-Calc calculation (21.5 vol.%) as well as the TEM results found in the literature [7, 9]. The higher amount of austenite in the aged samples could be responsible for the higher Peak I area of the aged sample than as-quenched since the H-solubility in the FCC lattice is known to be higher than the BCC lattice [40]. Although there is an obvious change in the voltammograms after H charging the X-ray diffraction patterns did not show any changes neither in peak positions, intensities nor in peak widths after charging.

Table 4.2. Phases present in the as-quenched and aged materials. Martensite is the main phase in the as-quenched material whereas in the aged sample it is referred as ferrite. The precipitates were predicted by Thermo-Calc and also reported in literature [7].

	<b>Austenite vol. %</b>	<b>Precipitates ([7] and Thermo-Calc)</b>	<b>Martensite or Ferrite vol.%</b>
<b>as-quenched</b>	< 2	MC, M <sub>23</sub> C <sub>6</sub> , M <sub>7</sub> C <sub>3</sub>	Balance
<b>aged (835 K, 69h)</b>	18.6 ± 2.1	M <sub>23</sub> C <sub>6</sub> , M <sub>6</sub> C, M <sub>2</sub> C	Balance

Another reason for a higher Peak I area could be related to other differences in the microstructure due to the heat treatment. The aged samples offer a more complex microstructure with an increased amount of precipitates. These precipitates could then act as traps for H resulting in an increase of the total H absorbed by the system.

The major difference between experiments with thiourea vs. without thiourea in the solution is in the area of Peak I. In experiments where thiourea is used, the peak area is about a factor of 10 higher than those without thiourea as summarized in Figure 4.4.

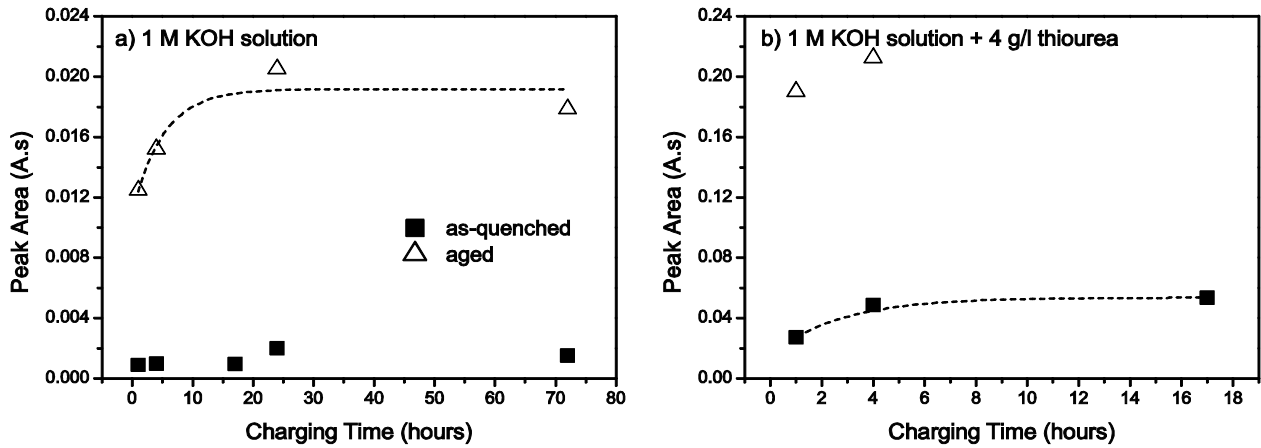


Figure 4.4. Areas of Peak I of as-quenched and aged Aermet 100 after charging in a 1M KOH solution a) without thiourea; b) with thiourea.

When the potentiostatic charging curve areas are taken into account, it is seen that the current produced during charging of the aged samples is already higher than that of the as-quenched samples (see Figure 4.5a). This could indicate that hydrogen dissociation and/or diffusion on the surface or towards the bulk for the aged samples is higher than that of the as-quenched samples. Additionally, Figure 4.5b shows the efficiency of the H-charging. Here, the efficiency is defined as:

$$\frac{\text{Peak I area (H in Fe)}}{\text{H - charging curve area}}$$

As this ratio gets closer to 1, the hydrogen produced on the surface is more efficiently absorbed by the sample. For the as-quenched sample, the efficiency is rather low for all charging times. However, regarding the aged sample, for 1 h charging, more than half of the produced hydrogen is absorbed (and then desorbed) by the system. The efficiency gradually decreases upon longer charging times and reaches the level of as-quenched samples, indicating that almost all of the hydrogen produced on the surface recombines to form H<sub>2</sub> gas. This indicates that a saturation state is reached.

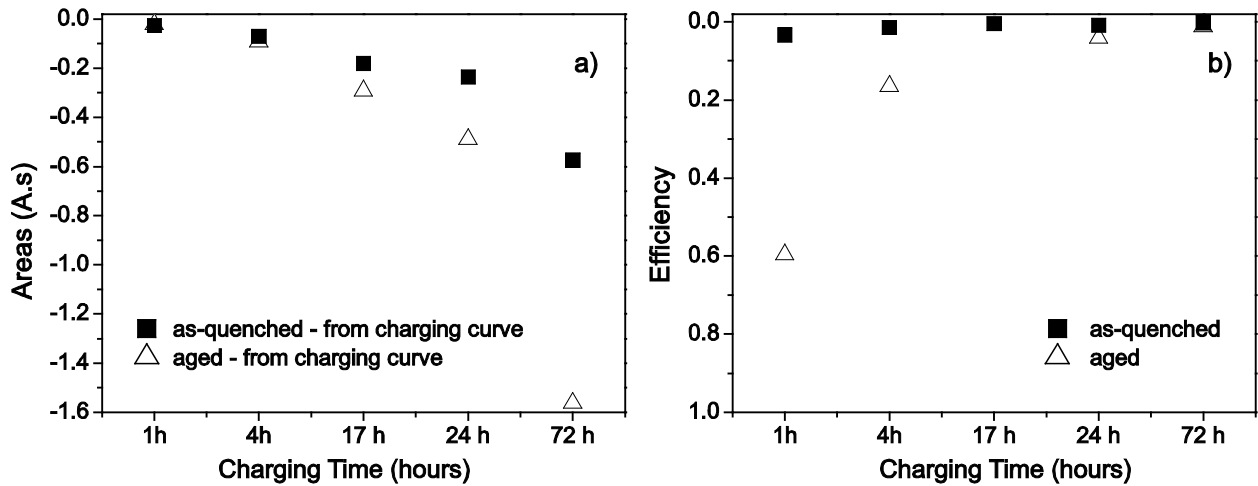


Figure 4.5. a) The area of the potentiostatic H-charging curves for the aged and as-quenched samples. b) The efficiency of H-charging expressed as Peak area I/H-charging area.

Regarding Peak II (related to the hydroxidation of Fe) of the aged samples, they also have a larger area than the as-quenched samples. This could be either due to the structural difference between the two materials, or because Peak II might be affected by Peak I. Since Peak II is not a hydrogen related peak and that hydrogen in the Aermet 100 is the primary focus of this paper, it is not further discussed here.

#### 4.3.2. Effect of nickel on the absorption of hydrogen (Peak III)

Peak III in Figure 4.2 is found to be present both in the as-quenched and aged specimens. This peak is not observed or reported in literature on CV of steels and iron, which suggests that the peak is caused by the hydrogenation during the charging step (this charging step is not present in experiments reported in literature). Additionally, the hydrogenation step did not cause a Peak III in our work on other steels [41], therefore the peak should be specific to the Aermet 100 microstructure or composition. In order to find out the origin of this peak, the compositions of different phases was looked into. In Figure 4.6 the compositions of the phases found in the as-quenched and aged samples are summarized. Figure 4.6a shows the composition of the as-quenched sample as obtained by means of TEM. The martensitic matrix is rich in Fe (~75 at.%), Co (~12 at.%) and Ni (~9.5 at.%). In Figure 4.6b and Figure 4.6c, the composition of the phases in the aged material is presented. Here the Ni content is about 25-30 at.% in the austenitic phase of the aged specimen (see Figure 4.6b); there is a much lower Ni content, about 5 at.%, in the ferrite phase (see Figure 4.6c). All mentioned compositions match very well with our Thermo-Calc calculations (~ 90% accuracy for most alloying elements).

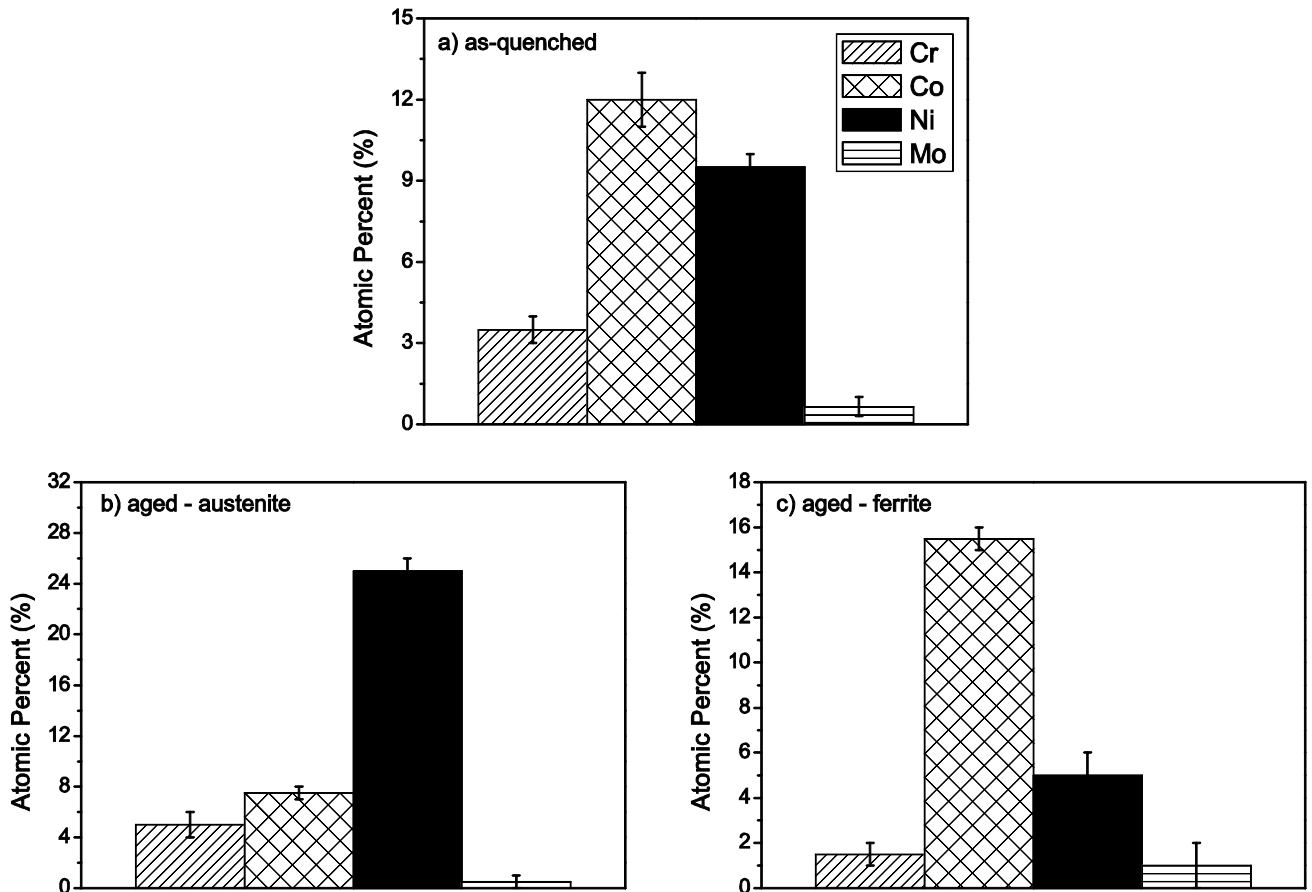


Figure 4.6. The composition of the matrix of Aermet 100 as observed by TEM in a) the as-quenched sample b) the austenite phase as observed after ageing at 835 K c) the ferrite phase as observed after ageing at 835 K.

CV experiments were performed on pure cobalt and nickel in order to identify Peak III since these are the two major constituents of different phases of martensite (or ferrite) and austenite, respectively. The CV results of the pure metals are presented in Figure 4.7. The position of Peak III (around  $-0.114$  V) matches well with a peak of pure nickel sample (Figure 4.7a). This peak is generally assigned to the oxidation of absorbed hydrogen in Ni [34]. Cobalt, on the other hand, does not show any clear common peak with Aermet 100 (see Figure 4.7b). The CV of pure Ni and Co were also performed after H-charging for 4 h in a solution with thiourea. Peak III readily occurs in scan 1, however the peak area is smaller than the one in scan 3. This indicates that hydrogen was easily absorbed by the Ni samples. Nickel is known to absorb hydrogen forming nickel hydrides [42].

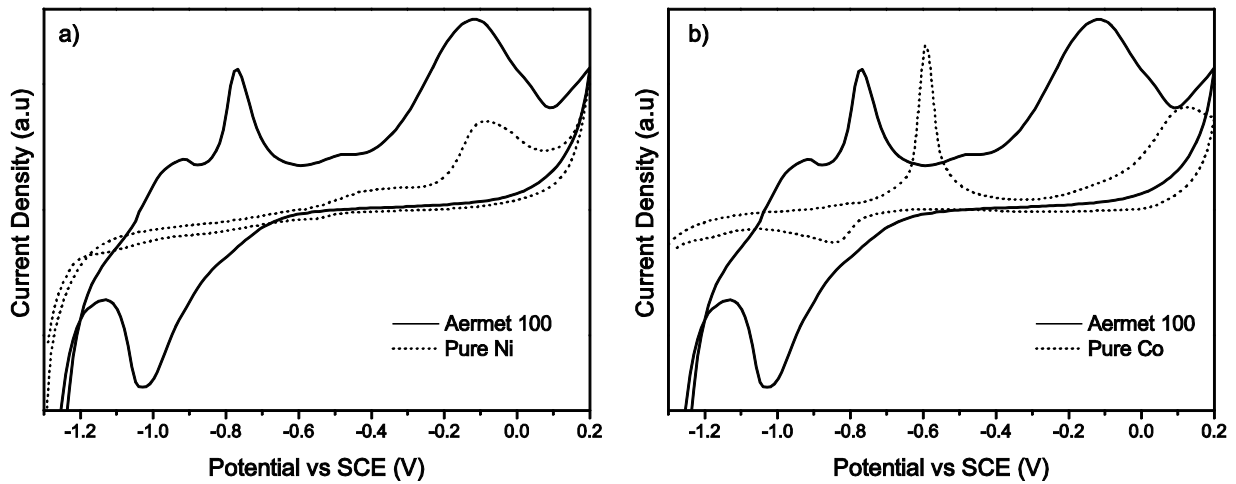


Figure 4.7. CV results of a) a pure nickel sample and b) a pure cobalt sample; compared with aged Aermet 100 in a 1 M KOH solution with thiourea. The scan rate was 0.01 V/s.

Noting that the pure Ni specimen shows the same peak after hydrogenation as the one found in Aermet 100, Peak III is suggested to form through regions rich in nickel. Apart from the matrix, also the composition of precipitates was investigated in order to check if they contain Ni as a potential source of Peak III. Precipitates were found scattered through the microstructure. Many precipitates were investigated by means of EDS and 93% of all precipitates showed enrichment in Cr, Fe and Mo but not in Ni. This is in agreement with the ThermoCalc calculations that also did not predict any Ni-enriched precipitates. The grain boundary areas were also investigated in order to see if different type of precipitates were to be found, but enrichment in Ni was not observed.

In Figure 4.8, the relation between the Ni content of the phases present in the samples and the Peak III area is presented. The lower Ni content in this figure is pertaining to martensite, the only phase in the as-quenched sample, whereas the higher Ni amount is pertaining to the austenite of the aged sample. The higher Ni content of the austenitic phase in the aged sample results in bigger Peak III areas, which in return implies a higher absorption/desorption of hydrogen by these samples, only due to nickel. Investigations on H in Fe-Ni binary system show that as the Ni amount increases, hydrogen solubility also increases [43, 44]. The higher amount of Ni in the austenite in Aermet 100 aged material could suggest that locally a structure closer to pure Ni is resembled which results in higher amounts of absorbed H. To summarize, it is highly likely that the source of the increase of the nickel related peak (Peak III in Figure 4.2) in the CV scan is due to the Ni in the austenite phase in the aged material. Nickel in austenite as a reversible trap is recognized in the literature [4] and the fact that Peak III is visible also implies this trap's reversible nature.

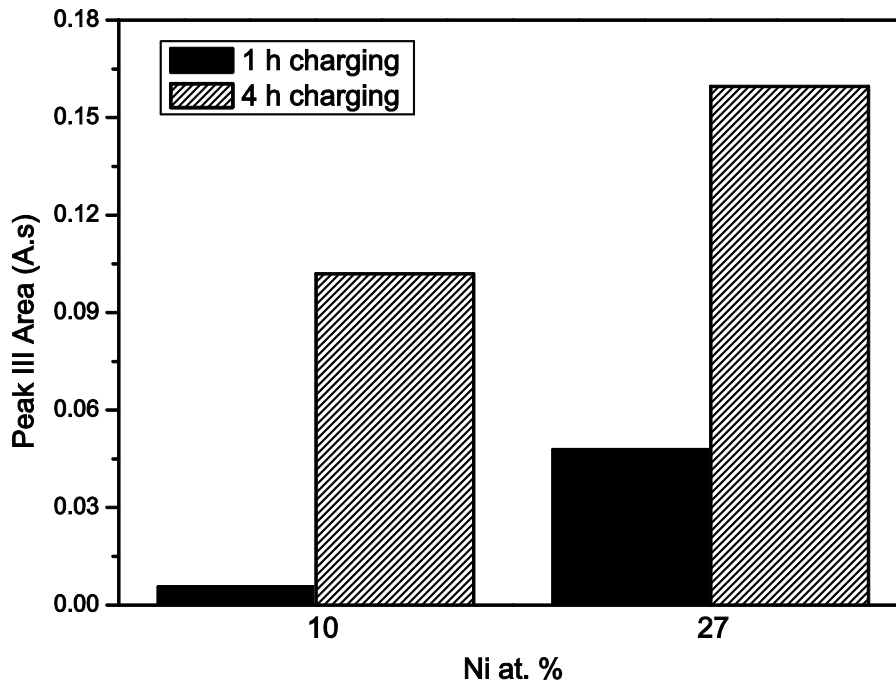


Figure 4.8. Peak III areas of samples with different content of Ni in the phases; the ferrite in the as-quenched sample contains about 10 at.% Ni, the austenite phase in the aged sample contains about 27 at.% Ni (and the ferrite about 5 at.%).

#### 4.4. Conclusions

Cyclic voltammetry is a useful tool to fast and easily identify the diffusible hydrogen in steels on the basis of which the microstructural aspects that enhance hydrogen absorption were pinpointed in Aermet 100 steel. The method in its current state does not allow a quantitative analysis of the detected hydrogen because the inward diffusion distance is not exactly known. However, by relatively comparing the desorbed H for two different heat treatments, it was shown that the aged material that contained austenite absorbs higher amounts of hydrogen than material that did not contain austenite. On that basis it is concluded that austenite enhances the absorption of hydrogen. The ratio of the CV peak areas to the potentiostatic charging curve integrations showed that the efficiency of H absorption is higher for aged specimens.

It is also concluded that some alloying elements can enhance the H uptake. In this case Ni might be acting as an easy route for H-absorption. Thus the addition of alloying elements meant to improve the quality of the steel for certain applications might result in an altering of the proneness of the steel to H-embrittlement by increasing the number of reversible traps, which are known to be detrimental for H-embrittlement through acting like a reservoir for diffusible H.

## **Acknowledgements**

The authors gratefully acknowledge R. W. A. Hendrikx and N.M. van der Pers for helping with XRD related sample preparations and discussions. We would also like to thank E. Zacharaki for her experimental support and J.M.C. Mol for the valuable discussions. This work is financially supported by the Delft University of Technology and is part of a Materials innovation institute (M2i) research program with project number MC6.06283.

## References

1. Dahl, J.M., *New Requirements for Ferrous-Base Aerospace Alloys*, in *Alloy TechZone2000*, Carpenter Technology Corporation: Reading, PA, USA.
2. Dautovic.Dp and S. Floreen, *Metallurgical Transactions*, 1973. **4**(11): p. 2627-2630.
3. Pound, B.G., *Acta Materialia*, 1998. **46**(16): p. 5733-5743.
4. Thomas, R.L.S., et al., *Metallurgical and Materials Transactions a-Physical Metallurgy and Materials Science*, 2002. **33**(7): p. 1991-2004.
5. Thompson, A., *Metallurgical and Materials Transactions B*, 1973. **4**(12): p. 2819-2825.
6. Gangloff, R.P., *Hydrogen-assisted Cracking*, in *Comprehensive Structural Integrity*, I. Milne, R.O. Ritchie, and B. Karihaloo, Editors. 2003, Pergamon: Oxford. p. 31-101.
7. Ayer, R. and P.M. Machmeier, *Metallurgical Transactions a-Physical Metallurgy and Materials Science*, 1993. **24**(9): p. 1943-1955.
8. Novotny, P.M. *An aging study of Carpenter AerMet® 100 alloy*. in *34th Mechanical Working and Steel Processing Conference*. 1992. Montreal, Canada: Iron and Steel Society.
9. Yoo, C.H., et al., *Metallurgical and Materials Transactions a-Physical Metallurgy and Materials Science*, 1996. **27**(11): p. 3466-3472.
10. Li, D.M., R.P. Gangloff, and J.R. Scully, *Metallurgical and Materials Transactions a-Physical Metallurgy and Materials Science*, 2004. **35A**(3): p. 849-864.
11. Thomas, R.L.S., J.R. Scully, and R.P. Gangloff, *Metallurgical and Materials Transactions a-Physical Metallurgy and Materials Science*, 2003. **34**(2): p. 327-344.
12. Devanathan, M.A.V., *Proceedings of the Royal Society of London Series a-Mathematical and Physical Sciences*, 1962. **267**(1329): p. 256-&.
13. Pound, B.G., *Acta Metallurgica et Materialia*, 1990. **38**(12): p. 2373-2381.
14. Pound, B.G., *Acta Metallurgica et Materialia*, 1991. **39**(9): p. 2099-2105.
15. Sundaram, P.A. and D.K. Marble, *Journal of Alloys and Compounds*, 2003. **360**(1-2): p. 90-97.
16. Evers, S., C. Senoz, and M. Rohwerder, *Science and Technology of Advanced Materials*, 2013. **14**(1).
17. Czerwinski, A. and R. Marassi, *Journal of Electroanalytical Chemistry*, 1992. **322**(1-2): p. 373-381.
18. Czerwinski, A., R. Marassi, and S. Zamponi, *Journal of Electroanalytical Chemistry*, 1991. **316**(1-2): p. 211-221.
19. Czerwinski, A., et al., *Journal of Electroanalytical Chemistry*, 1995. **386**(1-2): p. 207-211.
20. Lukaszewski, M. and A. Czerwinski, *Electrochimica Acta*, 2003. **48**(17): p. 2435-2445.
21. Lukaszewski, M. and A. Czerwinski, *Journal of Solid State Electrochemistry*, 2008. **12**(12): p. 1589-1598.
22. Lukaszewski, M., K. Hubkowska, and A. Czerwinski, *Physical Chemistry Chemical Physics*, 2010. **12**(43): p. 14567-14572.
23. Lukaszewski, M., et al., *Journal of Solid State Electrochemistry*, 2003. **7**(2): p. 69-76.
24. Uluc, A.V., et al., *Journal of Electroanalytical Chemistry*, 2014. **revised version submitted**.
25. Albani, O.A., et al., *Electrochimica Acta*, 1990. **35**(9): p. 1437-1444.
26. Albani, O.A., et al., *Electrochimica Acta*, 1986. **31**(11): p. 1403-1411.
27. Diaz, B., et al., *Electrochimica Acta*, 2009. **54**(22): p. 5190-5198.
28. Geana, D., A.A. Elmiligy, and W.J. Lorenz, *Journal of Applied Electrochemistry*, 1974. **4**(4): p. 337-345.
29. Guzman, R.S.S., J.R. Vilche, and A.J. Arvia, *Electrochimica Acta*, 1979. **24**(4): p. 395-403.
30. Guzman, R.S.S., J.R. Vilche, and A.J. Arvia, *Journal of Applied Electrochemistry*, 1981. **11**(5): p. 551-562.
31. Machado, S.A.S. and L.A. Avaca, *Electrochimica Acta*, 1994. **39**(10): p. 1385-1391.
32. Veleva, L., et al., *Journal of Electroanalytical Chemistry*, 2002. **537**(1-2): p. 85-93.
33. Veleva, L., et al., *Journal of Electroanalytical Chemistry*, 2005. **578**(1): p. 45-53.
34. Visscher, W. and E. Barendrecht, *Journal of Applied Electrochemistry*, 1980. **10**(2): p. 269-274.
35. Vracar, L. and B.E. Conway, *Journal of Electroanalytical Chemistry*, 1990. **277**(1-2): p. 253-275.
36. Pers, N.M.v.d., et al., *Review of Scientific Instruments*, 2013. **84**(4): p. 045102.
37. Pourbaix, M., *Atlas of electrochemical equilibria in aqueous solutions*. 1974: NACE International.
38. Conway, B.E. and G. Jerkiewicz, *Journal of Electroanalytical Chemistry*, 1993. **357**(1-2): p. 47-66.

39. Cullity, B.D. and S.R. Stock, *Elements of X-Ray Diffraction*. 3 ed. 2001: Prentice Hall.
40. San-Martin, A. and F. Manchester, *Journal of Phase Equilibria*, 1990. **11**(2): p. 173-184.
41. Uluc, A.V. and A.J. Bottger, to be submitted, 2014.
42. Hampton, M.D., et al., eds. *Hydrogen Materials Science and Chemistry of Metal Hydrides*. Vol. XI. 2002, Kluwer Academic Publishers: The Netherlands. 357-359.
43. Beck, W., et al., *Metallurgical Transactions*, 1971. **2**(3): p. 883-&.
44. Stafford, S.W. and R.B. Mclellan, *Acta Metallurgica*, 1976. **24**(6): p. 553-558.



# CHAPTER 5



# CHAPTER 5: The Effect of Austenite and V-carbide on the Diffusible Hydrogen in Steels for Automotive Applications

---

*Hydrogen trapping behavior of SAE 52100 steel of two different heat treatments, one with and the other without austenite and a Mn-based TWIP steel of two different compositions, with and without vanadium carbide, were investigated. The samples were electrochemically loaded with hydrogen in a 1 M KOH solution, and the hydrogen desorption behavior was studied by means of cyclic voltammetry (CV) and thermal desorption analysis. The amounts of diffusible hydrogen were determined as an indication for the susceptibility to H-embrittlement. It was found that the presence of austenite in SAE 52100 leads to higher amounts of desorbed hydrogen. For the TWIP steel it was observed that the absence of vanadium carbides leads to higher amounts of desorbed hydrogen. The results also indicate that CV is a more sensitive method than thermal desorption to analyze the effect of microstructural features on the amount of diffusible hydrogen. This is mainly because CV is able to identify differences between the two materials regarding the amount of H, whereas thermal desorption is not.*

---

## 5.1. Introduction

Resistance to hydrogen embrittlement is one of the key requirements for steels in automotive applications, along with fatigue resistance, high hardness, good ductility, toughness and corrosion resistance [1, 2]. In order to improve the performance of bearing materials and twinning induced plasticity (TWIP) steels, reduction of H uptake and/or the development of microstructures less prone to H embrittlement are necessary.

Hydrogen's deteriorating effect on the resistance to fatigue of bearing steels gained interest in the 1960's with the finding that the fatigue life of bearing steels depends on the lubricant used and that the accelerated pitting of steel balls by a water contaminated lubricant is a result of hydrogen embrittlement [3]. Mechanically stimulated H absorption occurs from H generation by water and oxygen in lubricants [4], as well as from environmental gases [5, 6]. Depending on the conditions, failure through crack formation starts either at the surface or the subsurface of the bearing, heating by friction and the absorbed H then enhances fracture propagation and spalling [4-6].

Ciruna et al [7], in one of the earlier works, studied the effect of H on fatigue life of SAE 52100 and AISI 440C steels (both used in bearing applications) and found that less hydrogen was charged into the AISI 440C steel by cathodic electrochemical loading. Moreover the AISI 440C steel had a higher fatigue resistance than the SAE 52100 steel. To date, the reason behind this difference in fatigue behavior is unknown [2]. One possible explanation is that the Cr in the AISI 440C stainless ferritic steel acts as a trap for H and therefore retards the H diffusion. Indeed, a lower diffusivity of H in AISI 440C (that contains a higher amount of Cr) than in the low-alloyed ferritic steel (0.09C-0.5Mn wt. %) was observed [2]. The SAE 52100 material can be heat treated in various ways to obtain different microstructures such as martensite, bainite or pearlite. It was found that the softer lower bainitic structure is less susceptible to hydrogen embrittlement than the martensitic material because of its higher toughness and ductility [8]. Besides the effect of alloying elements on fatigue resistance, the effect of austenite on the fatigue lifetime of the bearing steels has also been investigated [2, 9, 10]. Although different hypotheses exist, in general it is supposed that for high stress applications the retained austenite plays a beneficial role by enhancing the development of a mean compressive stress upon transforming to martensite [2, 10], whereas for low stress applications no transformation occurs and the austenite content is suggested to stay at a minimum in order to avoid plastic deformation [9].

Austenitic Mn-based twinning induced plasticity (TWIP) steels are one of the high potential material class for the automotive industry due to their high strength combined with a high ductility (formability) [1, 11]. The high ductility in ultra-high Mn TWIP steels is achieved by the formation of stress-induced twins and (HCP, BCC) martensite formation. Formation of twins and martensite depends on the chemical composition, temperature and strain. Implementation of these steel grades has been hindered by reports on delayed hydrogen-assisted fracture of formed parts [11-13]. Several microstructural features attributed to have an effect on hydrogen embrittlement in TWIP steels are dislocation density [14, 15], martensite content [16], presence of deformation twins [11, 15] and grain boundaries [11, 15]. Aluminium is added to the microstructure to suppress the martensite formation and to increase the stacking fault energy [17]. Recently it has been shown that Al indeed enhances the resistivity to delayed fracture [12, 15, 18]. Experiments on low Mn, V-carbide containing steels showed that V-carbides trap a large part of H [19] and for low Mn, Cr-V-C steels containing V-carbides an improved resistivity to H embrittlement was found [20]. Direct observation of vanadium carbides as trapping sites for H was made by Takahasi et al. [21]. The results suggested that the misfit dislocation cores at semi-coherent interfaces of the platelets are deep trapping sites for hydrogen.

In this work we utilize a rather fast and easy method based on cyclic voltammetry (CV) to investigate the H uptake and release of SAE 52100 (two different heat treatments, i.e. with and without austenite) and austenitic Mn-based TWIP steel (two different vanadium contents, i.e. with and without V-carbides). The SAE52100 material in two heat treatments gives the opportunity to study the effect of austenite on H sorption/desorption properties of steels. Whereas our selection of Mn-based TWIP steels with two different vanadium contents provides direct evidence on H-sorption/desorption differences in presence/absence of V-carbides. The CV method has been successfully applied to study H in Pd-alloys (Chapter 2) [22-24]. CV has also been used extensively in oxidation/passivation and corrosion of pure metals including Fe and steels [25-35]. However, the hydrogen uptake properties of steels have not yet been investigated in detail by means of CV except for an ultra-high-strength steel (Aermet 100) in Chapter 4 [36]. For SAE52100 material, the CV findings are compared to the results using mass spectrometry technique. Furthermore, X-ray diffraction (XRD) method was used in order to get insight about the overall structure.

## 5.2. Experimental procedure

### 5.2.1. Characterization methods

X-ray powder diffraction patterns were recorded in a Bragg-Brentano geometry with a Bruker D8 Advance diffractometer equipped with a Vantec position sensitive detector and graphite monochromator [37]. Data collection was carried out at room temperature using Co K $\alpha$  radiation ( $\lambda = 0.179026$  nm) in the  $2\theta$  range between  $30^\circ$  and  $130^\circ$ , a step size of  $0.034^\circ 2\theta$ , and a measuring time per step of 2 s. The samples were placed on a Si (510) substrate and rotated during measurement. Data evaluation was done with the Bruker program EVA. Volume fraction of austenite of the samples were determined by the “direct comparison method” [38].

Vickers microhardness tests were performed with a Buehler Automatic Microhardness Tester using 500 g load. Hardness data are averages over 15 indents.

### 5.2.2. Materials

#### *SAE 52100*

The materials were provided as  $\varnothing 18$  mm discs with 2 mm thickness by SKF Engineering & Research Centre Netherlands. The bearing material has the composition given in Table 5.1 [39]. The materials were obtained in two different heat treatment states resulting in different

microstructures and mechanical properties. The procedures of these heat treatments are schematically shown in Figure 5.1.

Table 5.1. Composition of SAE 52100 steel (balance Fe).

	<b>C</b>	<b>Cr</b>	<b>Ni</b>	<b>Mn</b>	<b>Mo</b>	<b>Si</b>	<b>Al</b>	<b>S</b>	<b>P</b>
<b>wt. %</b>	1.01	1.36	0.16	0.32	0.04	0.25	0.0013	0.020	0.013

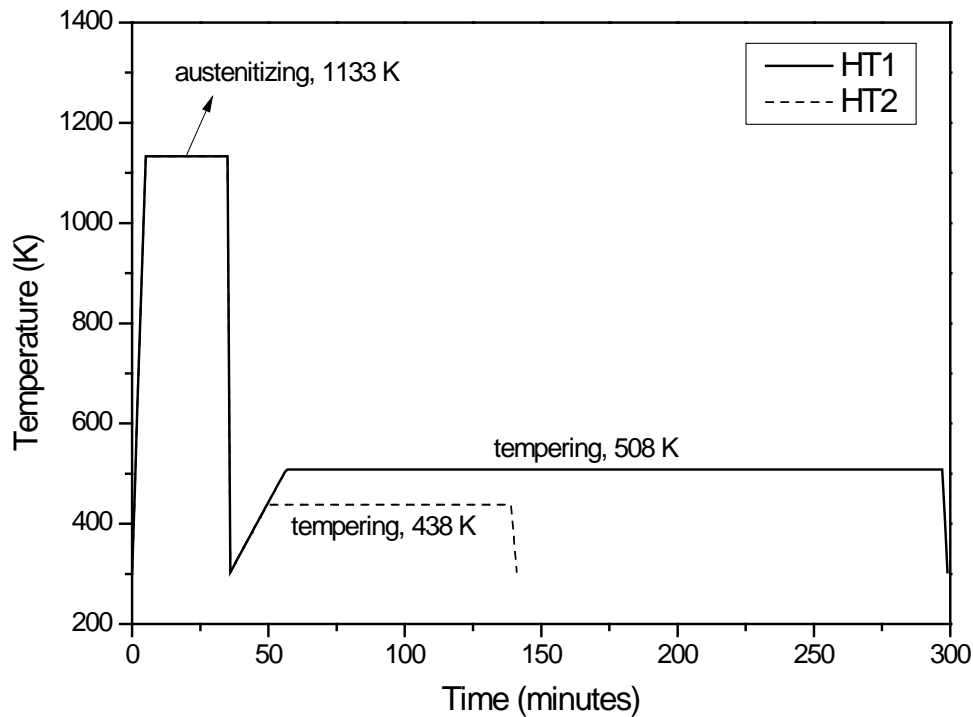


Figure 5.1. Schematic of the two heat treatments applied to the SAE 52100 bearing steel.

The materials were austenitized at 1133 K for 30 minutes followed by quenching to 303 K which resulted in a martensitic structure with about 14 vol. % retained austenite ( $\gamma_R$ ) [39].

#### a) Heat treatment 1 (HT1)

For heat treatment HT1, the austenitization treatment was succeeded by tempering of the material at 508 K for 4 h followed by quenching to 303 K. The XRD pattern of the resulting material is given in Figure 5.2. The peaks correspond to ferrite ( $\alpha$ ) and cementite ( $\theta$ ). At this tempering temperature, the retained austenite is completely decomposed into ferrite and cementite. A detailed TEM work on SAE 52100 [40] with a very similar heat treatment (tempering temperature 523 K for 4 h) reveals a very complex microstructure consisting of ferrite as the main phase, and, cementite and transition carbides ( $\eta$ - $M_2C$  and  $\chi$ - $M_5C_2$  carbides). Besides incoherent undissolved (micron-sized) cementite particles, a mixture of coherent cementite

precipitates,  $\chi$ - $M_5C_2$  carbides (sizes from a few nm to 500 nm), and  $\eta$ -carbide is observed. The average  $\eta$ -carbide size observed was  $15 \pm 20$  nm in width and  $100 \pm 35$  nm in length; the majority of these carbides were coherent with the matrix.

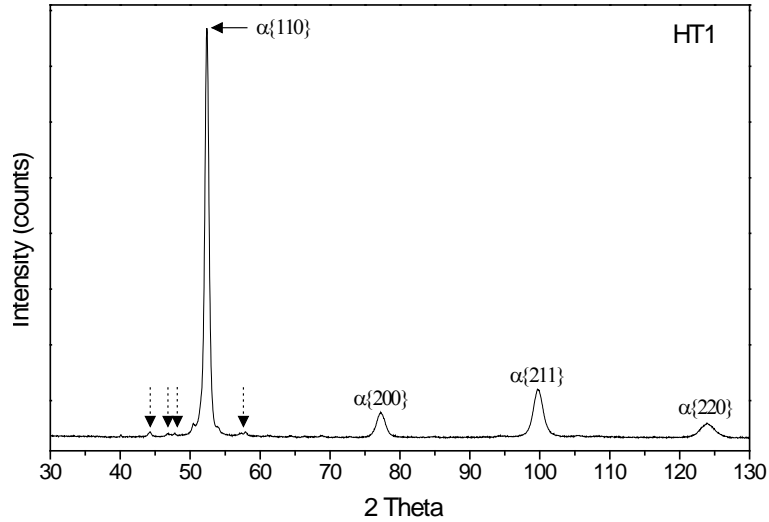


Figure 5.2. XRD scan of SAE 52100 bearing steel HT1. Dashed arrows indicate the undissolved cementite ( $\theta$ ) diffraction peaks [39].

*b) Heat treatment 2 (HT2)*

For heat treatment HT2, the austenitization treatment was succeeded by tempering at 438 K for 1.5 h followed by quenching to 303 K. An XRD pattern of the material is shown in Figure 5.3. The peaks come from: ferrite ( $\alpha$ ), cementite ( $\theta$ ) and retained austenite ( $\gamma_R$ ). The austenite amount in this sample was 13.4 vol. %, calculated with the direct comparison method [38].

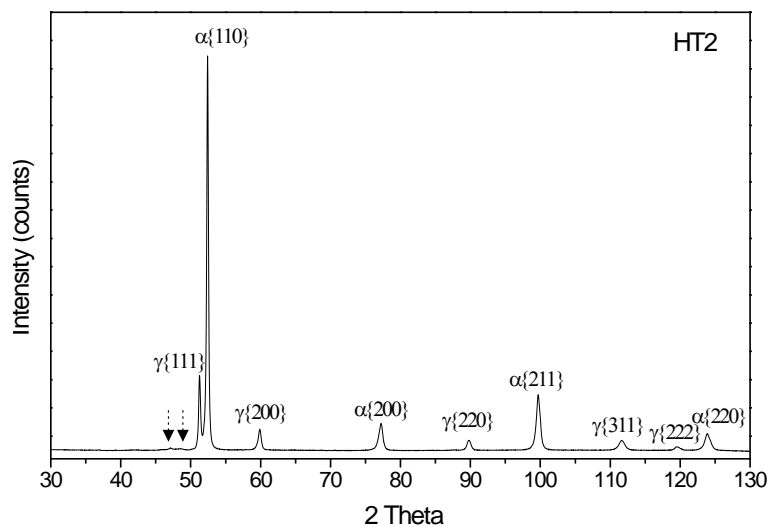


Figure 5.3. XRD scan of SAE 52100 bearing steel HT2. Dashed arrows indicate the undissolved cementite ( $\theta$ ) diffraction peaks [39].

Transmission electron microscopy analysis of SAE 52100 [39, 41] heat treated in a very similar way (428 K for 1 h) again reveals a very complex microstructure including: ferrite and austenite as the main phases and, cementite and transition carbides ( $\eta$ -M<sub>2</sub>C). Besides incoherent undissolved (micron-sized) cementite particles, most precipitates are small and coherent with the matrix: plate-like cementite forming lamellae of widths smaller than 25 nm and lengths smaller than 100 nm, and  $\eta$ -carbide precipitates of about 25 nm in diameter i.e., precipitates are considerably smaller than the ones found in the HT1.

#### *Austenitic Mn-based Twinning Induced Plasticity (TWIP) Steels*

The materials with compositions shown in Table 5.2 were obtained from Tata Steel Nederland as 4 mm thickness sheets in the cold-rolled and recrystallization-annealed condition. These were cut into 1 cm x 1 cm squares for electrochemical measurements.

Table 5.2. Composition of the TWIP steels (balance Fe).

	C	Si	Mn	Al	V	$\sigma_{0.2}$	$\sigma_{UTS}$	$\epsilon_{UTS}$	$\epsilon_f$
	wt. %	(MPa)	(MPa)	(%)	(%)				
<b>With V-carbide</b>	0.72	0.25	14.5	2.3	0.16	622	978	42.2	45.8
<b>Without V-carbide</b>	0.75	0.25	14.9	2.4	0.004	544	956	52.1	52.3

As indicated in Table 5.2, the two materials differ in compositions, the main difference being the amount of vanadium. The materials are fully austenitic at room temperature, as confirmed by the XRD pattern for the sample with V-carbide (Figure 5.4). The V-carbides are very small and finely distributed in the microstructure and therefore are not visible with XRD. The presence of V-carbide is indirectly confirmed by the increase in the yield strength of the higher vanadium content sample as indicated in Table 5.2. The heat treatments of the two steels were the same and the increase in the yield strength is attributed to the presence of vanadium carbide precipitates in the sample with 0.16 wt.% V (with V-carbide) [42]. The increase in the yield strength by V-carbide is studied by transmission electron microscopy and stress-strain analysis for TWIP steels with and without V-carbide with similar heat treatments [42].

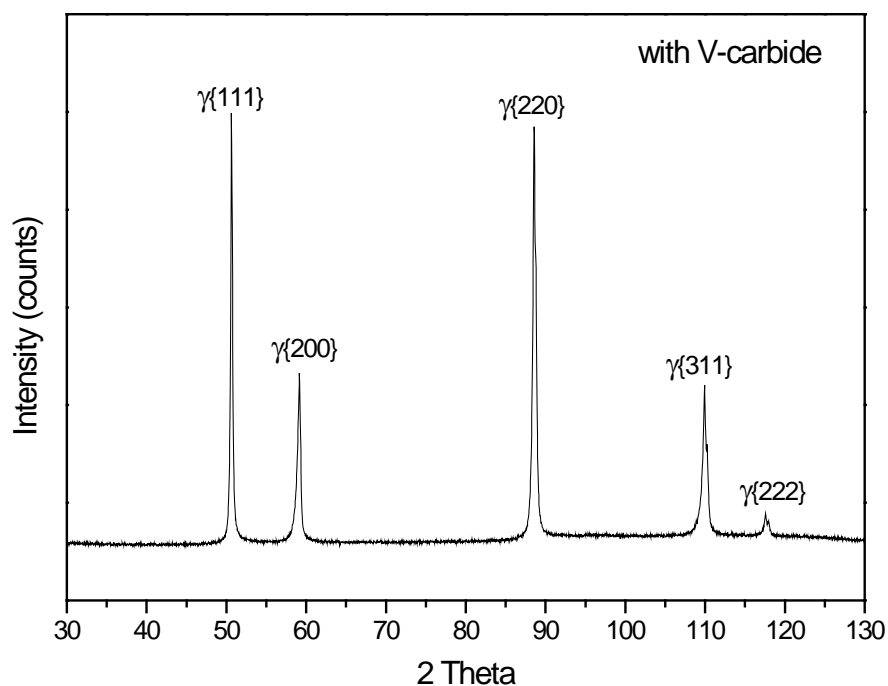


Figure 5.4. XRD scan of fully austenitic Mn-based TWIP steel with V-carbide.

### 5.2.3. Electrochemical method

During the cyclic voltammetry experiments, the potential was swept between -1.3 V to 0.2 V starting at -1.3 V with a scan rate of 0.01 V/s. The electrolyte was 1 M KOH with 4 g/l thiourea added as a recombination poison for some experiments. The CV measurements were performed in a KOH solution to prevent corrosion from playing a major role. The loading potential was selected as -1.3 V to ensure hydrogen evolution on the working electrode. Loading times were varied from 1 h to 17 h. The reference electrode was a standard calomel electrode (SCE) and the counter electrode was Pt. The details of the electrochemical method were published in previous papers [24, 36] but in summary was as follows: (1) two repeated cycles of CV, the first of these is regarded as a cleaning step of the surface and the second is the reference scan, (2) subsequent potentiostatic hydrogen loading at -1.3 V and (3) two repeated cycles of CV which are used to analyze the H-desorption behavior.

### 5.2.4. Mass spectrometry

Thermogravimetric Analysis (TGA) equipment utilized was a Setaram Setsys Evolution combined with an Omnistar quadrupole mass spectrometer by Pfeiffer Vacuum.

The TGA/MS experiments were performed in two cycles as schematically depicted in Figure 5.5. During the first cycle, H desorbs out of the sample. Because all H is already desorbed after the first cycle, the second cycle serves as a reference measurement to estimate the background. The

heating was performed from 300 K to 900 K with 5 K/min heating rate. Ar gas with a flow rate of 60 ml/min was used as the carrier gas.

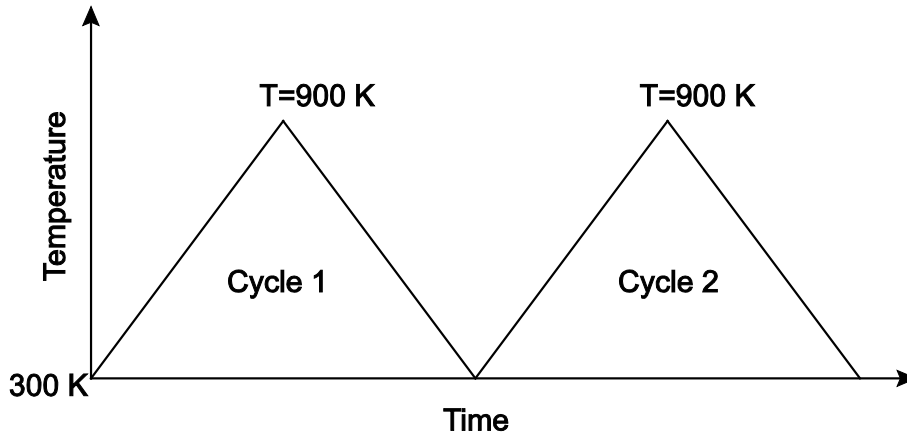


Figure 5.5. Schematics of the TGA/MS experiments: Cycle 1 is the actual measurement, whereas Cycle 2 is used as a reference. Temperature scan is from room temperature (RT) to  $T = 900$  K.

The Multiple Ion Determination (MID) data acquisition method [43] was used for the mass spectrometer measurements. The mass-to-charge ratios ( $m/e$ ) tracked by the MID method and the corresponding ions are given in Table 5.3.

Table 5.3. The mass-to-charge ratio ( $m/e$ ) followed during the MS experiments and their corresponding main components. The terms in brackets indicate contributions due to isotopes.

Mass-to-charge ratio ( $m/e$ )	Corresponding component
1	$H^+$
2	$H_2^+$
14	$N^+$
16	$O^+$
17	$OH^+ (O^+)$
18	$H_2O^+, (Ar^{++}, OH^+, O^+)$
20	$Ar^{++}, (H_2O^+, OH^+)$
28	$N_2^+$
29	$(N_2^+)$
32	$O_2^+$
36	$(Ar^+)$
38	$(Ar^+)$
40	$Ar^+$

In order to relate the MS results to H<sub>2</sub> amounts calibration was performed taking into account the isotope effect and the effect of fragmentation; details can be found in Appendix A. Sensitivity was also taken into account.

### 5.3. Results and discussion

#### 5.3.1. SAE 52100

In Figure 5.6, the CV scans of HT2 material scan 3 i.e. after H-loading the material for 1 h, 4 h and 17 h, are shown. For both heat treatments (HT1 and HT2) the peak denoted Peak I clearly shifts to higher potential when the loading time increases (see also Figure 5.7). A similar Peak I was related to desorption of absorbed hydrogen from Aermet 100 after potentiostatic H-loading in our recent work in Chapter 4 [36]. Peak I of Aermet 100 was considerably broader than the one observed here and therefore a clear peak shift was not detected.

On the other hand, a clear shift of the hydrogen desorption peak to more positive potentials was also observed for Pd-alloys [24] upon increasing the H-loading time. In that case the observation was related to the amount of H in the samples and the time needed to desorb; the potential axis in a cyclic voltammogram can also be regarded as a time axis, therefore a higher amount of H needs a longer desorption time [24].

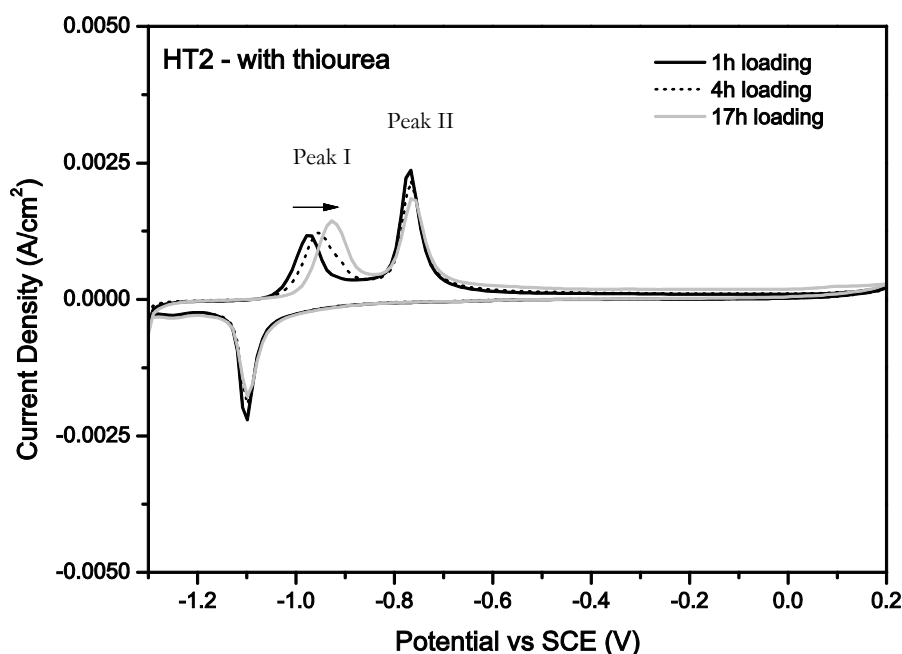


Figure 5.6. CV scan of HT2 material (scan 3) after H-loading for 1 h, 4 h and 17 h in 1 M KOH solution with thiourea.

For SAE 52100, the peak shift observed upon longer loading times is also assigned to a larger amount of H absorbed. This is confirmed by the Peak I areas (see Figure 5.8) that increase when the loading times are longer.

The behavior of Peak II which is related to the hydroxidation of Fe [36] is considerably different than Peak I. This is better visible in Figure 5.7, which shows that while the peak potential of Peak I strongly depends on the duration of H-loading, Peak II is not at all affected by H-loading times nor by the type of heat treatment. The different heat treatments, however, do have an effect on the peak potential of Peak I. Peak I of HT1 has more anodic peak potentials than HT2 for all H-loading times. A more anodic potential of Peak I could suggest that HT1 absorbs more hydrogen than HT2 for the same H-loading time and therefore needs longer times to desorb, hence the more positive potentials.

This is however not the case as can be deduced from Figure 5.8, where the Peak I areas are presented for HT1 and HT2. In all cases HT2 has a larger peak area but a lower peak potential than HT1. This suggests that the difference in Peak I potential (Figure 5.7) is not caused by a difference in H amounts. Also kinetics does not seem to play a role since the diffusivity of H in the FCC austenite is smaller [44-46] than the BCC ferrite [46-49], which would have resulted in more anodic potentials for HT2 material with 13.4 vol% austenite, as more time to desorb is required.

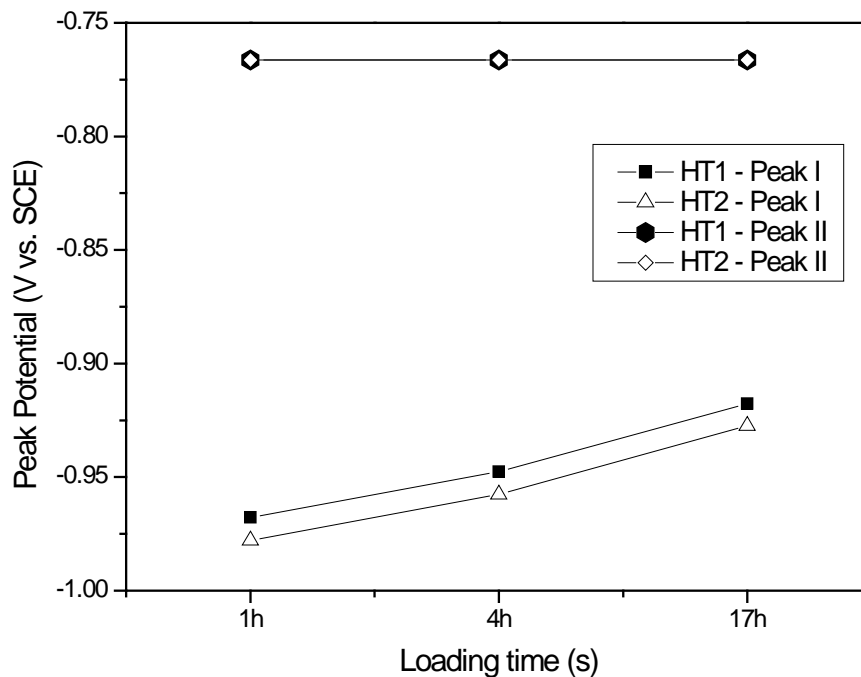


Figure 5.7. Peak I and Peak II of scan 3 (H-desorption) for different heat-treated SAE 52100 specimen.

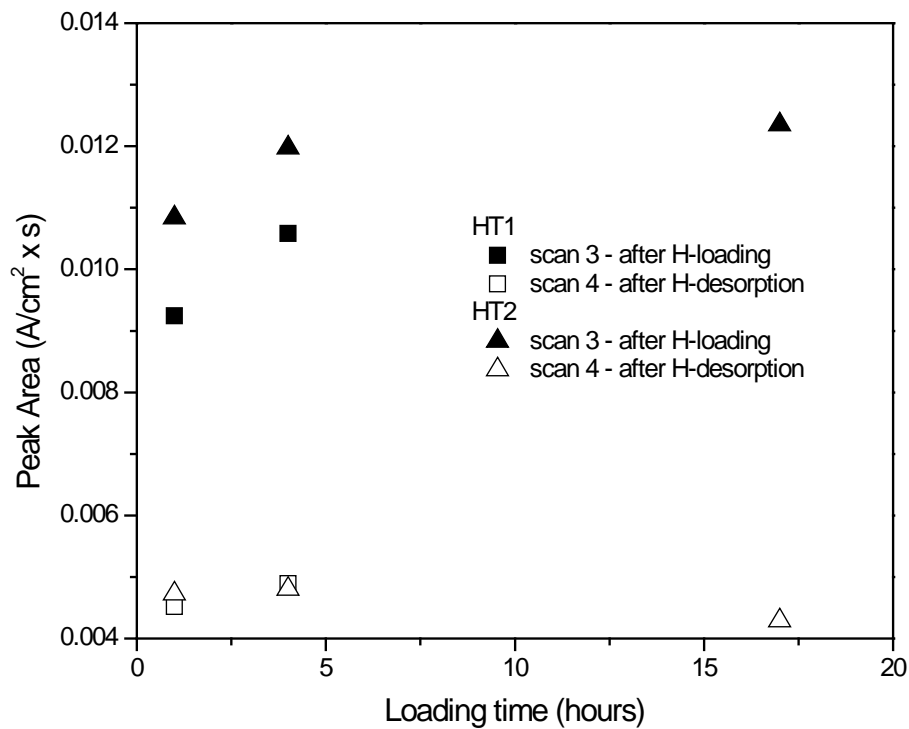


Figure 5.8. Peak areas of desorbing H from SAE 52100 material. Both HT1 and HT2 are H-loaded in the presence of thiourea in the solution.

Therefore, the difference in the peak potentials of HT1 and HT2, is suggested to be related to the interaction energy between the hydrogen and ferrite vs. austenite. In this case it would suggest that the binding energy of H with the overall traps in ferrite is larger than those in austenite [44].

Figure 5.8 shows that HT2 absorbs higher amounts of hydrogen than HT1 material. This difference could be explained by the absence of austenite in the HT1 heat-treated material since the H-solubility in the FCC lattice is known to be higher than the BCC lattice [46]. Additionally, most of the precipitates are coherent for HT2 material. The lower diffusivity of H in the austenite implies higher solubility of H [46, 50], so the difference in the higher amounts of H desorbing out of the HT2 sample could be related to the austenite in the HT2.

Titanium carbide, vanadium carbide and niobium carbide particles are known to trap hydrogen and consequently reduce the deteriorating effect of hydrogen on embrittlement [21, 51, 52]. Incoherent precipitates generally have a higher H binding energy and that results in irreversible trapping whereas smaller coherent particles have a tendency to act as reversible traps [53-55]. The irreversible traps consequently reduce hydrogen embrittlement by inhibiting diffusion of H. Besides the absence of austenite, the HT1 heat treatment leads to larger but mostly coherent carbide precipitates in the microstructure [39]. The fact that there are somewhat more incoherent

precipitates and larger strain fields around the (larger) precipitates, it is feasible that also some hydrogen is trapped irreversibly. This also would result in less desorbing H from HT1 samples.

All in all, from the above explanation it is concluded that the amount of free diffusible H in the HT2 sample is expected to be higher than the HT1 material [46, 56]. This is confirmed by the peak area observations on Figure 5.8, which also shows that the Peak I areas for scan 4 of both materials are similar and close to zero, indicating that most of the hydrogen is desorbed.

In order to distinguish whether higher peak areas of HT2 is caused indeed by the material's capacity of absorbing higher amounts of hydrogen, or whether the phenomena is a consequence of surface related properties during the H-loading step, the areas of H-loading curves were considered. The results, in Figure 5.9, show that the areas of the loading curves are about the same. This suggests that the difference in H-desorption peak areas (Peak I) originates from the difference in microstructure.

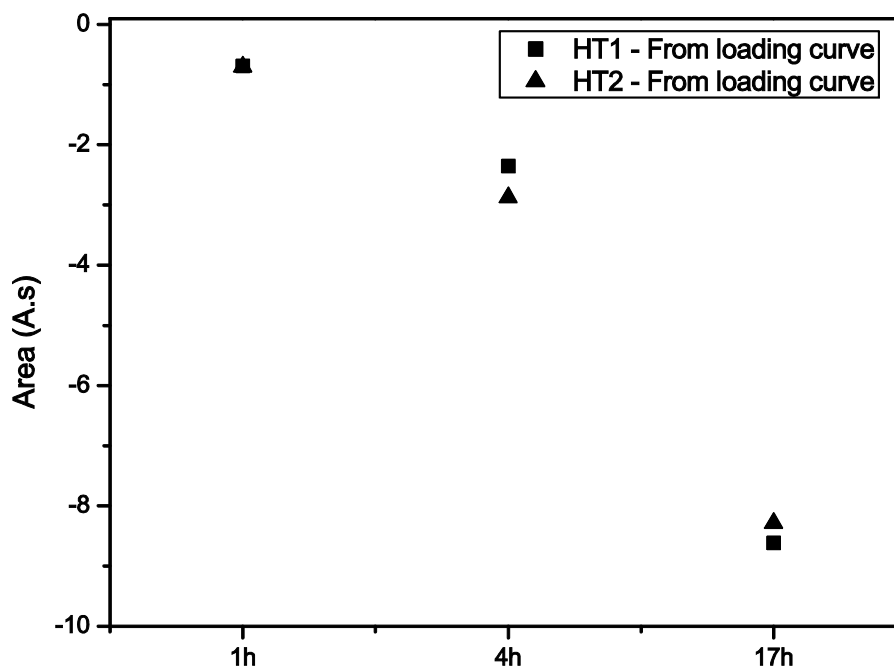


Figure 5.9. H-loading curve areas for HT1 and HT2.

In Figure 5.10, the microhardness test results are presented for HT1 and HT2 heat-treated samples with and without H. The HT1 material is softer than the HT2 material. Some effect of H on the hardness is visible for the HT1 material, i.e., it has a slightly increased hardness upon H-loading. The effect of H is hardly visible in the microhardness test results of HT2, the hardness values are about the same within the accuracy of the data.

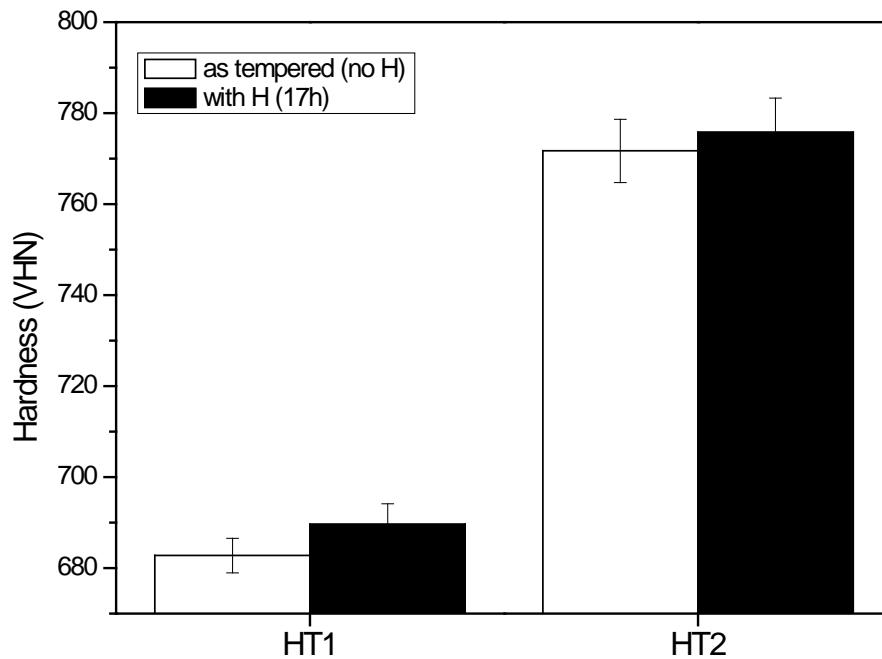


Figure 5.10. Microhardness measurements using a 500 g load on HT1 and HT2 materials. Hardness data are averages over 15 indents.

Combining the high hardness of HT2 with a higher amount of diffusible hydrogen than the HT1 material, the HT2 is expected to suffer more from hydrogen embrittlement than HT1; this is in accordance with literature [57].

The MS results of the SAE 52100 in two heat treatment states are shown in Figure 5.11 for mass-to-charge ratio ( $m/e$ ) = 2. The heating rate was 5 K/min and the heating range was between 300-900 K. In the temperature range of the experiments, only one trap state is clearly observed for both heat treatments. The (desorption) peak maximum occurs around 450 K and is associated with the diffusible H. This is in good agreement with other work done on bearing materials where H-related peak was observed from a little below 400 K [58] to around 450 K [4].

Recent work on electrolytically charged specimens showed that other defects that act as stronger traps form after tensile testing [59]. In that case also desorption peaks with maximums at temperatures above 550 K occur. The amount of H<sub>2</sub> is estimated as 0.4 weight ppm for both materials using the calibration method introduced in Chapter 3. Note that this is an average over the whole sample volume, the penetration depth of H is much smaller than the sample thickness. Comparing these results with the CV results of SAE 52100 material, it is concluded that CV is a more sensitive method to detect H-related differences than the TGA-MS method.

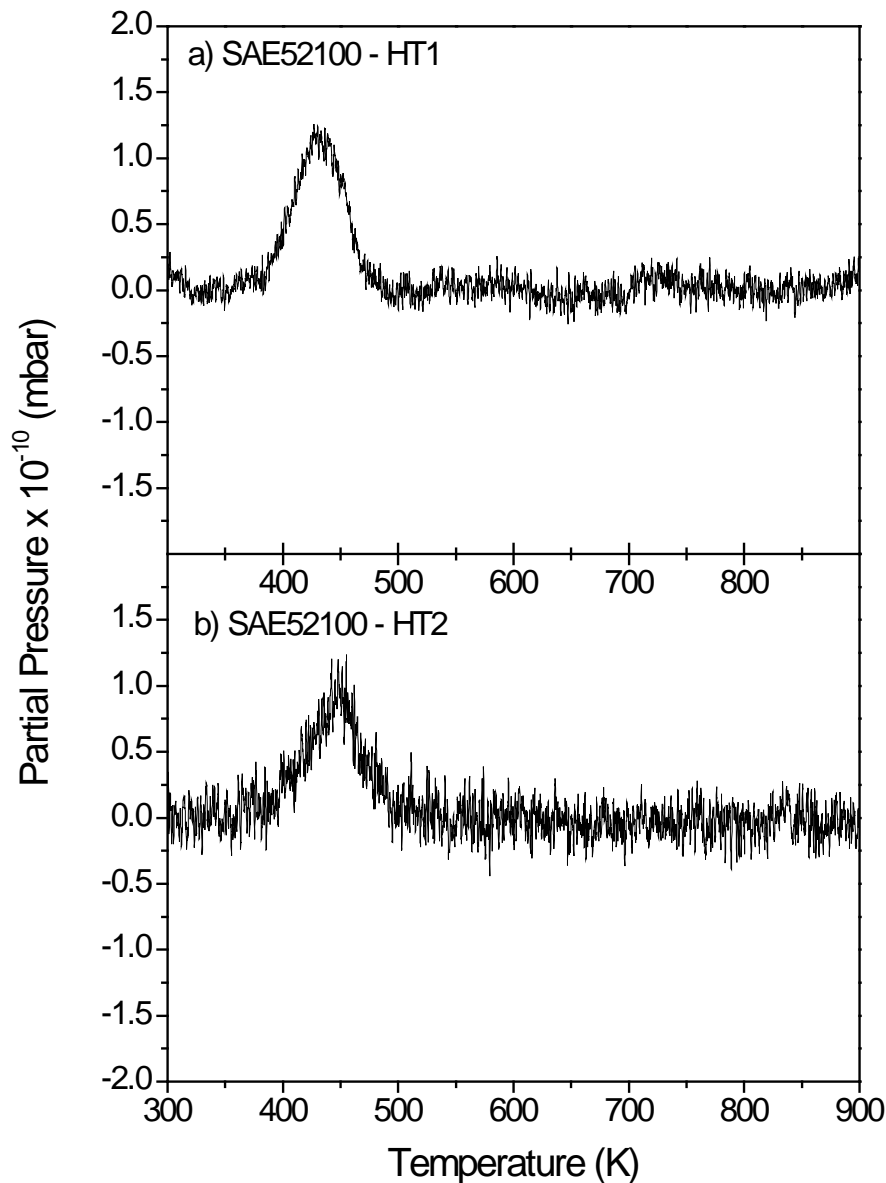


Figure 5.11. MS results of a) SAE 52100 – HT1 b) SAE 52100 – HT2 for heating rate of 5 K/min.

### 5.3.2. Mn-based TWIP steel

The CV scans of the TWIP steel samples with vanadium carbide are given as an example in Figure 5.12. Also in this case Peak I increases as the time of H-loading increases, which relates this peak to hydrogen desorption whereas Peak II is unaffected by the loading time, as in the previous results. When comparing with and without vanadium carbide materials, there is a significant difference between the hydrogen peak areas. The H-desorbed from the samples that have vanadium carbide is considerably lower than for the samples without vanadium carbide (Figure 5.13).

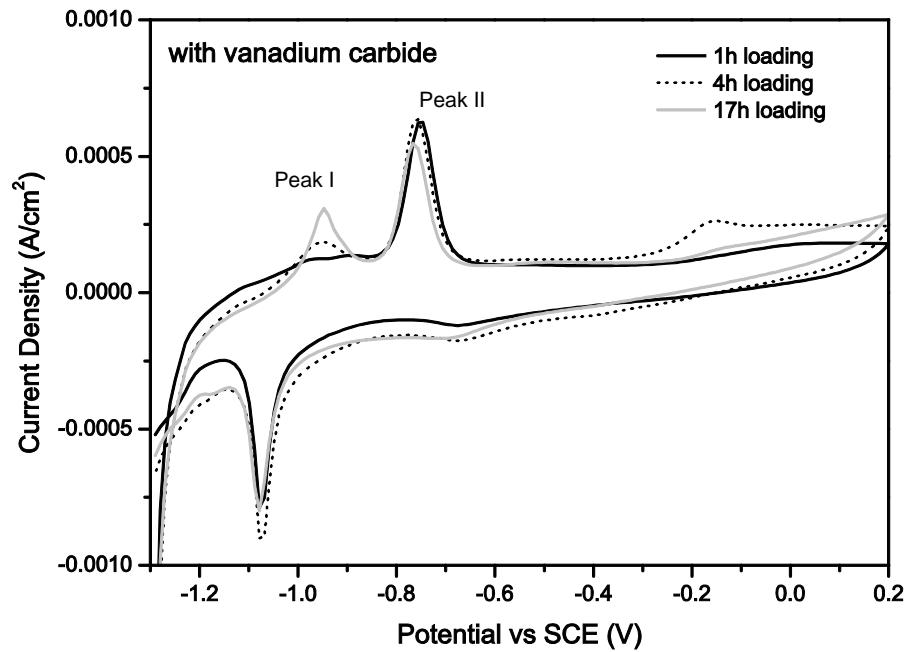


Figure 5.12. CV scan of samples with vanadium carbide (scan 3) after H-loading for 1 h, 4 h and 17 h.

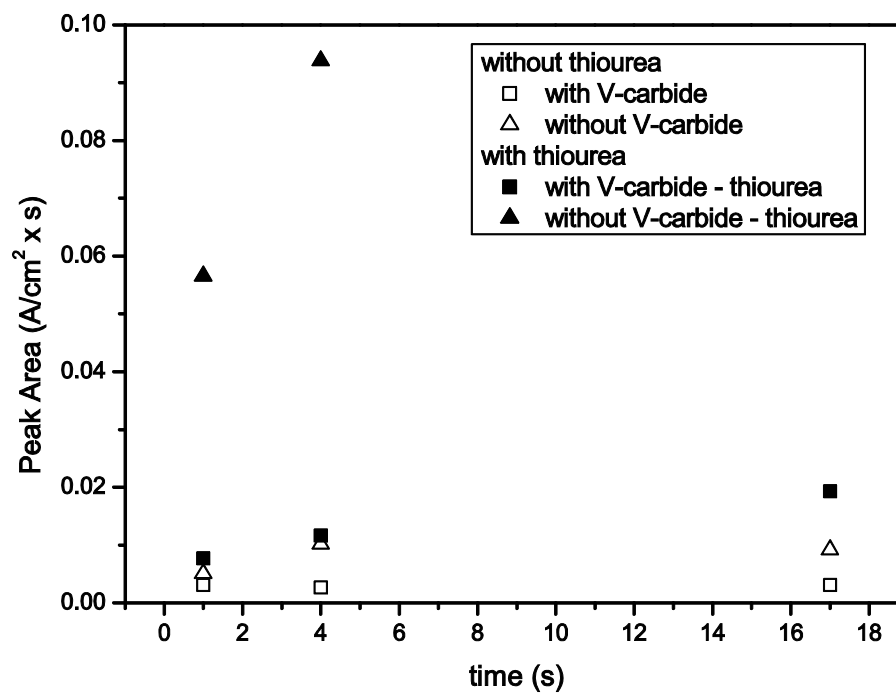


Figure 5.13. Hydrogen desorption peak areas of austenitic Mn-based TWIP steels. Samples that contain vanadium carbides desorb less hydrogen than samples without vanadium carbide.

This result suggests that vanadium carbides act as irreversible traps. This is in accordance with the observations made by Asahi et al. who show that the amount of diffusible H in V-carbide containing low-Mn steels is much lower than in the same steel with V in solid solution [19] and the direct observation of the role of V-carbides as deep traps by Takahashi et al. [21]. Literature

data show that the desorption peaks for the diffusible H for the various steel grades e.g. without V nor Al [11], without V but including Al [15] and with V or V-carbide [19] are all very similar to the ones observed for the ball-bearing steel (SAE 52100), i.e. the maximum of the desorption peak arises in a temperature range around 350-450 K (for different heating rates).

Therefore, in the current work no MS experiments were performed for the TWIP steel. The weak traps associated with the diffusible H are grain boundaries and dislocations [15]. Since the materials investigated here are cold-rolled and recrystallised, the main weak trap sites are expected to be grain boundaries. Asahi et al. also observed that the total amount of H absorbed is higher for the V-carbide containing steel [19]. For the TWIP steels investigated here, however, the H-loading curves for steels with or without V-carbides were not significantly different. This excludes that observed differences are related to differences in the amount of absorbed hydrogen.

When comparing the CV results of the SAE 52100 material with the Mn-based TWIP materials, it is seen that the TWIP materials show higher hydrogen related peak areas (Figure 5.8 vs. Figure 5.13). This could originate from the fact that the TWIP material is fully austenitic and the FCC lattice can uptake higher amounts of hydrogen [46]. The peak potentials of both materials are observed around  $\sim 0.96$  V vs. SCE, and this is also consistent with our previous work on Aermet 100 steel [36].

## 5.4. Conclusions

For the SAE 52100 ball bearing material, the austenite in the HT2 material could be increasing the amount of reversible traps for hydrogen resulting in higher H amounts stored reversibly in the material. The results imply that the diffusible hydrogen content of HT2 is higher than for HT1 that does not contain austenite. Combined with the higher hardness of HT2, this infers that HT2 is expected to suffer more from hydrogen embrittlement than the HT1.

The MS results show that the ball bearing material after two different heat treatments both show single peak desorption profile associated with diffusible hydrogen. This is consistent with the single peaks observed with CV as well as TDS results on similar material. Comparing the CV and TDS methods for SAE 52100 material, it is concluded that CV is a more sensitive method to detect H-related differences than the MS method. This is mainly because the CV was able to detect a higher amount of H desorbing from the HT2 sample, whereas with MS technique similar amounts for HT1 and HT2 materials were observed. This also means that CV is a rather easy and fast measurement method to reveal H-desorption properties that can give clues on H embrittlement susceptibility of materials.

The CV experiments on Mn-based TWIP steel with and without vanadium carbide showed that the amount of H desorbing from samples containing V-carbide was less than for samples without V-carbide. This was attributed to the V-carbides that trap hydrogen irreversibly.

Comparing the various steel grades it can be concluded that the presence of austenite largely contributes to diffusible hydrogen: in general the TWIP material, of a fully austenitic microstructure desorbed higher amounts of hydrogen than the bearing material regardless the presence of carbides, and the bearing material without austenite.

## **Acknowledgements**

We would first and foremost like to thank J.M.C. Mol and H. Terryn for the fruitful discussions regarding the cyclic voltammetry interpretations. The authors gratefully acknowledge J.C. Brouwer for supporting with TGA/MS related experiments and discussions and we would also like to thank R. W. A. Hendrikx and N.M. van der Pers for helping with XRD related sample preparations and discussions. This work is financially supported by the Delft University of Technology and is part of a Materials innovation institute (M2i) research program with project number MC6.06283.

## References

1. Grassel, O., et al., International Journal of Plasticity, 2000. **16**(10-11): p. 1391-1409.
2. Bhadeshia, H.K.D.H., Progress in Materials Science, 2012. **57**(2): p. 268-435.
3. Grunberg, L., D. Scott, and D.T. Jamieson, Philosophical Magazine, 1963. **8**(93): p. 1553-&.
4. Tanimoto, H., H. Tanaka, and J. Sugimura, Tribology Online, 2011. **6**(7): p. 291-296.
5. Deulin, E.A., et al., Surface and Interface Analysis, 2000. **30**(1): p. 635-637.
6. Tanaka, H., et al., Tribology Online, 2013. **8**(1): p. 90-96.
7. Ciruna, J.A. and H.J. Szeleit, Wear, 1973. **24**(1): p. 107-118.
8. Hampshire, J.M. and J.V.H. Nash, G. E. , eds. *Materials evaluation by flat washer testing*. Rolling contact fatigue testing of bearing steels, ed. H.J.J. C. 1982, American Society for Testing of Materials: Pennsylvania, USA. 44-66.
9. R.C., D. and M. E.B., Journal of Basic Engineering, 1960. **82**: p. 302-306.
10. Yajima, E., et al., Transactions of the Japan Institute of Metals, 1974. **15**(3): p. 173-179.
11. Koyama, M., et al., Acta Materialia, 2013. **61**(12): p. 4607-4618.
12. Chin, K.-G., et al., Materials Science and Engineering: A, 2011. **528**(6): p. 2922-2928.
13. Koyama, M., E. Akiyama, and K. Tsuzaki, Corrosion Science, 2012. **54**(0): p. 1-4.
14. Chun, Y.S., et al., Scripta Materialia, 2012. **67**(7-8): p. 681-684.
15. So, K.H., et al., Isij International, 2009. **49**(12): p. 1952-1959.
16. Chun, Y.S., et al., Materials Science and Engineering a-Structural Materials Properties Microstructure and Processing, 2012. **533**: p. 87-95.
17. Frommeyer, G., U. Brux, and P. Neumann, Isij International, 2003. **43**(3): p. 438-446.
18. Ryu, J.H., et al., Proceedings of the Royal Society a-Mathematical Physical and Engineering Sciences, 2013. **469**(2149).
19. Asahi, H., D. Hirakami, and S. Yamasaki, Isij International, 2003. **43**(4): p. 527-533.
20. Spencer, G.L. and D.J. Duquette, *The role of Vanadium Carbide traps in reducing the hydrogen embrittlement susceptibility of high strength alloy steels*, 1998.
21. Takahashi, J., K. Kawakami, and T. Tarui, Scripta Materialia, 2012. **67**(2): p. 213-216.
22. Czerwinski, A. and R. Marassi, Journal of Electroanalytical Chemistry, 1992. **322**(1-2): p. 373-381.
23. Lukaszewski, M. and A. Czerwinski, Electrochimica Acta, 2003. **48**(17): p. 2435-2445.
24. Uluc, A.V., et al., Journal of Electroanalytical Chemistry, 2014. **734**: p. 53-60.
25. Albani, O.A., et al., Electrochimica Acta, 1990. **35**(9): p. 1437-1444.
26. Albani, O.A., et al., Electrochimica Acta, 1986. **31**(11): p. 1403-1411.
27. Diaz, B., et al., Electrochimica Acta, 2009. **54**(22): p. 5190-5198.
28. Geana, D., A.A. Elmiligy, and W.J. Lorenz, Journal of Applied Electrochemistry, 1974. **4**(4): p. 337-345.
29. Guzman, R.S.S., J.R. Vilche, and A.J. Arvia, Electrochimica Acta, 1979. **24**(4): p. 395-403.
30. Guzman, R.S.S., J.R. Vilche, and A.J. Arvia, Journal of Applied Electrochemistry, 1981. **11**(5): p. 551-562.
31. Machado, S.A.S. and L.A. Avaca, Electrochimica Acta, 1994. **39**(10): p. 1385-1391.
32. Veleva, L., et al., Journal of Electroanalytical Chemistry, 2002. **537**(1-2): p. 85-93.
33. Veleva, L., et al., Journal of Electroanalytical Chemistry, 2005. **578**(1): p. 45-53.
34. Visscher, W. and E. Barendrecht, Journal of Applied Electrochemistry, 1980. **10**(2): p. 269-274.
35. Vracar, L. and B.E. Conway, Journal of Electroanalytical Chemistry, 1990. **277**(1-2): p. 253-275.
36. Uluc, A.V., et al., Journal of Electroanalytical Chemistry, 2015. **739**: p. 130-136.
37. Pers, N.M.v.d., et al., Review of Scientific Instruments, 2013. **84**(4): p. 045102.
38. Cullity, B.D. and S.R. Stock, *Elements of X-Ray Diffraction*. 3 ed. 2001: Prentice Hall.
39. Morra, P.V., *Thermo-mechanical loading response of hardened and tempered iron-carbon based alloys*, 2004, Technische Universiteit Delft: Delft. p. 118.
40. Morra, P.V., et al., International Journal of Plasticity, 2009. **25**(12): p. 2331-2348.
41. Morra, P.V., *Chapter 3 - Low Temperature Creep Behaviour of Martensitic Iron-based Alloys Tempered Up to the completion of the first stage of tempering*, in *Thermo-mechanical loading response of hardened and tempered iron-carbon based alloys* 2004, TU Delft: Delft p. p.39.
42. Chateau, J.P., et al., 15th International Conference on the Strength of Materials (Icsma-15), 2010. **240**.

43. Vacuum, P. *Mass Spectrometer*. 2005 1 March 2015]; Available from: <http://www.istcgroup.com/pdf/Mass%20Spectrometer%20Catalog%202005%20-%202007.pdf>.
44. Xu, J., et al., *Acta Metallurgica Et Materialia*, 1993. **41**(5): p. 1455-1459.
45. Yagodzinsky, Y., et al., *Steel Research International*, 2011. **82**(1): p. 20-25.
46. San-Martin, A. and F. Manchester, *Journal of Phase Equilibria*, 1990. **11**(2): p. 173-184.
47. Choi, J.Y., *Metallurgical Transactions*, 1970. **1**(4): p. 911-&.
48. Jiang, D.E. and E.A. Carter, *Physical Review B*, 2004. **70**(6).
49. Oriani, R.A. *The Physical and Metallurgical Aspects of Hydrogen in Metals*. in *4th International Conference on Cold Fusion*. 1993. Lahina, Maui, USA.
50. Marchi, C.S., B.P. Somerday, and S.L. Robinson, *International Journal of Hydrogen Energy*, 2007. **32**(1): p. 100-116.
51. Wei, F.G. and K. Tsuzaki, *Metallurgical and Materials Transactions a-Physical Metallurgy and Materials Science*, 2006. **37A**(2): p. 331-353.
52. Yamasaki, S. and H.K.D.H. Bhadeshia, *Proceedings of the Royal Society a-Mathematical Physical and Engineering Sciences*, 2006. **462**(2072): p. 2315-2330.
53. Bernstein, I.M. and G.M. Pressouyre, eds. *Hydrogen Degradation of Ferrous Alloys*, ed. R.A. Oriani, J.P. Hirth, and M. Smailowski. 1985, Noyes Publications: New Jersey. p. 641.
54. Pound, B.G., *Acta Materialia*, 1998. **46**(16): p. 5733-5743.
55. Stevens, M.F. and I.M. Bernstein, *Metallurgical Transactions a-Physical Metallurgy and Materials Science*, 1985. **16**(10): p. 1879-1886.
56. Takai, K. and R. Watanuki, *Isij International*, 2003. **43**(4): p. 520-526.
57. Gangloff, R.P., *Hydrogen-assisted Cracking*, in *Comprehensive Structural Integrity*, I. Milne, R.O. Ritchie, and B. Karihaloo, Editors. 2003, Pergamon: Oxford. p. 31-101.
58. Hamada, H. and Y. Matsubara, *NTN TECHNICAL REVIEW*, 2006(74).
59. Murakami, Y., et al., *Fatigue & Fracture of Engineering Materials & Structures*, 2013. **36**(9): p. 836-850.



# APPENDICES



# APPENDICES

## APPENDIX A Calculation of [H]/[Pd] from X-ray diffraction peak shifts

Upon loading with H, the XRD peaks of Pd shift to lower  $2\theta$  indicating the phase change from  $\alpha$  to  $\beta$ . After loading, hydrogen starts leaving the sample and after 34 days some of the  $\beta$  phase has turned into  $\alpha$  phase but the hydrogen is not completely out;  $\alpha$  and  $\beta$  phases coexist. The lattice parameter change was calculated upon loading and the result can be found in Figure A. 1. The H concentration in the  $\beta$  phase can be calculated by the well-known linear relationship between the lattice parameter change in Pd and hydrogen concentration which can be seen in the below equation.

$$\frac{3}{a_0} \frac{\Delta a_0}{\Delta x} = 0.19 \pm 0.01 \quad [1]$$

Extrapolating the lattice parameter for  $\theta = 90^\circ$  (Figure A. 2) and using the equation above, the hydrogen concentration is calculated as  $x = [\text{H}]/[\text{Pd}] = 0.6$ . It is known that high pressures are needed for achieving hydrogen concentrations above 0.7 and then the above equation does not hold [1, 2].

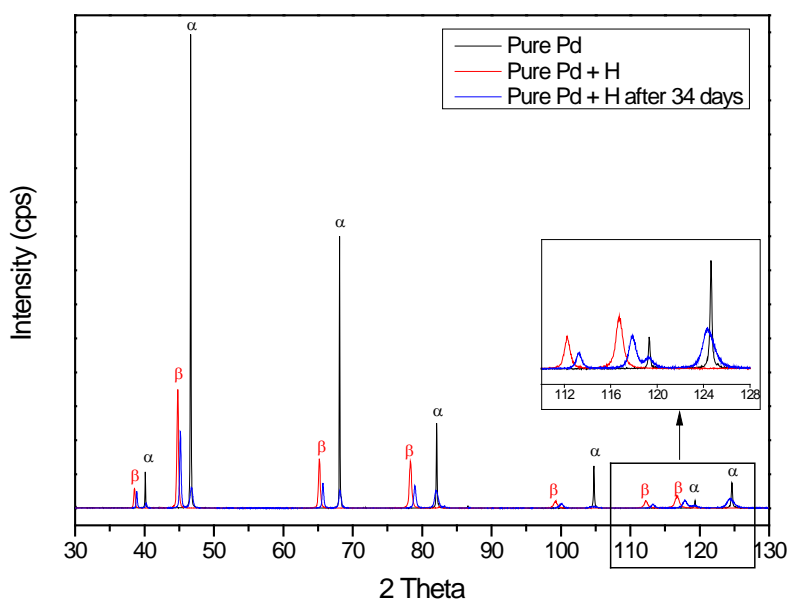


Figure A. 1. XRD scans of pure Pd sample a) reference b) after H-loading c) after H-desorption

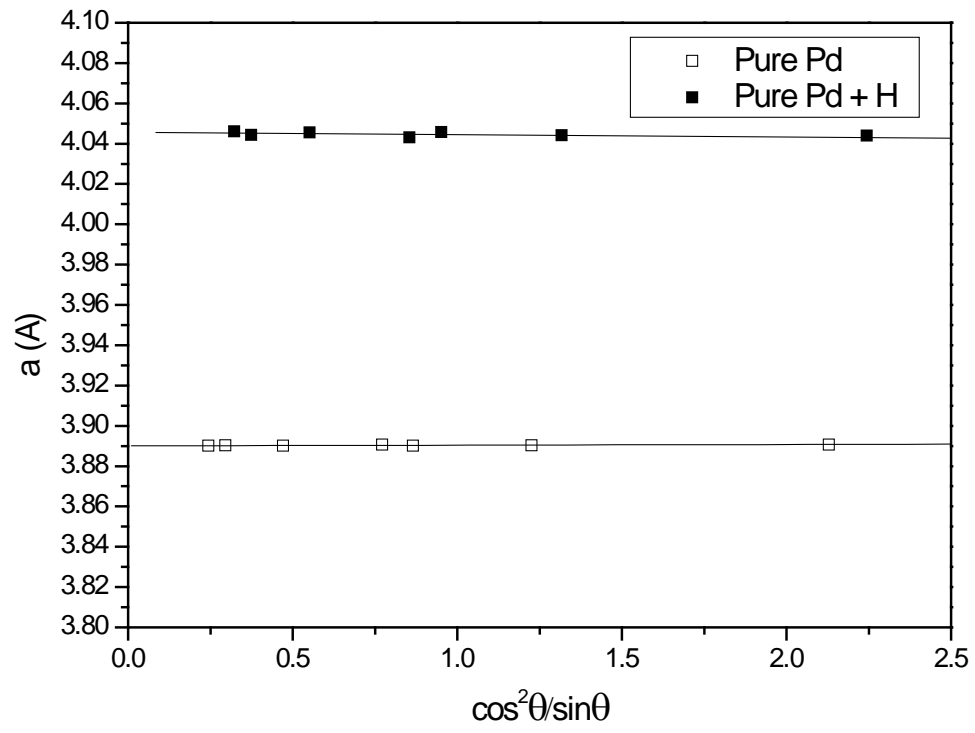


Figure A. 2. Lattice parameter extrapolation to  $\theta = 90^\circ$

## APPENDIX B Effect of isotopes and fragmentation probabilities on a mass spectrum

Because  $m/e$  values for different compounds could overlap (e.g.  $m/e=18$  contains contributions of  $\text{H}_2\text{O}^+$ ,  $^{36}\text{Ar}^{++}$  ions) a correct selection of the mass-to-charge ratios related  $\text{H}_2$  and  $\text{H}_2\text{O}$  to be used for calibration should be made. Therefore, the effect of the isotopes and the cracking patterns of molecules/ions should be considered.

The contributions of the Ar carrier gas to the spectrum will be considered. The three naturally occurring isotopes of the Ar atom are summarized in Table B. 1. Additionally, the fragmentation probabilities need to be considered (see Table B. 2). For the  $^{40}\text{Ar}$  isotope, a peak at  $m/e=40$  (from  $^{40}\text{Ar}^+$ ) and a peak at  $m/e=20$  (from  $^{40}\text{Ar}^{++}$ ) is therefore expected. The fragmentation probabilities in the mass analyser are not absolute as it is for isotopes, different values are reported in literature [4, 5].

Combining the isotope effect with the fragmentation effect, the complete MS contributions are taken into account. The Ar related peaks in the MS are summarized in Table B. 3.

Table B. 1. Natural abundance of Ar isotopes.

Ar isotopes	Natural abundance
$^{36}\text{Ar}$	0.3365%
$^{38}\text{Ar}$	0.632%
$^{40}\text{Ar}$	99.6003%

Table B. 2. Relative ion currents of fragment ions of Ar.

Ar fragment ions	Relative intensity
$\text{Ar}^+$	100%
$\text{Ar}^{++}$	5-22.4%

Similarly the contribution of water to the MS is specified in Table B. 4, taking into account the different oxygen and hydrogen isotopes and fragmentation probabilities of water. From Table B. 3(for Ar) and Table B. 4 (for water), it is concluded that both Ar and water contribute at  $m/e = 20$  and  $m/e=18$ .

Table B. 3. Ar fragment ions and their relative intensity at the corresponding mass-to-charge ratio.

<b>Ar fragment ions</b>	<b>Peak m/e</b>	<b>Relative intensity</b>
$^{36}\text{Ar}^{++}$	18	0.017%
$^{38}\text{Ar}^{++}$	19	0.003%
$^{40}\text{Ar}^{++}$	20	5-22.4%
$^{36}\text{Ar}^+$	36	0.338%
$^{38}\text{Ar}^+$	38	0.063%
$^{40}\text{Ar}^+$	40	100%

The contribution of different sources in a m/e channel of interest can be resolved by calculating the relative contributions for the expected fragments from a major peak from RGA and subtracting that from intensity observed in the m/e channel of interest. Alternatively, if a m/e peak with a rather significant relative intensity did not have contributions from other ions in the chamber, that m/e was can be used in the analysis. This was the case for the water related m/e =17 (Table B. 4).

In conclusion, based on what has been described so far, an analysis of all expected components (based on RGA Figure 3.3) and their fragments (for all isotopes) were made. Based on that, m/e= 17 was chosen for the water related analysis and m/e=2 as the main peak for hydrogen related analysis.

Table B. 4. Water fragment ions and their relative intensities at the corresponding mass-to-charge ratio.

<b>H<sub>2</sub>O fragment ions</b>	<b>Peak m/e</b>	<b>Relative intensity</b>
$^1\text{H}^+$	1	2.4%
$^2\text{H}^+$	2	<4E <sup>-4</sup> %
$^{16}\text{O}^+$	16	1.8%
$^{16}\text{O}^1\text{H}^+$ and $^{17}\text{O}^+$	17	26%
$^{17}\text{O}^1\text{H}^+$ , $^{16}\text{O}^2\text{H}^+$ , $^{18}\text{O}^+$ , $^1\text{H}_2^{16}\text{O}^+$	18	100%
$^{18}\text{O}^1\text{H}^+$ , $^{17}\text{O}^2\text{H}^+$ , $^1\text{H}^1\text{H}^{17}\text{O}^+$ , $^1\text{H}^2\text{H}^{16}\text{O}^+$	19	0.106%
$^{18}\text{O}^2\text{H}^+$ , $^2\text{H}^2\text{H}^{16}\text{O}^+$ , $^1\text{H}^2\text{H}^{17}\text{O}^+$ , $^1\text{H}^1\text{H}^{18}\text{O}^+$	20	0.204%
$^2\text{H}^2\text{H}^{17}\text{O}^+$ , $^2\text{H}^1\text{H}^{18}\text{O}^+$	21	<4E <sup>-5</sup> %
$^2\text{H}^2\text{H}^{18}\text{O}^+$	22	<4.5E <sup>-9</sup> %

## APPENDIX C Calibration for Mass spectroscopy measurements

As hydrogen desorbs out of the Pd-alloys, it is expected to form  $H_2$  gas in the chamber. Alternatively (or simultaneously), as H desorbs out, it reacts to form water. Therefore,  $H_2$  and  $H_2O$  are expected to be the main products upon H desorption within the chamber. In order to quantify the desorbed hydrogen correctly, calibration is needed for both  $H_2$  and water. In order to relate the MS (Chapter 3) results (in partial pressure) to  $H_2$  amounts, calibration was necessary. Calibration was performed regarding both water and hydrogen.

### Calibration of $H_2O$

Copper (II) sulfate pentahydrate ( $CuSO_4 \cdot 5H_2O$ ) was used as a calibration compound for the water signal because it is known to decompose by losing two water molecules at 336 K, followed by two more at 382 K and the final water molecule at 473 K [3].

An example of the MS results is shown in Figure C. 1a, where the partial pressure  $OH^+$  ions at  $m/e = 17$  is shown. The three peaks of the partial pressure-temperature graph in Figure C. 1a match well with the decomposition temperatures expected. The amount of  $H_2O$  in the sample can be predicted by weighing the amount of copper sulphate placed in the chamber. This water content was verified and confirmed by the TGA. Therefore, the amount of  $H_2O$  inside the sample is confidently known. This calibration experiment was repeated three times, and a linear relation of the  $H_2O$  content and the area of the partial pressure-time data was obtained (Figure C. 1b). This relation was then used to calculate the amount of  $H_2O$  from the MS  $H_2O$  signals of all the MS measurements in Chapter 3.

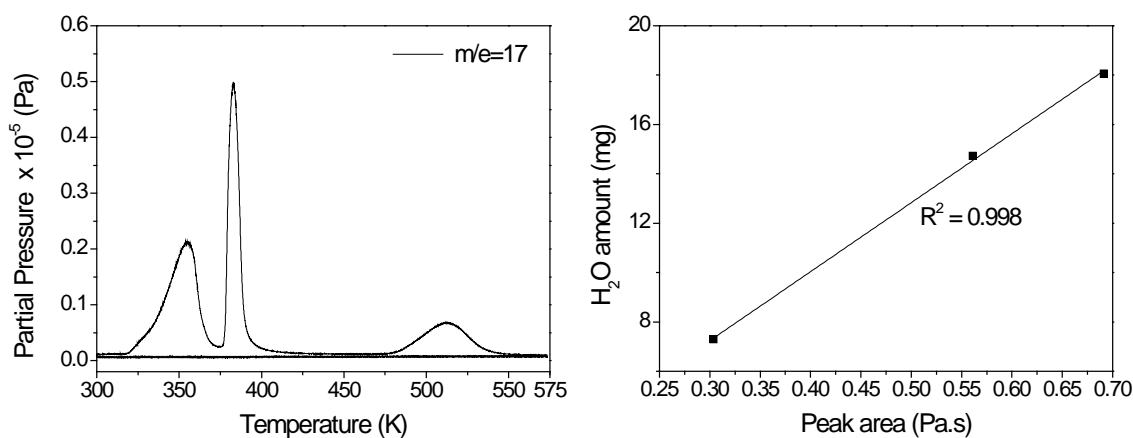


Figure C. 1. Calibration for water a) MS  $m/e=17$  for Copper (II) sulfate pentahydrate ( $CuSO_4 \cdot 5H_2O$ ) during heating b) water amount – MS water peak area relationship.

## Calibration of H<sub>2</sub>

Similar to the calibration of the water, a calibration of the H<sub>2</sub><sup>+</sup> was necessary in order to relate the MS H<sub>2</sub> signal to the H<sub>2</sub> amount in the samples. For this purpose, the experiment first started with flowing 60 ml/min Ar gas in the chamber. The m/e=2 signal pertaining to H<sub>2</sub><sup>+</sup> was measured and used as the background. Then the gas composition was switched to a mixture of Ar and H<sub>2</sub>. An Ar + 50 ppm H<sub>2</sub> flowing with 60 ml/min was fed into the system. The pressure change in the m/e=2 channel ( $\Delta P_{\max}$  in Figure C. 2), taking into account the background, was then used to relate the MS H<sub>2</sub><sup>+</sup> signal to the H<sub>2</sub> amount.

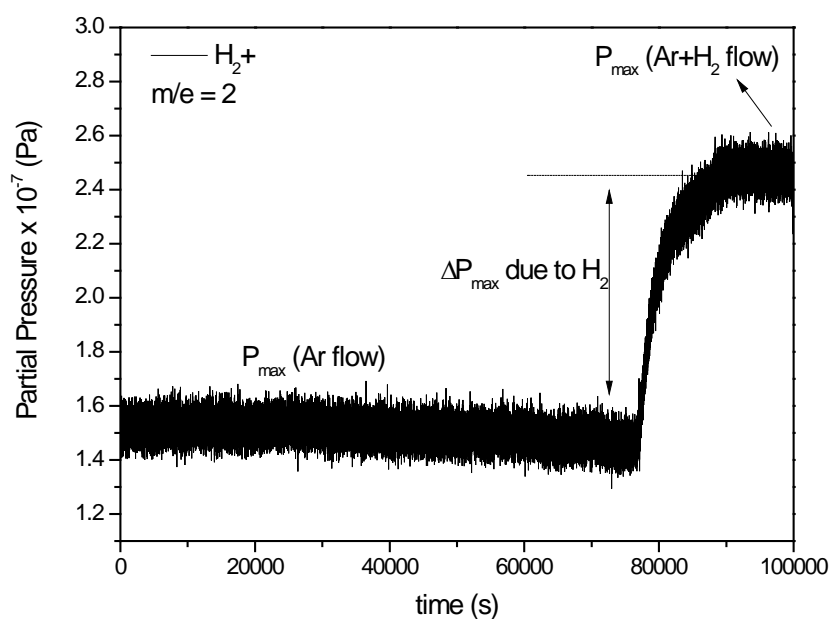


Figure C. 2. Calibration for MS H<sub>2</sub><sup>+</sup> signal.

## References

1. Eastman, J.A., L.J. Thompson, and B.J. Kestel, *Narrowing of the Palladium-Hydrogen Miscibility Gap in Nanocrystalline Palladium*. *Physical Review B*, 1993. **48**(1): p. 84-92.
2. Baranowski, B., S. Majchrzak, and T.B. Flanagan, *The volume increase of fcc metals and alloys due to interstitial hydrogen over a wide range of hydrogen contents*. *Journal of Physics F: Metal Physics*, 1971. **1**(3): p. 258-261.
3. Holleman, A.F. and E. Wiberg, *Holleman-Wiberg's Inorganic Chemistry*. 2001, Berlin: Walter de Gruyter GmbH & Co.
4. S.E. Stein, d. *NIST Mass Spec Data Center, Mass Spectra*. 17 April 2015]; Available from: [webbook.nist.gov](http://webbook.nist.gov).
5. O'Hanlon, J.F., *A User's Guide to Vacuum Technology*. 2004, USA: John Wiley & Sons, Inc.



# SUMMARY



## Summary

Although it has been more than a century since the first known hydrogen embrittlement case was reported, the fundamental question regarding its mechanism is still open to debate. Understanding the hydrogen-metal interactions is of great importance in tailoring microstructures that will have excellent mechanical properties while still resisting hydrogen embrittlement. This is because microstructure and composition affect the thermodynamic and mechanical stability of a material in the presence of hydrogen, as well as the kinetics of processes such as crack propagation, and absorption, desorption and diffusion of hydrogen.

So far, thermal desorption spectroscopy has been widely used in investigating hydrogen traps present in alloys. This method is well-established in identifying binding energies of traps with hydrogen. Mechanical testing, on the other hand, provides a direct assessment of embrittlement but cannot determine trap types or the amount of hydrogen in the material. A direct observation of the material can be provided by *in-situ* TEM, where evidence of the effect of hydrogen on fracture behavior and dislocation pile-ups is given.

In order to complement the above-mentioned methods, in this work a non-destructive, fast and easy method is presented that can be used for screening the hydrogen uptake of alloys. An electrochemical method based on cyclic voltammetry (CV) is used to investigate the hydrogen absorption and desorption of different materials. The method is very useful in quantifying small amounts of hydrogen.

After a brief introduction to hydrogen embrittlement topics in Chapter 1, the CV method is introduced for Pd and Pd-alloys in Chapter 2. The hydrogen sorption and desorption related properties of Pd-alloys (Pd-Au and Pd-Mo-Cu) and pure Pd are investigated in this chapter. Following potentiostatic H-charging for various times, CV is performed in order to monitor the H that desorbs out. It is shown that CV allows quantification of the amounts of hydrogen even in the  $\alpha$ -phase when about 0.05 H atoms per metal atom are present. For short loading times (up to 3000 s), an increase in Au% results in an increase of the amount of H sorbed. During the initial stages of H-absorption where the system is away from a steady state, the H-absorption of different alloys is determined by the kinetics of the reduction process. This is supported by the

potentiostatic H-charging curves, which show that the  $H^+$  reduction at the surface of the Au rich alloys is faster than the Pd rich alloys for loading up to 3000 s. This is the determining factor for the fact that more H desorbs from Au rich samples. In contrast, for long loading times (above 3000 s), the total H amount sorbed by the samples decreases as Au% increases. The total amount of H in the material is determined by thermodynamics. For low H contents, the maximum of the hydrogen oxidation peak potential  $E_p$  reflects the H-metal binding strength or the diffusivity of H and for higher H contents the time needed to remove all the H is determining  $E_p$ .

Following the CV approach on Pd-alloys in Chapter 2, Chapter 3 mainly focuses on thermal H-desorption with a combined method of thermogravimetric analysis and quadrupole mass spectrometry (TGA/MS). H-desorption from Pd, Pd-Au and Pd-Cu-Mo alloys is investigated, and the role of water forming reactions in the route of H-desorption from different Pd-alloys is examined. For pure Pd, two reaction products detected by MS are  $H_2$  and  $H_2O$ . In particular, most of the hydrogen that is absorbed by the Pd sample reacts with the oxygen in the chamber and forms water. This is in contrast to reactions related to Pd-Au and Pd-Cu-Mo samples, where  $H_2$  (and not water) is preferably formed upon desorption. This difference in behavior is attributed to the catalytic activity differences between unalloyed Pd and the Pd-alloys.

Chapters 4 and 5 describe the CV method applied to different steels. Chapter 4 focuses on Aermet 100 steel, an ultra-high strength steel developed for aerospace applications with a good combination of tensile strength and toughness, yet prone to H embrittlement. The material is investigated in two heat treatment states: (i) as-quenched – which is a martensitic structure and (ii) aged – which consists of austenite and martensite. Since CV has not been used frequently for H-detection purposes in steels, the hydrogen related regions of a cyclic voltammogram were closely studied, and the peaks could be unambiguously assigned to chemical reactions. In most cases three prominent peaks appear in the anodic region of the cyclic voltammogram of Aermet 100. Peak I ( $\sim -0.9$  V vs. SCE) is attributed to oxidation of hydrogen, and Peak II ( $\sim -0.75$  V vs. SCE) is related to hydroxidation of Fe. Since Peak III is not commonly seen in cyclic voltammograms of steels or pure Fe, additional CV scans on pure Ni and Co (major alloying elements in Aermet 100) were performed. It is found that the potential  $E_p$  at the maximum of Peak III matches perfectly with the hydrogen oxidation peak observed in Ni sample. Therefore, Peak III in Aermet 100 is ascribed to Ni acting as an easy route for H-absorption. H-sorption is found to be higher in the aged sample than the as-quenched one. Since the major difference between the aged and as-quenched sample is the amount of austenite ( $\sim 19$  vol. % in aged

sample and <2 % in as-quenched sample), it is concluded that austenite enhances the absorption of hydrogen.

In Chapter 5, two other types of steels used for automotive applications are studied. These are a bearing steel (SAE 52100) and an austenitic Mn-based twinning-induced plasticity (TWIP) steel. For the ball-bearing steel, the effect of austenite is investigated. The materials had undergone two different heat treatment states resulting in different microstructures and mechanical properties. Heat treatment 1 (HT1) results in steel consisting of ferrite ( $\alpha$ ), cementite ( $\theta$ ) and transition carbides. Heat treatment 2 (HT2) results in steel consisting of ferrite ( $\alpha$ ), cementite ( $\theta$ ), retained austenite ( $\gamma_R$ ) and transition carbides. The CV results imply that the diffusible hydrogen content of HT2 is higher than for HT1. This is mainly attributed to the austenite in the HT2 material which stores H reversibly. Combined with the higher hardness of HT2, this implies that HT2 is expected to suffer more from hydrogen embrittlement than HT1. The MS results show that the ball bearing material with two different heat treatments both show a single peak desorption profile associated with diffusible hydrogen. Comparing the CV and TDS methods for SAE 52100 steel, we conclude that CV is a more sensitive method to detect H-related differences between materials than MS. This causes CV to be able to detect a higher amount of H desorbing from the HT2 sample than from the HT1 sample, whereas similar hydrogen amounts for HT1 and HT2 were observed with MS.

Fully austenitic Mn-based TWIP steel is investigated in two compositions, where the main difference is the vanadium content. One composition has a higher amount of vanadium and is heat treated to develop V-carbides. The other composition, with a negligible amount of vanadium, has gone through the same heat treatment as the first one. The CV scans show that the amount of H desorbing from samples containing V-carbide is less than for samples without V-carbide. This is attributed to irreversible trapping of hydrogen by V-carbides.



# SAMENVATTING



# Samenvatting

Hoewel het meer dan een eeuw geleden is dat het eerste geval van waterstofverbrossing werd gemeld, staat de fundamentele verklaring van het mechanisme ervan nog altijd ter discussie. Om doelgericht metalen met microstructuren te fabriceren die zowel uitstekende mechanische eigenschappen hebben als ook weerstand hebben tegen waterstofverbrossing, is het van groot belang de wisselwerking tussen waterstof en metalen te begrijpen. Dit komt omdat microstructuur en samenstelling de thermodynamische en mechanische stabiliteit van een materiaal in de aanwezigheid van waterstof beïnvloeden, en ook de kinetiek van processen zoals scheurgroei, en absorptie, desorptie en diffusie van waterstof.

Tot nu toe is thermische desorptiespectroscopie (TDS) veel gebruikt om vangstplaatsen (*traps*) voor waterstof in metaallegeringen te onderzoeken. Deze methode wordt toegepast om bindingsenergieën van waterstof aan deze defecten te bepalen. Aan de andere kant verschaft mechanisch testen een directe maat voor de brosheid, maar daarmee kan noch het soort *trap* noch de hoeveelheid waterstof in het materiaal vastgesteld worden. Directe waarneming van het materiaal is mogelijk met *in-situ* transmissie elektronenmicroscop, waarmee het effect van waterstof op breukgedrag en dislocatieaccumulatie wordt aangetoond.

Als aanvulling op de bovengenoemde methodes wordt in dit werk een niet-destructieve, snelle en eenvoudige methode gepresenteerd die kan worden gebruikt voor het zichtbaar maken van waterstofopname in legeringen. Het gaat om een electrochemische methode gebaseerd op cyclische voltammetrie (CV). In dit proefschrift is deze gebruikt om waterstofabsorptie en -desorptie in verschillende materialen te onderzoeken. De methode is zeer bruikbaar voor het kwantificeren van kleine hoeveelheden waterstof.

Na een korte introductie tot waterstofverbrossing in Hoofdstuk 1, wordt in Hoofdstuk 2 de CV methode voor Pd en Pd-legeringen geïntroduceerd. In dit hoofdstuk worden eigenschappen van Pd-legeringen (Pd-Au en Pd-Mo-Cu) en puur Pd die gerelateerd zijn aan waterstofabsorptie en -desorptie onderzocht. Na herhaald potentiostatisch H-beladen wordt met CV het desorberende H geobserveerd. Het laat zien dat CV-kwantificering van de hoeveelheid waterstof mogelijk is, zelfs in de  $\alpha$ -fase waarin slechts 0.05 H-atomen per metaalatoom aanwezig zijn. Voor korte laadtijden (tot 3000 s) neemt de hoeveelheid gesorbeerde waterstof toe met het percentage Au. In de beginfase van H-absorptie, waar het systeem niet stabiel is, wordt de H-absorptie van

verschillende legeringen bepaald door de kinetiek van het reductieproces. Dit wordt ondersteund door de potentiostatische H-beladingsmetingen die laten zien dat tot 3000 s de  $H^+$ -reductie aan het oppervlak van Au-rijke legeringen sneller is dan voor Pd-rijke legeringen. Dit is de belangrijkste reden voor de gemeten grotere H-desorptie uit Au-rijke monsters. Dit in tegenstelling tot langere laadtijden (boven 3000s), waarbij de hoeveelheid gesorbeerde H afneemt bij toename van het Au%. De totale hoeveelheid H in het materiaal wordt dan bepaald door de thermodynamica. Voor lage H-gehalten representeert het maximum van de waterstofoxidatiepiekpotentiaal  $E_p$  de H-metaal bindingskracht of de diffusiviteit van H; voor hogere H-gehalten wordt  $E_p$  bepaald door de tijd die nodig is om alle H te desorberen.

Volgend op de CV-benadering van Pd-legeringen in Hoofdstuk 2, gaat Hoofdstuk 3 voornamelijk in op thermische H-desorptie door middel van een combinatie van thermogravimetrische analyse en quadrupool-massaspectrometrie (TGA/MS). Zowel de H-desorptie uit Pd, Pd-Au en Pd-Cu-Mo legeringen als de rol van watervormende reacties bij H-desorptie uit verschillende Pd-legeringen worden onderzocht. Voor puur Pd worden met MS twee reactieproducten waargenomen, te weten  $H_2$  en  $H_2O$ . Meer in het bijzonder reageert de meeste waterstof die is geabsorbeerd door de Pd-preparaten met de zuurstof in de meetopstelling en vormt water. Dit in tegenstelling tot reacties bij Pd-Au en Pd-Cu-Mo, waarin vooral  $H_2$  (en niet water) wordt gevormd bij desorptie. Dit verschil in gedrag wordt toegeschreven aan de verschillen in katalytische activiteit tussen ongelegeerd Pd en de Pd-legeringen.

Hoofdstukken 4 en 5 beschrijven de toepassing van de CV-methode op verschillende types staal. Hoofdstuk 4 behandelt Aermet 100 staal, een ultra-hogesterkte-staal ontwikkeld voor luchtvaarttoepassingen, met een goede combinatie van treksterkte en taaiheid, maar ook vatbaar voor waterstofverbrossing. Het wordt onderzocht na twee warmtebehandelingen: (i) snel afgekoeld (*quenched*) hetgeen een martensitische structuur oplevert, en (ii) verouderd (*aged*) – bestaande uit austeniet en martensiet. Aangezien CV tot dusverre niet vaak gebruikt is voor H-onderzoek in staal, zijn de waterstofgerelateerde gebieden van een cyclisch voltammogram in dit werk nauwkeurig bestudeerd en konden de pieken ondubbelzinnig worden toegeschreven aan chemische reacties. In de meeste gevallen verschijnen drie prominente pieken in het anodische gebied van het cyclisch voltammogram van Aermet 100. Piek I ( $\sim -0.9$  V vs. SCE) wordt toegeschreven aan oxidatie van waterstof. Piek II ( $\sim -0.75$  V vs. SCE) is gerelateerd aan de hydroxidatie van Fe. Aangezien piek III in het algemeen niet gezien wordt in cyclisch voltammogrammen van staal of puur Fe, werden aanvullende CV-scans gemeten voor puur Ni en Co (de belangrijkste legeringselementen in Aermet 100). Het resultaat is dat de potentiaal  $E_p$  op

het maximum van piek III perfect overeenkomt met de waterstofoxidatiepiek gemeten voor het Ni monster. Daarom wordt piek III in Aermet 100 toegeschreven aan Ni dat een eenvoudige route voor H-absorptie verschaft. Vastgesteld is dat H-sorptie hoger is in het *aged* preparaat dan in het *as-quenched* preparaat. Aangezien het grootste verschil tussen het verouderde en het snel afgekoelde preparaat de hoeveelheid austeniet is (ongeveer 19 vol. % in het *aged* preparaat versus minder dan 2% in het *as-quenched* preparaat), kan worden geconcludeerd dat austeniet de absorptie van waterstof bevordert.

In Hoofdstuk 5 worden twee andere soorten staal bestudeerd, die allebei gebruikt worden in de autoindustrie. Dit zijn een kogellagerstaal (SAE 52100) en een austenitisch TWIP-staal met Mn (TWIP = *Twinning Induced Plasticity*). Voor het kogellagerstaal is het effect van austeniet onderzocht. De materialen hadden twee verschillende warmtebehandelingen ondergaan die resulteerden in verschillende microstructuren en mechanische eigenschappen. Warmtebehandeling 1 (HT1) leidt tot staal dat bestaat uit ferriet ( $\alpha$ ), cementiet ( $\theta$ ) en overgangscarbiden. Na warmtebehandeling 2 (HT2) bevat het staal daarnaast nog restausteniet ( $\gamma_R$ ). De CV-resultaten laten zien dat er meer mobiel waterstof in HT2 aanwezig is dan in HT1. Dit wordt voornamelijk toegeschreven aan het austeniet in het HT2-materiaal, dat H reversibel opslaat. In combinatie met de grotere hardheid van HT2 leidt dit tot de verwachting dat HT2 meer waterstofverbrossing zal vertonen dan HT1. De MS-resultaten laten zien dat het kogellagermateriaal bij de twee verschillende warmtebehandelingen een enkele desorptiepiek bevat die wijst op mobiel waterstof. Na vergelijking van de CV- en TDS-methodes voor SAE 52100 staal, concluderen we dat CV een gevoeliger methode is om H-gerelateerde verschillen tussen materialen te onderzoeken dan MS. Dit maakt dat CV de verschillen in desorptiehoeveelheid tussen HT1 en HT2 kan aantonen, terwijl MS die verschillen niet kon waarnemen.

Volledig austenitisch mangaanhoudend TWIP-staal is onderzocht in twee samenstellingen, waarbij het grootste verschil zit in de hoeveelheid vanadium. De ene samenstelling heeft een hogere hoeveelheid vanadium en heeft een warmtebehandeling ondergaan om V-carbides te ontwikkelen. De andere samenstelling, met een verwaarloosbare hoeveelheid vanadium, heeft dezelfde warmtebehandeling ondergaan. De CV-scans laten zien dat er minder H desorbeert van de monsters met V-carbide dan van monsters zonder. Dit wordt toegeschreven aan het irreversibel afvangen van waterstof door de V-carbiden.



ACKNOWLEDGE-  
MENTS



# Acknowledgements

There we are. For a long time, I have been looking forward to the moment of writing my acknowledgements, as this would mean that the long pursuit of a Ph.D. degree is approaching an end. Here I am at this moment and I realize that it is a disturbing thought to miss a single person while trying to thank everyone who have helped me in this process. Nevertheless, I will do my best.

First and foremost, I would like to thank my promoter Barend Thijssen and my supervisor Amarante Böttger for all their support and input both regarding the scientific interpretations and also for their understanding, patience and encouragement during the long period of finalizing my Ph.D work while working in a full-time job.

Next, I would like to express my great appreciation to Herman Terry and Arjan Mol for their invaluable support, feedback and enthusiasm regarding my work. Thank you for always making me feel like a part of your group by always being available for my questions and inviting me to your amazingly entertaining groups uitjes. I will always be grateful.

The experimental work in this thesis would not have been possible without the help of Bo Han, Hans Brouwer, Bart Norbart, Ruud Hendriks, Niek van der Pers, Lambert Schipperheijn, Frans Tichelaar and Eirini Zcharaki. Thank you for all your efforts that you have put into this work. I am happy to be able to show you with this thesis that your efforts were not for nothing.

Special thanks go to Monica Reulink. I do not know if I was able to show you how much I appreciated your help and support during the last year that I was at TU Delft. Your encouraging words and attitude have helped a lot in the most stressful days. A warm thank you.

Staf de Keijser, I think I was the luckiest one there on the 4<sup>th</sup> floor to have shared the same office with you. I have enjoyed and still fondly remember our conversations and the lovely days that we spent at your house with your wife. Thanks for everything. One of our conversations have inspired me about a proposition that I have written. I hope you like it.

Cindy Cencen, thank you very much for translating the summary of this thesis to Dutch.

I would like to express my thanks to my former and current group leaders at Bosch Transmission Technology, namely Andreas Birnesser and Patrick van Eerd. It has always been comforting to

feel your support and encouragement to finalize my Ph.D. Thank you for your flexibility and understanding during these two years. I would also like to name some colleagues who have supported me without even knowing: Corné Maas, Ronald Cornelissen, Robert Antonise, Kazem Yazdchi, Louis Huysmans. Jan-Willem Lenderink, Wim Janssen and Lili Crebolder, thank you for your support.

It goes without saying that I have had great colleagues/friends within this period with whom I have had scientific discussions over lunches as well as having absolutely a great time together. I would like to be specific and list some important names for me: Darko, Ivan, Raymond, Sebastian, Fidel, Vahid, Onnaz, Yaiza, Emre, Andy, Francois, Santi, Peyman, Georgina, Neha, Maria... I am absolutely certain I am missing some names here, if so, I am terribly sorry but I am sure you are a great person and thank you for your contribution to my journey!

And then, the real deal: Deniz, Gozde, Ali and Nil... It is difficult to find the right words for you guys. Just THANK YOU, for always being there. I am hoping that we will catch up soon. Argun, thank you also for your support and friendship and also letting me crush your couch when I needed to stay in Delft. Noyan, I'm lucky to have you as a younger brother now, thanks for your support.

Seren, Natali and Melisa. Thank you for your friendship which never lost its warmth despite of long distances between us. Seren, thanks for lighting candles at every single church you have been to around the world, now you can stop doing that!

Mamacim ve babacim. İyi ki varsınız. Sizi çok seviyorum ve bu dönemde bana göstermiş olduğunuz anlayış, sevgi ve destek için çok ama çok teşekkür ederim. Alış, iyi ki varsın, torunun doktor oldu anlat herkese.

My dear brother, Artur. I am the luckiest person on earth to have such a brother to always look up to. You know that you are the reason that I am where I am, and you have had a great influence on the person that I turned out to be (for better or worse). I love you, always.

And finally. First a football mate and now my partner in life: Sinan. You have been by my side throughout this journey, and I am especially happy because maybe now I can get closer to being the partner that you truly deserve. Just maybe.

Vanya

Breda, July 2015

ABOUT THE  
AUTHOR



## **About the Author**

Vanya Uluc was born on August 29<sup>th</sup>, 1983, in Istanbul, Turkey. She studied at Ferikoy Armenian Primary School and received her high school education at Pangalti Armenian High School. In 2001, she started to pursue her Bachelor's degree at Metallurgy and Materials Science Engineering department of Istanbul Technical University. Following her graduation in 2006, she immediately started her master studies at Sabanci University in Istanbul within Materials Science and Engineering department with full scholarship. As a next step in her career, in November 2008, she moved to The Netherlands to pursue a Ph.D. degree at Delft University of Technology. The results of this pursuit are presented in this thesis. From July 2013 to date, she is working at Bosch Transmission Technology in Tilburg as a process development engineer mainly focused on heat treatment processes.

